

Modeling Pc4 Pulsations in Two and a Half Dimensions and Comparisons to Van Allen Probe Observations

DRAFT VERSION CREATED ON APRIL 26, 2016

1

© Charles A. McEachern 2016

2



3

The text of this work is licensed under a Creative Commons

Attribution-ShareAlike 4.0 International license.

4

⁵ Acknowledgements

⁶ TODO: ...

Abstract

Field line resonances — that is, Alfvén waves bouncing between the northern and southern foot points of a geomagnetic field line — serve to energize magnetospheric particles through drift-resonant interactions, carry energy from high to low altitude, induce currents in the magnetosphere, and accelerate particles into the atmosphere. Wave structure and polarization significantly impact the execution these roles. The present work showcases a new two and a half dimensional code, Tuna, ideally suited to model FLRs, with the ability to consider large-but-finite azimuthal modenumbers, coupling between the poloidal, toroidal, and compressional modes, and arbitrary harmonic structure. Using Tuna, the interplay between Joule dissipation and poloidal-to-toroidal rotation is considered for both dayside and nightside conditions. An attempt is also made to demystify giant pulsations, a class of FLR known for its distinctive ground signatures. Numerical results are supplemented by a survey of ~ 500 FLRs using data from the Van Allen Probes, the first such survey to characterize each event by both polarization and harmonic. The combination of numerical and observational results suggests an explanation for the disparate distributions observed in poloidal and toroidal FLR events.

Contents

²⁴	Acknowledgements	i
²⁶	Abstract	ii
²⁷	List of Tables	vi
²⁸	List of Figures	vii
²⁹	1 Introduction	1
³⁰	1.1 Structure of the Present Work	2
³¹	2 The Near-Earth Environment	4
³²	2.1 The Outer Magnetosphere	5
³³	2.2 The Inner Magnetosphere	7
³⁴	2.3 The Ionosphere	8
³⁵	2.4 Geomagnetic Storms and Substorms	9
³⁶	3 Field Line Resonance	12
³⁷	3.1 Harmonic Structure	16
³⁸	3.2 Azimuthal Modenumber	18
³⁹	3.3 Poloidal and Toroidal Polarizations	20
⁴⁰	3.4 Giant Pulsations	22
⁴¹	3.5 Motivations for the Present Work	23
⁴²	4 Waves in Cold Resistive Plasma	25

43	4.1 Guided Propagation	27
44	4.2 Compressional Propagation	28
45	4.3 High Altitude Limit	30
46	4.4 Implications to the Present Work	31
47	5 “Tuna Half” Dimensional Model	33
48	5.1 Coordinate System	34
49	5.2 Physical Parameter Profiles	38
50	5.3 Driving	41
51	5.4 Maxwell’s Equations	44
52	5.5 Boundary Conditions	48
53	6 Electron Inertial Effects	53
54	6.1 The Boris Factor	54
55	6.2 Parallel Currents and Electric Fields	56
56	6.3 Inertial Length Scales	61
57	6.4 Discussion	63
58	7 Numerical Results	65
59	7.1 Modenumber and Compression	65
60	7.2 Resonance and Rotation on the Dayside	71
61	7.3 Resonance and Rotation on the Nightside	78
62	7.4 Ground Signatures and Giant Pulsations	83
63	7.5 Discussion	87
64	8 Van Allen Probe Observations	89
65	8.1 Sampling Bias and Event Selection	90
66	8.2 Events by Mode	95
67	8.3 Events by Amplitude	99
68	8.4 Events by Frequency	102
69	8.5 Events by Phase	105
70	8.6 Discussion	110
71	9 Conclusion	112

72	9.1	Code Development	112
73	9.2	Numerical Work	113
74	9.3	Van Allen Probe Pc4 Survey	114
75	References		115

⁷⁶ **List of Tables**

⁷⁷	3.1 IAGA Magnetic Pulsation Frequency Bands	14
⁷⁸	5.1 Typical Parameters for the Tuna Density Profile	39
⁷⁹	5.2 Integrated Atmospheric Conductivity	49

List of Figures

81	2.1	Reconnection in the Outer Magnetosphere	5
82	2.2	Structures in the Inner Magnetosphere	7
83	3.1	Alfvén Bounce Frequencies	15
84	3.2	First and Second Harmonic Resonances	17
85	3.3	Azimuthal Modenumbers Viewed from the Pole	19
86	3.4	Poloidal Mode Structure	21
87	3.5	Toroidal Mode Structure	22
88	4.1	Compressional Alfvén Wave Cutoff Frequencies	32
89	5.1	Nonorthogonal Dipole Grid	38
90	5.2	Alfvén Speed Profiles	40
91	5.3	Ionospheric Conductivity Profiles	41
92	5.4	Decreasing Penetration with Increasing Modenumber	43
93	5.5	Sym-H for June 2013 Storm	44
94	6.1	Plasma Frequency Profile	55
95	6.2	Electric Field Snapshots	57
96	6.3	Current and Poynting Flux at 1000 km	58
97	6.4	Current and Poynting Flux at 100 km	60
98	6.5	Power Density at the Ionosphere	61
99	6.6	Parallel Electric Fields by Perpendicular Grid Resolution	62
100	7.1	Magnetic Field Snapshots from a Small- m Run	68
101	7.2	Magnetic Field Snapshots from a Large- m Run	69
102	7.3	Compressional Coupling to the Poloidal Mode	70
103	7.4	Dayside Poloidal and Toroidal Energy	75

104	7.5 Dayside Poloidal Energy Distribution	76
105	7.6 Dayside Toroidal Energy Distribution	77
106	7.7 Nightside Poloidal and Toroidal Energy	80
107	7.8 Nightside Poloidal Energy Distribution	81
108	7.9 Nightside Toroidal Energy Distribution	82
109	7.10 Dayside Ground Magnetic Fields	85
110	7.11 Nightside Ground Magnetic Fields	86
111	8.1 Distribution of Usable Van Allen Probe Data	91
112	8.2 Waveforms and Spectra for a Toroidal Pc4 Event	94
113	8.3 Rate of Pc4 Events	96
114	8.4 Rate of Pc4 Events by Mode	97
115	8.5 Amplitude Distribution of Pc4 Events by Mode	100
116	8.6 Rate of Pc4 Events by Mode and Amplitude	101
117	8.7 Rate of Pc4 Events by Mode and Frequency	103
118	8.8 Frequency Distribution of Pc4 Events by Mode	104
119	8.9 Waveforms and Spectra for a Double Pc4 Event	107
120	8.10 Phase Distribution of Pc4 Events by Mode	108
121	8.11 Rate of Pc4 Events by Mode and Phase	109

¹²² Chapter 1

¹²³ Introduction

¹²⁴ 1859 was a pivotal year in human history. The United States moved steadily toward
¹²⁵ the American Civil War, which would abolish slavery and consolidate the power of
¹²⁶ the federal government. A slew of conflicts in Southern Europe set the stage for the
¹²⁷ unification of Italy. The Taiping Civil War — one of the bloodiest conflicts of all time
¹²⁸ — is considered by many to mark the beginning of modern Chinese history. Origin of
¹²⁹ Species was published. The first transatlantic telegraph cable was laid.

¹³⁰ Meanwhile, ambivalent to humanity, the Sun belched an intense burst of charged par-
¹³¹ ticles and magnetic energy directly toward Earth. The resulting geomagnetic storm¹
¹³² caused telegraph systems to fail across the Western hemisphere, electrocuting operators
¹³³ and starting fires[35, 94]. Displays of the northern lights were visible as far south as
¹³⁴ Cuba.

¹³⁵ The Solar Storm of 1859 was perhaps the most powerful in recorded history, but by no
¹³⁶ means was it a one-time event. The Sun discharges hundreds of coronal mass ejections
¹³⁷ (CMEs) per year, of all sizes, in all directions. In fact, a comparably large CME narrowly
¹³⁸ missed Earth in 2012[71]. Had it not, it's estimated it would have caused widespread,
¹³⁹ long-term electrical outages, with a damage toll on the order of 10^{12} dollars[67].

¹The Solar Storm of 1859 is also called the Carrington Event, after English astronomer Richard Carrington. He drew a connection between the storm's geomagnetic activity and the sunspots he had observed the day before.

140 The Sun’s extreme — and temperamental — effect on Earth’s magnetic environment
141 makes a compelling case for the ongoing study of space weather. Such research has
142 evolved over the past century from sunspot counts and compass readings to multi-
143 satellite missions and supercomputer simulations. Modern methods have dramatically
144 increased humanity’s understanding of the relationship between the Sun and the Earth;
145 however, significant uncertainty continues to surround geomagnetic storms, substorms,
146 and the various energy transport mechanisms that make them up.

147 The present work focuses in particular on the phenomenon of field line resonance: Alfvén
148 waves bouncing between the northern and southern hemispheres. Such waves play an
149 important part in the energization of magnetospheric particles, the transport of energy
150 from high to low altitude, the precipitation of particles into the atmosphere, and the
151 driving of currents at the top of the atmosphere. It is these currents which give rise to
152 potentially-catastrophic magnetic disturbances at Earth’s surface.

153 The study of resonance in the near-Earth environment is furthermore valuable as a proxy
154 for other (less-accessible) plasma environments. Similar waves occur in astrophysical
155 plasmas, observation of which is limited by distance. Field line resonance is also analo-
156 gous to the so-called “fishbone instability” in fusion reactors. As a plasma laboratory,
157 the magnetosphere is unique in that it is both close enough to measure directly, and
158 also large enough that measurements can be performed without disrupting its behavior.

159 1.1 Structure of the Present Work

160 The present work is laid out as follows.

161 Chapter 2 surveys the near-Earth environment. Prominent features of the magneto-
162 sphere are defined. The behavior of the magnetosphere during geomagnetic storms and
163 substorms is summarized.

164 Chapter 3 introduces the field line resonance phenomenon, in terms of both the under-
165 lying physics and notable work on the topic. Jargon is introduced to clarify important
166 elements of wave structure. Several open questions about field line resonances (FLRs)
167 are offered as motivations for the present work.

168 Chapter 4 lays the groundwork for a numerical model by exploring the fundamental
169 equations of waves in a cold, resistive plasma — such as Earth’s magnetosphere. Char-
170 acteric scales are gleaned from the resulting dispersion relations.

171 Chapter 5 presents Tuna, a new two and a half dimensional simulation designed specif-
172 ically for the realistic modeling of FLRs. Tuna’s non-orthogonal geometry, height-
173 resolved ionosphere, novel driving mechanism, and coupling to the atmosphere are jus-
174 tified and explained.

175 Chapter 6 considers the addition of electron inertial effects to Tuna, which are neglected
176 in the core model presented in Chapter 5. These effects allow the computation of parallel
177 currents and electric fields, which have not previously been included in global Alfvén
178 models. The effects are shown to be instability-prone and computationally expensive,
179 but some results are gleaned nonetheless.

180 Chapter 7 showcases the core numerical results of the present work, unifying several of
181 the questions posed in Chapter 3. The interplay between compressional propagation,
182 poloidal-to-toroidal rotation, and Joule dissipation is considered from several angles.

183 Chapter 8 puts the numerical results in context through the analysis of data from the
184 Van Allen Probes mission. FLR occurrence rates are considered in terms of location,
185 harmonic, and polarization, parameters which have been only partially addressed in
186 past FLR surveys.

187 Chapter 9 briefly summarizes the results shown in the above chapters — code devel-
188 opment, analysis of numerical results, and satellite observation — and suggests further
189 directions.

¹⁹⁰ **Chapter 2**

¹⁹¹ **The Near-Earth Environment**

¹⁹² From Earth’s surface to a height of a hundred kilometers or so, the atmosphere is a
¹⁹³ well-behaved fluid: a collisional ensemble of neutral atoms. Higher up, its behavior
¹⁹⁴ changes dramatically. As altitude increases, solar ultraviolet radiation becomes more
¹⁹⁵ intense, which ionizes atmospheric atoms and molecules. Density also decreases, slow-
¹⁹⁶ ing collisional recombination. Whereas the neutral atmosphere is held against Earth’s
¹⁹⁷ surface by gravity, the motion of charged particles is dominated by Earth’s geomagnetic
¹⁹⁸ field, as well as the electromagnetic disturbances created as that field is hammered by
¹⁹⁹ the solar wind.

²⁰⁰ Before discussing specific interactions, it’s appropriate to introduce the so-called “frozen-
²⁰¹ in condition.” In a collisionless plasma, magnetic field lines are equipotential contours.
²⁰² Charged particles move freely along the contours, but cannot move across them. Com-
²⁰³ pression of the magnetic field is synonymous with compression of the ambient plasma,
²⁰⁴ as any magnetic field lines that thread a moving plasma are dragged along with it. This
²⁰⁵ assumption is valid throughout most of the magnetosphere — that is, the region of
²⁰⁶ space primarily governed by Earth’s magnetic field — and provides an invaluable tool
²⁰⁷ for understanding the large-scale motions of plasmas and fields.

2.1 The Outer Magnetosphere

Plasma behavior within Earth's magnetosphere is ultimately driven by the solar wind: a hot (~ 100 eV), fast-moving (~ 100 km/s) plasma threaded by the interplanetary magnetic field (~ 10 nT)¹. The density of the solar wind is on the order of 10^3 /cm³; in a laboratory setting, this would constitute an ultra-high vacuum (atmospheric density at sea level is $\sim 10^{19}$ /cm³), but compared to much of the magnetopause it's quite dense.

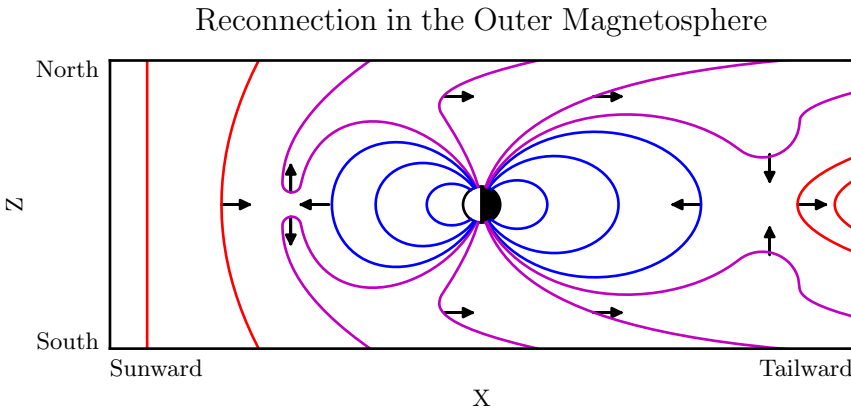


Figure 2.1: When the solar wind magnetic field (red) points southward, reconnection can occur between it and Earth's (northward) closed magnetic field lines (blue). The resulting open field lines (magenta) convect nightward over the poles, ultimately arriving in the magnetotail. There, the open field lines reconnect again. Newly closed field lines move Earthward, carrying flux across the flanks and back to the dayside. The rest are completely decoupled from Earth, and are lost to the solar wind.

The magnetosphere's outer boundary represents a balance between the solar wind dynamic pressure and the magnetic pressure of Earth's dipole field. On the dayside, the dipole is compressed, pushing this boundary to within about $10 R_E$ of Earth². The nightside magnetosphere is stretched into a long tail which may exceed $50 R_E$ in width and $100 R_E$ in length.

When the interplanetary magnetic field opposes the geomagnetic field at the nose of the magnetosphere, magnetic reconnection occurs. Closed magnetospheric field lines

¹Listed values correspond to the solar wind at Earth's orbit.

²Distances in the magnetosphere are typically measured in units of Earth radii: $1 R_E \equiv 6378$ km.

221 “break,” opening up to the interplanetary magnetic field³. They then move tailward
222 across the poles, dragging their frozen-in plasma with them. Reconnection in the tail
223 allows magnetic field lines to convect back to the day side, across the flanks. This
224 process is called the Dungey cycle[21].

Viewed from the north, the Dungey cycle involves a clockwise flow of flux and plasma on
the dusk side and a counterclockwise flow on the dawn side. The motion is accompanied
by a convection electric field, per Ohm’s law in an ideal plasma:

$$\underline{E} + \underline{U} \times \underline{B} = 0 \quad (2.1)$$

225 Where \underline{B} , \underline{E} , and \underline{U} are the magnetic field, electric field, and plasma velocity vectors
226 respectively.

227 Consistent with Ampère’s law, the interplanetary magnetic field is separated from the
228 magnetosphere by a current sheet: the magnetopause. On the dayside, the magne-
229 topause current flows duskward; on the nightside, it flows downward around the mag-
230 netotail.

231 Earth’s dipole is significantly deformed in the magnetotail; field lines in the northern
232 lobe of the tail points more or less Earthward, and vice versa. Plasma within the lobes
233 is cool (~ 100 eV) and rarefied ($\sim 10^{-2}$ /cm³). The two lobes are divided by the plasma
234 sheet, which is comparably hot ($\sim 10^3$ eV) and dense (~ 1 /cm³). The plasma sheet
235 carries a duskward current which connects to the magnetopause current.

³Closed field lines are more or less dipolar; one end connects to the north pole of Earth’s magnetic core, and the other end to the south pole. Open field lines are tethered to Earth at one end. In principle, the other end eventually doubles back to Earth, but for practical purposes it is lost to the solar wind. The distinction is important because charged particle motion is guided by magnetic field lines, as discussed in Chapter 3.

236 2.2 The Inner Magnetosphere

237 Within $L \sim 8$ (where L is the McIlwain parameter⁴), the dipole magnetic field is not
238 appreciably deformed by the solar wind. As a result, the structures in the inner mag-
239 netosphere follow closely from the motion of charged particles in an ideal dipole field.

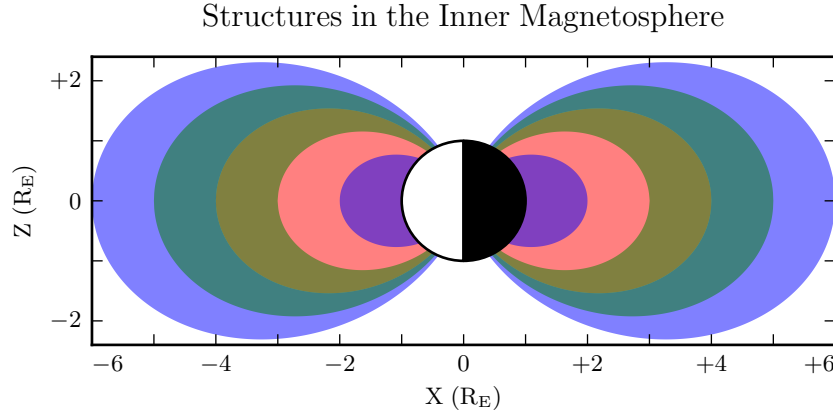


Figure 2.2: The above figure shows typical ranges in L for the plasmasphere (red, $L < 4$), ring current (green, $3 < L < 5$) and radiation belts (blue, $L < 2$ and $4 < L < 6$). These values, particularly the size of the plasmasphere, can vary significantly in response to geomagnetic activity.

240 The plasmasphere — a cold (~ 1 eV), dense ($10^2 / \text{cm}^3$ to $10^4 / \text{cm}^3$) torus of corotating
241 plasma — is formed by the outward drift of atmospheric ions along magnetic closed
242 field lines. Its outer boundary is thought to represent a balance between the corotation
243 electric field (per the rotation of Earth's magnetic dipole) and the convection electric
244 field (associated with the convection of magnetic flux during the Dungey cycle). Particle
245 density drops sharply at the edge of the plasmasphere; the boundary is called the
246 plasmapause. The plasmapause typically falls around $L = 4$, though during prolonged
247 quiet times it can extend to $L = 6$ or larger.

⁴The McIlwain parameter L is used to index field lines in Earth's dipole geometry: $L \equiv \frac{r}{\sin^2 \theta}$ for colatitude θ and radius r in Earth radii. For example, the $L = 5$ field line passes through the equatorial plane at a geocentric radius of $5 R_E$, then meets the Earth at a colatitude of $\arcsin \sqrt{\frac{1}{5}} \sim 27^\circ$ (equally, a latitude of $\arccos \sqrt{\frac{1}{5}} \sim 63^\circ$).

248 Energetic particles trapped within the inner magnetosphere are divided into two popu-
249 lations.

250 The Van Allen radiation belts are made up of particles with energy above 10^5 eV or
251 so. The inner belt ($L \lesssim 2$) is primarily composed of protons, the decay remnants of
252 neutrons freed from the atmosphere by cosmic rays. The outer belt ($L \gtrsim 4$) is primarily
253 composed of high-energy electrons. The density of radiation belt particles is significantly
254 affected by geomagnetic storms and substorms; a typical value is $10 / \text{cm}^3$.

255 Particles with energies of 10^3 eV to 10^5 eV make up the ring current, which extends
256 from $L \sim 3$ to $L \sim 5$. Gradient-curvature drift carries ions and electrons in opposite
257 directions; the net result is a westward current. During quiet times, the ring current
258 causes magnetic a southward magnetic field on the order of 1 nT at Earth's equator,
259 while during geomagnetically active times (discussed in Section 2.4) the effect may be
260 100 nT or more⁵.

261 2.3 The Ionosphere

262 Earth's neutral atmosphere is an excellent insulator. Collisions are so frequent that
263 charged particles quickly thermalize and recombine. The breakdown of air molecules
264 into a conductive plasma (as happens during a lightning strike, for example) requires
265 electric fields on the order of 10^9 mV/m.

266 Cold particles in the magnetosphere are likewise not conducive to currents. In the
267 absence of collisions, electrons and ions drift alongside one another in response to an
268 electric field, creating no net current perpendicular to the magnetic field⁶. Magnetic
269 field lines can typically be considered as equipotential contours, devoid of field-aligned
270 potential structures.

271 The ionosphere is a sweet spot between the two regimes. Collisions are frequent enough
272 to disrupt the drift of ions, but not frequent enough to immobilize the electrons. The

⁵For comparison, Earth's dipole field points north at the equator with a magnitude over 10^4 nT.

⁶The so-called E -cross- B drift is associated with a velocity of $\underline{U} = \frac{1}{B^2} \underline{E} \times \underline{B}$, independent of a charged particle's mass or sign.

273 result is a finite-valued conductivity tensor. Pedersen currents (which scale with the
274 Pedersen conductivity) flow in the direction of the perpendicular electric field. Hall
275 currents (due to the Hall conductivity) flow in the $\underline{B} \times \underline{E}$. It is these currents — par-
276 ticularly the Hall current — which give rise to magnetic fields at the ground. Collisions
277 in the ionosphere also result in a finite parallel conductivity, allowing for the formation
278 of potential structures along the magnetic field line.

279 The convection electric field (associated with the Dungey cycle, Section 2.1) drives
280 Pedersen currents in the ionosphere. Pedersen currents flow downward on the flanks
281 and duskward across the poles. The currents remain divergence-free by connecting
282 to field-aligned currents at the edges of the polar cap. The field-aligned currents, in
283 turn, connect to the magnetopause current, the cross-tail current, and the (partial) ring
284 current.

285 When electron density is low, thermal velocities may be unable to carry enough current
286 to satisfy $\nabla \cdot \underline{J} = 0$. This leads to the formation of potential structures along geomagnetic
287 field lines in the ionosphere. Such structures accelerate particles along magnetic field
288 lines, leading to the precipitation of energetic particles into the atmosphere. As the
289 particles thermalize, they excite atmospheric atoms. The resulting spontaneous emission
290 is often in the visible spectrum, giving rise to the aurora.

291 2.4 Geomagnetic Storms and Substorms

292 The quiet geomagnetic behavior described above is periodically disturbed by transient
293 solar phenomena such as corotating interaction regions (CIRs) and coronal mass ejec-
294 tions (CMEs). CMEs, such as the one that caused the Solar Storm of 1859 mentioned
295 in Chapter 1, are bursts of unusually dense solar wind which are ejected from regions of
296 high magnetic activity on the Sun; they are most common at the height of the eleven-
297 year solar cycle. CIRs, on the other hand, occur when a relatively fast region of the
298 solar wind catches up to an earlier and slower-moving pocket of solar wind, resulting in
299 a pair of shockwaves.

300 During a storm, increased solar wind intensity results in enhanced magnetic reconnection
301 on the dayside. As the newly-opened field lines are swept tailward, the convection
302 electric field is strengthened. The plasmasphere — the outer boundary of which is set by
303 a balance between the convection electric field and the (more or less constant) corotation
304 electric field — sheds its outer layers[33]. A large number of energetic particles are also
305 injected into the ring current[68].

306 The strength of the storm is gauged by the size of the magnetic perturbation created
307 by the ring current⁷. A small storm has a magnitude of 50 nT to 100 nT. Large storms
308 may reach 250 nT to 500 nT. The Carrington Event, mentioned in Chapter 1, is thought
309 to have exceeded 1700 nT[94].

310 The main phase of a storm typically lasts for several hours. Storm recovery — the
311 gradual return of the storm index to zero, and the refilling of the plasmasphere — lasts
312 several days. Geomagnetic storms occur tens of times per year at the height of the solar
313 cycle, and just a few times per year otherwise.

314 Whereas storms are prompted by large solar wind events on the dayside, geomagnetic
315 substorms are primarily a nightside occurrence. As flux accumulates in the tail, mag-
316 netic tension builds in the stretched field lines. A substorm is an impulsive release of
317 that tension.

318 At substorm onset, a burst of reconnection occurs in the tail. A jet of plasma is launched
319 Earthward from the reconnection site (and another is launched tailward, and lost to the
320 solar wind). The Earthward plasma injection injects particles into the ring current.
321 The outer radiation belt is depleted, then repopulated. Energetic particles precipitate
322 into the atmosphere, giving rise to a distinctive sequence of auroral signatures over the
323 course of about an hour.

324 Concurrent with substorm onset, impulsive Alfvén waves are observed with periods of
325 a minute or two. The precise ordering of events — whether reconnection causes the
326 waves, or vice versa, or if they share a common cause — remains controversial.

⁷The most commonly used storm index is Dst, which is computed hourly using measurements from several ground magnetometers near the equator. The Sym-H index, used in Section 5.3, is computed once per minute.

327 Each substorm lasts several hours, including the time it takes for the ring current to
328 return to pre-substorm levels. Several substorms may occur per day during quiet times.
329 During a storm, substorms become far more frequent; by the time one has ended,
330 another may have already begun.

³³¹ **Chapter 3**

³³² **Field Line Resonance**

³³³ The motion of a charged particle in a dipole field can be described in terms of three
³³⁴ fundamental motions.

³³⁵ The first is cyclotron motion. Given a uniform magnetic field line, a particle follows a
³³⁶ helical path. It moves in a circular path in a plane normal to the magnetic field line,
³³⁷ and keeps a constant velocity along the direction of the field. Close to Earth, where the
³³⁸ magnetic field is strongest, the proton (electron) cyclotron timescale is on the order of
³³⁹ 10^{-3} s (10^{-6} s); at $L \sim 5$, a typical value is closer to 10 s (10^4 s).

³⁴⁰ The second fundamental motion is bounce motion. As it moves along the magnetic field
³⁴¹ line like a bead on a wire, the particle experiences a change in magnetic field magnitude.

³⁴² In order to conserve its magnetic moment (also called the first adiabatic invariant), the
³⁴³ particle's perpendicular kinetic energy increases in proportion with the magnetic field.

³⁴⁴ When the perpendicular kinetic energy can no longer increase — that is, when all of
³⁴⁵ the particle's kinetic energy is perpendicular — the particle bounces back. Particles
³⁴⁶ undergoing bounce motion continuously move back and forth between the northern and
³⁴⁷ southern hemispheres, with timescales of a few seconds to a few minutes.

³⁴⁸ Particles with more parallel kinetic energy (compared to their perpendicular kinetic
³⁴⁹ energy) bounce at lower altitudes. If the particle's motion is sufficiently field-aligned, the

350 bounce altitude drops into the atmosphere, and the particle is collisionally thermalized.

351 This process is called precipitation.

352 The third fundamental motion is drift motion. Over the course of a particle's cyclotron
353 motion, the Earthward half of the orbit experiences a slightly stronger magnetic field
354 (and thus a slightly smaller orbit radius). The net effect, called the gradient-curvature
355 drift, is an azimuthal motion around Earth on timescales of $\sim 10^3$ s.

356 Wave-particle resonance arises when a particle's periodic motion matches with the fre-
357 quency of a coincident electromagnetic wave[23, 64, 73, 83]. In the particle's rest frame,
358 the wave then appears as a net electric field. This allows a net movement of energy
359 between the wave and the particle. The interaction is analogous to a surfer moving
360 along with — and being accelerated by — a wave in the ocean. Such resonance can
361 arise for any of the three fundamental motions, or even for a combination of them.

362 In the present work, the waves under consideration are field line resonances (FLRs). An
363 FLR is a standing harmonic on a geomagnetic field line. It can also be envisioned as
364 a superposition of traveling waves, reflecting back and forth between its northern and
365 southern foot points at the conducting ionosphere.

These waves travel at the Alfvén speed, v_A , defined per

$$v_A^2 \equiv \frac{B^2}{\mu_0 \rho} \quad \text{or, equally,} \quad v_A^2 \equiv \frac{1}{\mu_0 \epsilon_{\perp}} \quad (3.1)$$

366 Where B is the magnetic field magnitude, ρ is the mass density, and μ_0 is the magnetic
367 constant. The perpendicular electric constant ϵ_{\perp} is analogous to the electric constant
368 ϵ_0 , and arises in cases (such as the magnetosphere) where a dielectric medium exhibits
369 a preferred direction. In the magnetosphere, mass density and magnetic field strength
370 depend strongly on position. As a result, the Alfvén speed varies by several orders
371 of magnitude over the length of a field line. The fundamental equations of field line
372 resonance were presented by Dungey in 1954[20]. Since then, they have remained a
373 topic of active study.

374 So-called ultra low frequency waves — of which FLRs are a subset — are categorized
 375 by morphology. Continuous (long-lived) pulsations are termed Pc, while irregular pulsations
 376 are called Pi. Within each are a number of frequency bands; see Table 3.1[44].
 377 In practice, frequency demarcations are not strict, but rather serve as a heuristic for
 378 grouping phenomenologically similar waves[41].

Table 3.1: IAGA Magnetic Pulsation Frequency Bands

	Pc1	Pc2	Pc3	Pc4	Pc5	Pi1	Pi2
Period (s)	0.2–5	5–10	10–45	45–150	150–600	1–40	40–150
Frequency (mHz)	200–5000	100–200	22–100	7–22	2–7	25–1000	7–25

379 FLRs fall into the Pc3, Pc4, and Pc5 ranges. The present work focuses specifically
 380 on the Pc4 band: waves with periods of a minute or two. Frequencies in the Pc4
 381 range typically coincide with Alfvén bounce times¹ near the plasmapause: $L \sim 4$ to
 382 $L \sim 6$ [2, 16, 24, 56]². In fact, the large radial gradients in the Alfvén speed near the
 383 plasmapause act as an effective potential well, trapping FLRs[15, 49, 53, 54, 63, 86].

384 In addition to being radially localized, FLRs in the Pc4 frequency band (also called Pc4
 385 pulsations, or just Pc4s) are localized in magnetic local time (MLT³). They have also
 386 been shown to occur preferentially on the dayside, during storms or storm recovery[2,
 387 16, 24, 52, 56, 95].

388 In the inner magnetosphere, the Alfvén frequency — and thus the frequency of FLRs
 389 — often coincides with integer or half-integer⁴ multiples of particle drift frequencies[17].
 390 The resulting wave-particle interactions can give rise to significant energization and ra-
 391 dial diffusion of the particles. In some cases, the waves also include an electric field
 392 parallel to the background magnetic field, breaking the assumption that magnetic field

¹The Alfvén frequency is the inverse of the Alfvén bounce time: $\frac{2\pi}{\omega_A} \equiv \oint \frac{dz}{v_A}$.

²Not coincidentally, these are the same L -shells where the Van Allen Probes spend most of their time; see Chapter 8.

³Noon points toward the Sun and midnight away from it, with 06:00 and 18:00 at the respective dawn and dusk flanks.

⁴See Section 3.1.

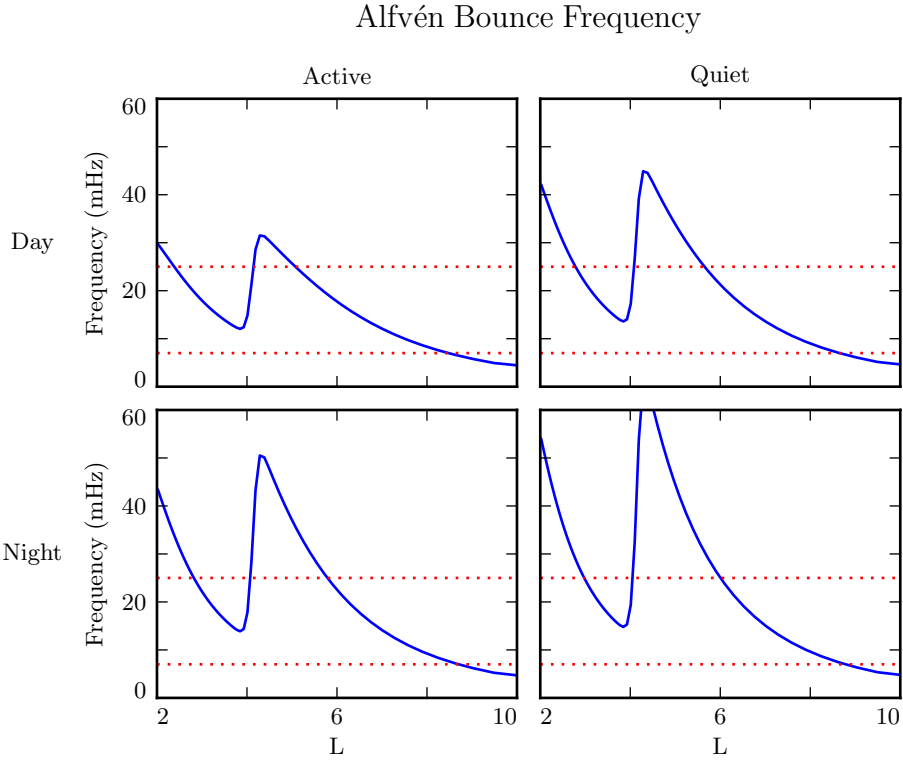


Figure 3.1: The above are bounce frequencies for an Alfvén wave moving back and forth along a geomagnetic field line. Alfvén speeds are computed based on profiles from Kelley[47], as discussed in Section 5.2. Notably, the bounce frequency depends significantly on the position of the plasmasphere, taken here to be at $L = 4$. Dotted lines indicate the P_{c4} frequency range: 7 mHz to 25 mHz.

393 lines are equipotential contours, and contributing to the precipitation of energetic par-
 394 ticles into the neutral atmosphere[31, 32, 92, 101].

395 The present chapter introduces the structural characteristics of FLRs, how those charac-
 396 teristics affect wave behavior, and several unresolved questions related to that behavior.

397 **3.1 Harmonic Structure**

398 Wave structure along a geomagnetic field line is indicated by harmonic number. The
399 first (or fundamental) harmonic has a wavelength twice as long as the field line. The
400 electric field perturbation is zero at the ionospheric foot points of the field line, due to
401 the conductivity of the ionosphere. For the first harmonic, this puts an electric field
402 antinode at the equator, along with a node in the perpendicular⁵ perturbation to the
403 magnetic field. For the second harmonic, the electric field has a third node at the
404 equator, in addition to the two at the ionospheric foot points, which is accompanied by
405 an antinode in the perpendicular wave magnetic field. Figure 3.2 shows a qualitative
406 sketch of the first and second harmonics: a series of snapshots in time, in the rest frame
407 of the wave. Perpendicular electric and magnetic field perturbations are shown in blue
408 and red respectively.

409 A first-harmonic FLR that is periodic or localized in the azimuthal direction is conducive
410 to drift-resonant wave-particle interactions[17, 74]. The particle is like a child on a swing:
411 whenever the path of the particle (or child) gets close to the wave (parent), it gets a
412 push, and always in the same direction. The wave fields spend half its time pointing
413 the other direction, just as the parent must shift their weight backward to get ready for
414 the next push, but at that point the particle (child) is far away.

415 Second-harmonic FLRs interact with particles through the drift-bounce resonance, which
416 is slightly more complicated. As the particle drifts azimuthally, it also zig-zags north-
417 south. The combination of those two periodic motions must align with the phase of
418 the wave electric field. An example path is shown by the purple line in Figure 3.2:
419 the particle's drift and bounce motions together ensure that it experiences a rightward
420 electric field throughout the wave's oscillation.

The drift and drift-bounce resonance conditions is written, respectively[87]:

$$\omega - m\omega_D = 0 \quad \text{and} \quad \omega - m\omega_D = \omega_B \quad (3.2)$$

⁵The parallel, or compressional, wave magnetic field exhibits the same nodes and antinodes as the perpendicular electric field[76].

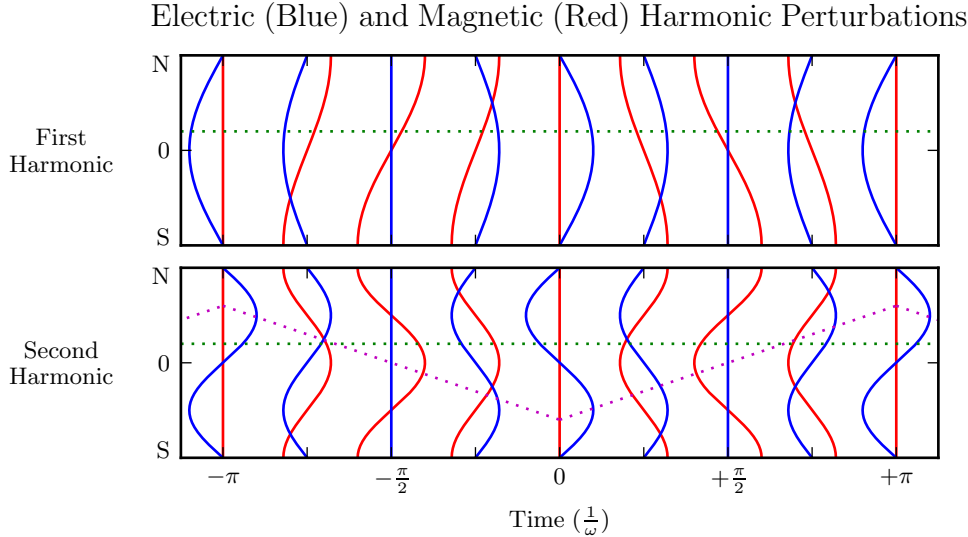


Figure 3.2: The first (or fundamental) harmonic has an antinode in its perpendicular electric field (blue) at the equator, along with a node in its perpendicular magnetic field perturbation (red). A single satellite can identify the first harmonic by the relative phase of the electric and magnetic field perturbations: an observer north of the equator (green) will see the magnetic field perturbation lead the electric field by $\pm 90^\circ$. The second harmonic is the opposite: it has an electric field node at the equator, and an observer north of the equator will see the magnetic field perturbation lag the electric field by $\mp 90^\circ$. Top and bottom signs correspond to the poloidal (shown) and toroidal polarizations respectively. The purple line sketches the path of a particle in drift-bounce resonance; in the particle's rest frame, the electric field is always to the right.

- 421 Where ω is the frequency of the wave, ω_D and ω_B are the particle's drift and bounce
- 422 frequencies respectively, and m is the wave's azimuthal modenumber, as discussed in
- 423 Section 3.2.
- 424 In principle, the first and second harmonics can be distinguished by their frequencies,
- 425 even from a single-point observation[2, 14, 34]. In practice, however, this is not a reliable
- 426 approach[88]. Significant uncertainties surround the mass density profile — and thus
- 427 the Alfvén speed profile — along a geomagnetic field line.
- 428 Harmonic structure can also be deduced by noting the phase offset between the wave
- 429 magnetic field and its electric field (or the plasma velocity)[16, 91]. In Figure 3.2, the
- 430 green line indicates an observer just north of the magnetic equator. For a wave polarized

431 in the poloidal direction (see Section 3.3), the observer sees the electric field waveform
432 offset from the magnetic field by a phase of $\pm 90^\circ$, where the top sign is for odd modes
433 and the bottom sign is for even modes. The signs are flipped for toroidally-polarized
434 waves, and again for waves observed south of the equator.

435 In addition to a wave's parity, the phase indicates how energy is divided between stand-
436 ing and traveling waves. Standing waves (phase of $\pm 90^\circ$) have a purely imaginary
437 Poynting flux. Traveling waves (phase of 0° or 180°), on the other hand, have real
438 Poynting flux, indicating a net movement of energy. Wave lifetimes can be estimated
439 by comparing the energy density to the rate at which that energy is carried away by
440 Poynting flux, as is done in Chapter 8.

441 Notably, the measurement of wave phase has only become viable with the advent of
442 satellites carrying both electric and magnetic field instrumentation, such as THEMIS in
443 2007[3] and the Van Allen Probes (formerly RBSP, for Radiation Belt Storm Probes)
444 in 2012[84].

445 Strictly speaking, the the phase offset of the electric and magnetic fields does not provide
446 the harmonic number — only its parity. It's reasonably safe to assume that an even mode
447 is the second harmonic; the second harmonic is by far the most commonly observed[43,
448 81, 89], due in part to its excitement by the antisymmetric balloon instability[9, 11,
449 12, 83]. However, the distinction between the first and third harmonics is not always
450 clear[13, 34]; this issue is discussed further in Chapter 8. Higher harmonics than that
451 are not expected in the Pc4 frequency band.

452 **3.2 Azimuthal Modenumber**

453 The wavelength of an FLR in the azimuthal direction is indicated by its azimuthal
454 modenumber. A wave with modenumber m has an azimuthal wavelength that spans $\frac{24}{m}$
455 hours in MLT.

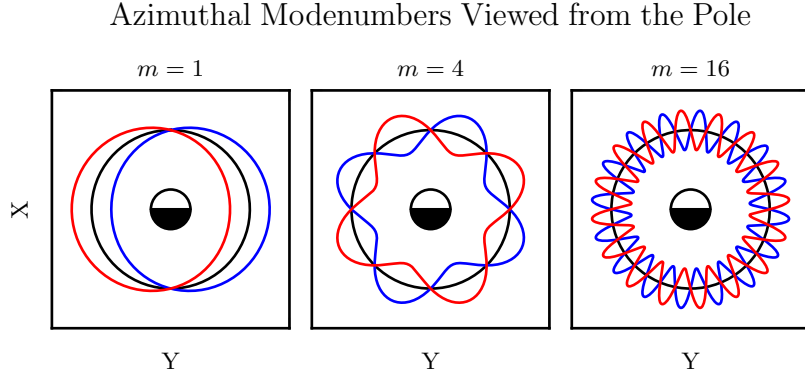


Figure 3.3: Above are qualitative sketches of waves with azimuthal modenumbers 1, 4, and 16, projected into the ecliptic plane. Black circles show unperturbed fields, while the blue and red curves show perturbations. At $m = 1$, the wave is more or less a uniform displacement, while at $m = 16$ azimuthal variations take place on spatial scales small compared to Earth's radius.

- 456 Waves with small azimuthal modenumbers ($0 < m < 10$) are typically driven by broad-
 457 band energy sources at the magnetosphere's boundary, such as variations in the so-
 458 lar wind pressure[18, 38, 48, 104, 105], sporadic magnetic reconnection[41], or Kelvin-
 459 Helmholtz waves on the magnetopause[10, 57, 82]. In the low- m regime, the shear and
 460 compressional Alfvén waves are coupled, which allows energy to move across field lines
 461 until the driving frequency lines up with the local Alfvén frequency[59]. Because of their
 462 broadband energy source, low- m FLRs often have a mishmash of frequencies present in
 463 their spectra[16], though the spectra are coherent in terms of harmonic[25].
- 464 When the azimuthal modenumber is large (or, equally, when the azimuthal wavelength
 465 is small), compressional propagation of Alfvén waves becomes evanescent, so the move-
 466 ment of energy is guided by magnetic field lines[14, 76]⁶. As a result, FLRs must be
 467 driven from within the magnetosphere. Proposed energy sources include phase space
 468 gradients near the plasmapause[17], particularly as the plasmasphere refills after a storm
 469 or substorm[24, 55].

⁶Equally, the strength of a wave's parallel component indicates its modenumber, a point which is revisited in Chapters 7 and 8.

470 The atmosphere is known to attenuate waves with small spatial extent in the perpendicular
471 direction[42, 99, 103]. As a result, FLRs may create no signature on the ground if
472 their azimuthal modenumber is large. For example, a recent paper by Takahashi shows
473 a strong (2 nT at $L \sim 10$), clear resonance with $|m| \gtrsim 70$ and no corresponding ground
474 signature[88].

Southwood[83] and Glassmeier[29] show that a low frequency wave passing through the ionosphere on its way to Earth will be attenuated per

$$\frac{B_E}{B_I} = \frac{\Sigma_H}{\Sigma_P} \exp\left(-m \frac{R_I - R_E}{R_E \sin \theta}\right) \quad (3.3)$$

475 Where B_E and B_I are the magnetic field strengths at R_E (Earth's surface, 6783 km
476 geocentric) and R_I (the ionosphere, \sim 6900 km geocentric) respectively. The integrated
477 ionospheric Pedersen and Hall conductivities, Σ_P and Σ_H , are typically within a factor
478 of two of one another. Field lines near the plasmapause can be traced to Earth at
479 $\sin \theta \sim 0.4$. That is, by the time it reaches the ground, the magnetic field from an FLR
480 with $m = 10$ is weaker by a factor of two; at $m = 100$, the factor is closer to 100.

481 3.3 Poloidal and Toroidal Polarizations

482 Based on polarization, each FLR can be classified as either poloidal or toroidal. The
483 poloidal mode is a field line displacement in the meridional plane, as shown in Figure 3.4,
484 with an accompanying electric field in the azimuthal direction. The toroidal mode's
485 magnetic displacement is azimuthal, per Figure 3.5; the associated electric field is in the
486 meridional plane.

487 Both poloidal and toroidal waves are noted for their ability to contribute to the energiza-
488 tion and radial diffusion of trapped particles. The poloidal mode interacts more strongly,
489 since its electric field is aligned with the trapped particles' drift motion. Poloidally-
490 polarized waves are also more prone to creating magnetic signatures on the ground, due
491 to ducting in the ionosphere[27, 36].

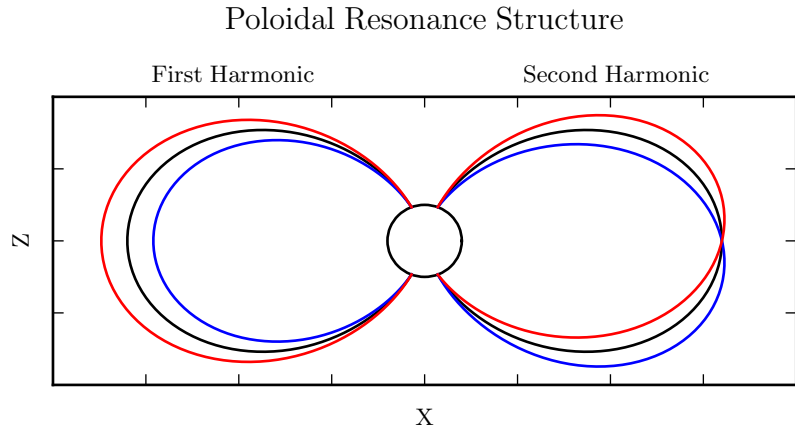


Figure 3.4: The poloidal resonance is a magnetic field in the meridional plane. The displacement is radial near the equator, and can be accompanied by enhancement in the parallel magnetic field near the ionosphere. The first harmonic is shown on the left, and the second harmonic on the right. Lines are colored red and blue only to contrast with the unperturbed black field line.

- 492 Toroidal modes have been shown to outnumber poloidal modes[2]. Perhaps not co-
 493 incidentally, poloidally-polarized waves rotate asymptotically to the toroidal mode[65,
 494 66, 76]. Poloidal waves with low azimuthal modenumber — such as those driven by
 495 broadband sources at the magnetopause — rotate on timescales comparable to their
 496 oscillation periods. The two modes are also coupled directly by the ionospheric Hall
 497 conductivity[46].
- 498 The eigenfrequencies for poloidal and toroidal FLRs are similar, though not identical[34].
 499 It has furthermore been noted that toroidally-polarized waves exhibit a strong relation-
 500 ship between frequency and L -shell (or latitude), while poloidal waves at fixed frequency
 501 are spread more broadly in L [25].

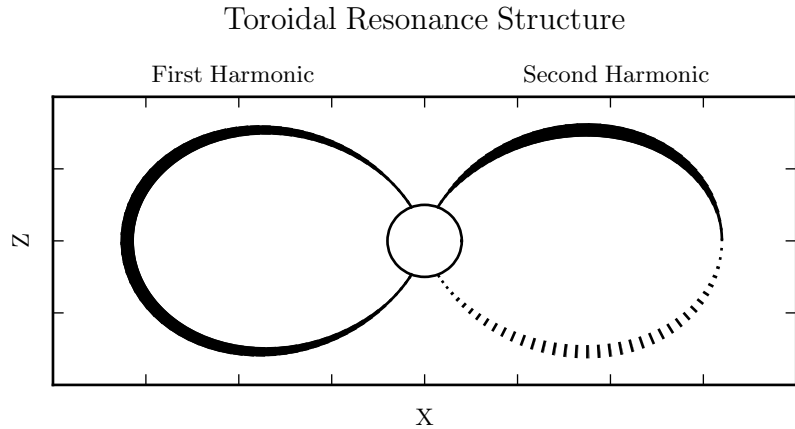


Figure 3.5: A toroidally-polarized FLR has a magnetic perturbation in the azimuthal direction, as shown. Bold lines are taken to be above the page, and dotted lines below the page, with the displacement indicated by the line’s width. The first harmonic — where the entire field line oscillates in and out of the page — is shown on the left. The second harmonic is on the right, with northern and southern halves perturbed in opposite directions.

502 3.4 Giant Pulsations

503 The study of geomagnetic pulsations long predates satellites, sounding rockets, or even
504 the word “magnetohydrodynamics”⁷. Large, regular oscillations in the magnetic field
505 were noted as early as 1901[5]. Eventually, the term “giant pulsation,” or Pg, arose to
506 describe such pulsations.

507 On the ground, Pgs are notable for their strikingly sinusoidal waveforms, their eastward
508 drifts, and their specific occurrence pattern: Pgs are typically seen pre-dawn, at latitudes
509 of 60° to 70° . Pgs generally fall into the Pc4 frequency band⁸. Their harmonic structure
510 was a source of controversy for decades, but recent multisatellite observations seem to be
511 in agreement that they are odd harmonics, probably fundamental[30, 40, 51, 52, 87, 91].
512 They are poloidally polarized, with modenumbers $10 \lesssim m \lesssim 40$ [28, 40, 74, 79, 91].

⁷The term was first used by Alfvén in the 1940s[1].

⁸The Pc4 range is periods of 45 s to 140 s, while Pgs range from 60 s to 200 s[7].

513 Whereas FLRs are waves in space which may produce ground signatures, “giant pulsation” refers to the ground signature specifically⁹. That is, Takahashi’s satellite observation of a sinusoidal, morningside, high- m , fundamental poloidal resonance was not 516 classified as a Pg because it did not produce a signal on the ground[88].

517 Due to their remarkably clear waveforms, Pgs are typically found by “visual inspection 518 of magnetometer data”[69]. Over the course of the past century, a number of multi-year 519 (sometimes multi-decade[7]) surveys have totaled nearly one thousand Pg events. On 520 average, a ground magnetometer near 66° magnetic latitude observes \sim 10 Pg events per 521 year[7, 39, 78, 85]. Observations are not distributed uniformly; rather, giant pulsations 522 are most common near the equinox and during times of low solar activity.

523 Unlike Pc4 pulsations in general, Pgs show no particular correlation with storm phase[69]. 524 However, they do often occur as the magnetosphere recovers from a substom[69, 79].

525 3.5 Motivations for the Present Work

526 A great deal has been learned — and continues to be learned — through observations of 527 field line resonance. However, the cost-to-benefit ratio is climbing. As summarized in the 528 sections above, FLR behavior depends significantly on harmonic structure, azimuthal 529 modenumber, and polarization — not to mention frequency, spectral width, and so 530 on. With each degree of freedom comes the necessity for an additional simultaneous 531 observation.

532 Similarly, as FLRs have been shown to depend on ever-more-specific magnetospheric 533 conditions, analytical techniques have fallen out of favor. The height-resolved iono- 534 sphere, multidimensional Alfvén speed profile, and inconvenient geometry combine to 535 create a problem beyond the reasonable purview of pencil and paper.

536 That is, the topic of field line resonance is ripe for numerical modeling.

⁹Historically, the wave designations shown in Table 3.1 all referred to ground phenomena. Over time, they have come to describe satellite observations as well, including those without corresponding signatures on the ground.

537 Past models of the magnetosphere have been limited in their consideration of FLRs.
538 Reasons include overly-simplified treatment of the ionospheric boundary, no consider-
539 ation of the plasmapause, limited range in m , and the inability to compute ground
540 signatures. Chapter 5 presents a model which addresses these issues, allowing the com-
541 putation of field line resonance with unparalleled attention to realism.

542 The model allows a bird’s-eye view of the structure and evolution of FLRs. As such,
543 not only can several open questions be addressed, but their answers serve to unify a
544 number of seemingly-disparate properties described in the sections above.

545 The rotation of poloidally-polarized waves to the toroidal mode is investigated. Par-
546 ticular attention is paid to the importance of azimuthal modenumber and ionospheric
547 conductivity. The interplay between said rotation and the transport of energy across
548 field lines — which also depends on azimuthal modenumber — is considered as well.

549 By their nature, drifting particles have the potential to spur wave-particle interactions
550 at all MLT. However, Pc4 observations are strongly peaked on the dayside. In a 2015
551 paper, Dai notes, “It is not clear why noncompressional [high- m] Pc4 poloidal waves,
552 which are presumably driven by instability within the magnetosphere, preferentially
553 occur on the dayside”[16]. Motoba, later that year, echoes, “It is unclear whether other
554 generation mechanisms of fundamental standing waves ... can explain the localization
555 of Pgs in local time”[69]. This, too, is considered numerically: to what degree is field
556 line resonance affected by the (day-night asymmetric) conditions of the ionosphere?

557 An attempt is also made to demystify giant pulsations. It’s been shown that toroidal
558 Pc4s outnumber poloidal ones, and that most poloidal Pc4s are even, so perhaps it
559 should come as no surprise that (poloidal, odd) Pgs are rare. Is it truly the case that
560 Pgs are only “a small subset of fundamental poloidal waves”[88], set apart from the rest
561 by their distinctive properties? Or, said another way, to what degree do the properties
562 associated with Pgs arise in fundamental poloidal waves overall?

563 **Chapter 4**

564 **Waves in Cold Resistive Plasma**

565 Before delving into the implementation of the numerical model, it's instructive to con-
566 sider the fundamental equations of waves in a cold, resistive plasma. Specifically, the
567 present chapter is concerned with waves much slower than the electron cyclotron fre-
568 quency. High-frequency waves such as the L and R modes are beyond the scope of the
569 present work — and, in fact, beyond the limits of the model described in Chapter 5.

The evolution of electric and magnetic fields is governed by Ampère's law and Faraday's law. Notably, the present work takes the linearized versions of Maxwell's equations; the vectors \underline{E} and \underline{B} indicate perturbations above the zeroth-order magnetic field.

$$\underline{\epsilon} \cdot \frac{\partial}{\partial t} \underline{E} = \frac{1}{\mu_0} \nabla \times \underline{B} - \underline{J} \quad \frac{\partial}{\partial t} \underline{B} = -\nabla \times \underline{E} \quad (4.1)$$

Current follows Ohm's law. For currents perpendicular to the background magnetic field, Kirchhoff's formulation is sufficient. Conductivity is much higher along the magnetic field lines¹, so it's appropriate to also include the electron inertial term².

$$0 = \underline{\sigma}_{\perp} \cdot \underline{E}_{\perp} - \underline{J}_{\perp} \quad \frac{1}{\nu} \frac{\partial}{\partial t} J_z = \sigma_0 E_z - J_z \quad (4.2)$$

¹The dipole coordinate system is defined rigorously in Section 5.1; at present, it's sufficient to take \hat{z} parallel to the zeroth-order magnetic field, and \hat{x} and \hat{y} perpendicular to \hat{z} (and to each other).

²Electron inertial effects are not included in the model described in Chapter 5, or in the results in Chapter 7; however, their implementation and impact are explored in Chapter 6.

Derivatives in Equations (4.1) and (4.2) can be evaluated by performing a Fourier transform. They can then be combined, eliminating the magnetic field and current terms.

$$\begin{aligned} 0 &= \underline{\underline{E}}_{\perp} + \frac{v_A^2}{\omega^2} (\underline{k} \times \underline{k} \times \underline{E})_{\perp} + \frac{i}{\epsilon_{\perp}\omega} \underline{\sigma}_{\perp} \cdot \underline{\underline{E}}_{\perp} \\ 0 &= E_z + \frac{c^2}{\omega^2} (\underline{k} \times \underline{k} \times \underline{E})_z + \frac{i\omega_P^2}{\omega(\nu - i\omega)} E_z \end{aligned} \quad (4.3)$$

The speed of light, Alfvén speed (including the displacement current correction), plasma frequency, and parallel conductivity are defined in the usual way:

$$c^2 \equiv \frac{1}{\mu_0\epsilon_0} \quad v_A^2 \equiv \frac{1}{\mu_0\epsilon_{\perp}} \quad \omega_P^2 \equiv \frac{ne^2}{m_e\epsilon_0} \quad \sigma_0 \equiv \frac{ne^2}{m_e\nu} \quad (4.4)$$

Where the perpendicular dielectric constant ϵ_{\perp} is analogous to the electric constant ϵ_0 , but for electric fields which are perpendicular to the preferred direction of the dielectric medium. As noted in Equation (3.1), $\epsilon_{\perp} \equiv \frac{\rho}{B^2}$ where ρ is the mass density and B is the magnitude of the (zeroth-order) magnetic field.

Using the vector identity $\underline{k} \times \underline{k} \times \underline{E} = \underline{k} \underline{k} \cdot \underline{E} - k^2 \underline{E}$, Equation (4.3) can be reassembled into a single expression,

$$0 = \left(\underline{\underline{\mathbb{I}}} + \frac{1}{\omega^2} \underline{\underline{V}}^2 \cdot \underline{k} \underline{k} - \frac{k^2}{\omega^2} \underline{\underline{V}}^2 + \frac{i}{\omega} \underline{\underline{\Omega}} \right) \cdot \underline{\underline{E}} \quad (4.5)$$

Where $\underline{\underline{\mathbb{I}}}$ is the identity tensor and in x - y - z coordinates,

$$\underline{\underline{V}}^2 \equiv \begin{bmatrix} v_A^2 & 0 & 0 \\ 0 & v_A^2 & 0 \\ 0 & 0 & c^2 \end{bmatrix} \quad \text{and} \quad \underline{\underline{\Omega}} \equiv \begin{bmatrix} \frac{\sigma_P}{\epsilon_{\perp}} & \frac{-\sigma_H}{\epsilon_{\perp}} & 0 \\ \frac{\sigma_H}{\epsilon_{\perp}} & \frac{\sigma_P}{\epsilon_{\perp}} & 0 \\ 0 & 0 & \frac{\omega_P^2}{(\nu - i\omega)} \end{bmatrix} \quad (4.6)$$

The parenthetical expression in Equation (4.5) is the dispersion tensor. Nontrivial solutions exist only when its determinant is zero. This gives rise to a seventh-order polynomial in ω , so rather than a direct solution it's necessary to consider limits of specific interest.

578 In these limits, as explored in the sections below, the wave vector \underline{k} is taken — without
 579 loss of generality — to lie in the x - z plane (that is, k_y is taken to be zero). The distinction
 580 between the two perpendicular components (k_x and k_y) is discussed in Section 4.4.

581 4.1 Guided Propagation

582 The wave vector of a field line resonance aligns closely to the background magnetic
 583 field. By supposing that the two align exactly (that is, taking $k_x = 0$), the parallel and
 584 perpendicular components of the dispersion relation are decoupled.

The parallel-polarized component ($E_x = E_y = 0$) is quadratic, and thus can be solved directly.

$$0 = \omega^2 + i\nu\omega - \omega_P^2 \quad \text{so} \quad \omega = -\frac{i\nu}{2} \pm \sqrt{\omega_P^2 - \frac{\nu^2}{4}} \quad (4.7)$$

It bears noting that the plasma frequency is large — not just compared to Pc4 frequencies, but even compared to the collision frequencies in the ionosphere³. Expanding Equation (4.7) with respect to large ω_P , the dispersion relation becomes

$$\omega^2 = \omega_P^2 \pm i\nu\omega_P + \dots \quad (4.8)$$

585 Equation (4.8) can hardly be called a wave, as it does not depend on the wave vector
 586 \underline{k} . Rather, it is the plasma oscillation⁴: electrons vibrating in response to a charge
 587 separation along the background magnetic field.

588 The plasma oscillation is not specifically relevant to the study of field line resonance.
 589 The two phenomena are separated by six orders of magnitude in frequency. The topic
 590 is revisited in Chapter 6 insomuch as it is inseparable from the electron inertial effects
 591 in Ohm’s law, but it is otherwise not relevant to the work at hand.

³The collision frequency may match or exceed the plasma frequency for a thin slice at the bottom of the ionosphere, where the density of neutral atoms is large; however, it falls off quickly. Above an altitude of 200 km, conservatively[72], the plasma frequency exceeds the collision frequency by an order of magnitude or more.

⁴The plasma oscillation is also called the Langmuir wave.

The perpendicular ($E_z = 0$) components of the dispersion relation give an expression quartic in ω .

$$0 = \omega^4 + 2i\frac{\sigma_P}{\epsilon_\perp}\omega^3 - \left(2k_z^2v_A^2 + \frac{\sigma_P^2 + \sigma_H^2}{\epsilon_\perp^2}\right)\omega^2 - 2ik_z^2v_A^2\frac{\sigma_P}{\epsilon_\perp}\omega + k_z^4v_A^4 \quad (4.9)$$

Like the parallel-polarized component above, Equation (4.9) can be solved directly. Noting that \pm and \oplus are independent,

$$\omega = \left(\frac{\pm\sigma_H - i\sigma_P}{2\epsilon_\perp}\right) \oplus \sqrt{k_z^2v_A^2 + \left(\frac{\pm\sigma_H - i\sigma_P}{2\epsilon_\perp}\right)^2} \quad (4.10)$$

Also like the parallel-polarized component, the exact solution is less useful than its Taylor expansion. The Pedersen and Hall conductivities are large near the ionospheric boundary, but fall off quickly; for the vast majority of the field line, the ratios $\frac{\sigma_P}{\epsilon_\perp}$ and $\frac{\sigma_H}{\epsilon_\perp}$ are small compared to field line resonance frequencies. Expanding with respect to small conductivity gives

$$\omega^2 = k_z^2v_A^2 \oplus k_zv_A\frac{\sigma_H \pm i\sigma_P}{\epsilon_\perp} + \dots \quad (4.11)$$

592 This is the shear Alfvén wave, with a shift in its frequency proportional to the character-
 593 istic conductivity of the ionosphere⁵. The wave travels along the background magnetic
 594 field like a bead on a string, with electric and magnetic field perturbations perpendicular
 595 to the magnetic field line (and to one another).

596 4.2 Compressional Propagation

597 The partner to guided motion is compressional motion; in order for energy to move
 598 across field lines, the wave vector must have a component perpendicular to \hat{z} . If the

⁵Admittedly, it's difficult to say what constitutes a characteristic conductivity. The Pedersen and Hall conductivities vary by several orders of magnitude within the ionosphere, then drop essentially to zero at large radial distance.

599 wave vector is completely perpendicular to the magnetic field line ($k_z = 0$), the parallel
 600 and perpendicular components of the dispersion relation decouple, as in Section 4.1.

The parallel-polarized ($E_x = E_y = 0$) component of the dispersion relation is

$$0 = \omega^3 + i\nu\omega^2 - (k_x^2 c^2 + \omega_P^2) \omega - ik_x^2 c^2 \nu \quad (4.12)$$

Equation (4.12) can be solved directly, though its solution (as a cubic) is far too long to be useful. Expanding with respect to the large plasma frequency, gives

$$\omega^2 = k^2 c^2 + \omega_P^2 - i\nu\omega_P + \dots \quad (4.13)$$

601 This is the O mode, a compressional wave with an electric field perturbation along
 602 the background magnetic field. Like the plasma oscillation discussed in Section 4.1, its
 603 frequency is very large compared to that of a field line resonance, putting it beyond the
 604 concern of the present work.

The perpendicular-polarized ($E_z = 0$) component of the compressional dispersion relation is also cubic.

$$0 = \omega^3 + 2i\frac{\sigma_P}{\epsilon_\perp}\omega^2 - \left(2k_x^2 v_A^2 + \frac{\sigma_P^2 + \sigma_H^2}{\epsilon_\perp^2}\right) \omega - ik_x^2 v_A^2 \frac{\sigma_P}{\epsilon_\perp} \quad (4.14)$$

A wave moving across magnetic field lines near the ionospheric boundary will encounter large $\frac{\sigma_P}{\epsilon_\perp}$ and $\frac{\sigma_H}{\epsilon_\perp}$, while at moderate to high altitudes those ratios will be small. Solving Equation (4.14) in those two limits respectively gives:

$$\omega^2 = k_x^2 v_A^2 \pm ik_x v_A \frac{\sigma_P}{\epsilon_\perp} + \dots \quad \text{and} \quad \omega^2 = k_x^2 v_A^2 + \left(\frac{\sigma_H \pm i\sigma_P}{\epsilon_\perp}\right)^2 + \dots \quad (4.15)$$

605 At first glance, both limits of Equation (4.15) appear to describe compressional Alfvén
 606 waves. The magnetic perturbation is along the background magnetic field — indicating
 607 compression of the frozen-in plasma — while the electric field perturbation is perpen-
 608 dicular to both the magnetic field and the wave vector.

609 However, in the high-conductivity limit, the parenthetical term actually dominates the
 610 Alfvén term, taking values as large as $\sim 10^6$ Hz. Waves at such frequencies are beyond
 611 the scope of the present work. As a matter of interest, however, it bears noting that —
 612 as long as $\nu \ll 10^6$ Hz — $\frac{\sigma_H}{\epsilon_{\perp}}$ reduces to the electron cyclotron frequency, $\frac{eB}{m_e}$.

613 4.3 High Altitude Limit

614 In the limit of large radial distance, it's reasonable to take the collision frequency to
 615 zero; doing so also neglects the Pedersen and Hall conductivities.

Whereas in Sections 4.1 and 4.2 it was the parallel-polarized component of the dispersion relation that factored out from the other two, the high altitude limit decouples the component polarized out of the x - z plane. The y -polarized ($E_x = E_z = 0$) dispersion relation is simply:

$$\omega^2 = k^2 v_A^2 \quad (4.16)$$

616 Equation (4.16) describes an Alfvén wave with an arbitrary angle of propagation. De-
 617 pending on the angle between the wave vector and the background magnetic field, it
 618 could be guided, compressional, or somewhere in between. Regardless of propagation
 619 angle, the electric field perturbation is perpendicular to both the direction of propaga-
 620 tion and the magnetic field perturbation.

The other two components (from $E_y = 0$) of the high altitude dispersion tensor give an expression quadratic in ω^2 :

$$0 = \omega^4 - (k_x^2 c^2 + k_z^2 v_A^2 + \omega_P^2) \omega^2 + k_z^2 v_A^2 \omega_P^2 \quad (4.17)$$

Which can be solved for

$$\omega^2 = \frac{1}{2} (k_x^2 c^2 + k_z^2 v_A^2 + \omega_P^2) \pm \sqrt{\frac{1}{4} (k_x^2 c^2 + k_z^2 v_A^2 + \omega_P^2)^2 - k_z^2 v_A^2 \omega_P^2} \quad (4.18)$$

Noting again that ω_P is very large, the two roots can be expanded to

$$\omega^2 = k_z^2 v_A^2 \left(\frac{\omega_P^2}{\omega_P^2 + k_x^2 c^2 + k_z^2 v_A^2} \right) + \dots \quad \text{and} \quad \omega^2 = k_x^2 c^2 + k_z^2 v_A^2 + \omega_P^2 + \dots \quad (4.19)$$

621 The first solution of Equation (4.19) is a shear Alfvén wave — in the limit of present
 622 interest, ω_P is large, so the parenthetical quantity is close to unity. The inertial limit,
 623 where frequencies are close to the plasma frequency, is beyond the scope of the present
 624 work. For that same reason, the second solution (which describes an oscillation faster
 625 than the plasma frequency) is not further considered.

626 4.4 Implications to the Present Work

627 The present section's findings carry three implications of particular significance to the
 628 present work.

629 First — with the exception of the plasma oscillation and similar modes, which are
 630 revisited in Chapter 6 — waves propagate at the Alfvén speed. This, in combination
 631 with the grid configuration, constrains the time step that can be used to model them
 632 numerically. The time step must be sufficiently small that information traveling at the
 633 Alfvén speed cannot “skip over” entire grid cells⁶.

Second, the results of the present section allow an estimate of the magnitude of parallel electric field that might be expected from a field line resonance compared to its perpendicular electric field. Between the full dispersion tensor form in Equation (4.5) and the Alfvén wave described by Equation (4.19),

$$\left| \frac{E_z}{E_x} \right| = \frac{k_x k_z c^2}{\omega^2 - k_x^2 c^2 - \omega_P^2} \sim \frac{k^2 c^2}{\omega_P^2} \quad (4.20)$$

634 In essence, the relative magnitudes of the parallel and perpendicular electric fields should
 635 scale quadratically with the ratio of the electron inertial length ($\frac{c}{\omega_P} \sim 1 \text{ km to } 100 \text{ km}$)

⁶As is the convention, the time step is scaled down from the smallest Alfvén zone crossing time by a Courant factor, typically 0.1, meaning that it takes at least ten time steps to cross a grid cell.

and the FLR wavelength ($\frac{1}{k} \sim 10^5$ km). That is, parallel electric fields should be smaller than perpendicular ones by at least six orders of magnitude.

Finally, the dispersion relations shown above indicate how the behavior of a field line resonance should behave as the azimuthal modenumber becomes large.

Whereas the shear Alfvén wave's dispersion relation depends only on the parallel component of the wave vector, the compressional Alfvén wave depends on its magnitude: $\omega^2 = k^2 v_A^2$. If the frequency is smaller than $k v_A$, the wave will become evanescent. The wave vector's magnitude can be no smaller than its smallest component, however, and the azimuthal component scales with the azimuthal modenumber: $k_y \sim \frac{m}{2\pi r}$.

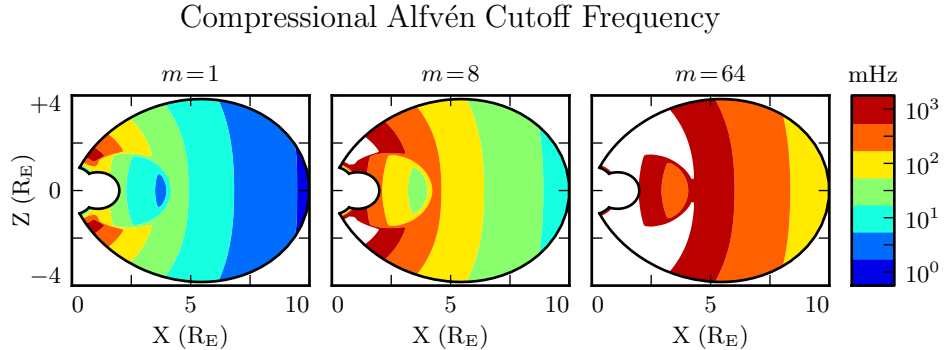


Figure 4.1: Taking $k_y \sim \frac{m}{2\pi r}$ as a lower bound for the magnitude of the wave vector, the above figure demonstrates the lowest frequency at which compressional Alfvén waves may propagate as a function of position and m . Regions shown in white are off the color scale — they have a lower bound on the order of 10^4 mHz or more. The above Alfvén frequency profile is from Kelley[47], for quiet dayside conditions, as discussed in Section 5.2.

This imposes a frequency cutoff on compressional Alfvén waves which scales with the azimuthal modenumber, as shown in Figure 4.1. At small values of m , most of the magnetosphere is conducive to compressional Alfvén waves in the Pc4 frequency range. As m increases, and the wave vector with it, the inner magnetosphere becomes increasingly inaccessible to them.

650 Chapter 5

651 “Tuna Half” Dimensional Model

652 The present section describes the implementation of Tuna, a new two and a half dimensional Alfven wave code based largely on work by Lysak[58, 62].

654 The half-integer dimensionality refers to the fact that Tuna’s spatial grid resolves a
655 two-dimensional slice of the magnetosphere, but that electric and magnetic fields —
656 as well as their curls — are three-dimensional vectors. This apparent contradiction is
657 reconciled by the use of a fixed azimuthal modenumber, m . Electric and magnetic fields
658 are taken to be complex-valued, varying azimuthally per $\exp(im\phi)$; derivatives with
659 respect to ϕ are then replaced by a factor of im .

660 Unlike a fully three-dimensional code, Tuna cannot resolve the evolution of wave structures in the azimuthal direction. Furthermore, the model does not allow coupling between the dayside and nightside magnetospheres. What Tuna does offer is efficiency.
663 The model’s economical geometry allows it to include a realistic Earthward boundary:
664 grid spacing on the order of 10 km, a height-resolved ionospheric conductivity tensor,
665 and even the computation of magnetic field signatures at the ground. Such features
666 would pose a prohibitive computational expense in a large global code.

667 Tuna was developed with field line resonance in mind. As discussed in Chapter 3, such
668 waves extend over just a few hours MLT, minimizing the importance of Tuna’s missing
669 half dimension. Moreover, because field line resonances are known to be affected by both

670 the ionosphere and the plasmasphere, a faithful treatment of the inner magnetosphere
671 is a crucial part of studying them numerically.

672 Perhaps the most exciting feature of Tuna is its novel driving mechanism: ring current
673 perturbation. Codes similar to Tuna have traditionally been driven using compressional
674 pulses at the outer boundary[58, 62, 97, 98]. This has precluded the investigation of
675 waves with large azimuthal modenumber — such as giant pulsations — which are guided,
676 and thus must be driven from within the magnetosphere.

677 Tuna’s source code, written in Fortran, is publicly available at <https://github.com/UMM-Space-Physics>. The repository also includes a pair of Python scripts: a test har-
678 ness — which automates programming environment setup, compilation, and interfacing
679 with the supercomputer queue — and a plotter.
680

681 5.1 Coordinate System

Field line resonance has traditionally been modeled by straightening the field lines
into a rectangular configuration[20, 65], by unrolling the azimuthal coordinate into a
cylindrical coordinate system[76], or through the use of dipole coordinates[75]¹:

$$x \equiv -\frac{\sin^2 \theta}{r} \quad y \equiv \phi \quad z \equiv \frac{\cos \theta}{r^2} \quad (5.1)$$

682 Where r , θ , and ϕ take on their usual spherical meanings of radial distance, colatitude,
683 and azimuthal angle respectively.

684 The dipole coordinate x is constant over each L -shell², y is azimuthal angle, and z is
685 used to index latitude along a given field line. The unit vectors \hat{x} , \hat{y} , and \hat{z} point in
686 the crosswise³ (radially outward at the equator), azimuthal (eastward), and parallel
687 (northward at the equator) directions respectively.

¹The dipole coordinates x , y , and z are sometimes named ν , ϕ , and μ respectively.

²In fact, x is inversely proportional to L .

³In the context of in situ measurements taken near the equatorial plane, \hat{x} is referred to as the radial
direction; however, the present work extends the dipole grid to low altitudes, where \hat{x} is often more
horizontal than vertical. The term “crosswise” is meant to indicate that \hat{x} is defined by the cross
product of \hat{y} and \hat{z} .

Notably, the dipole coordinates in Equation (5.1) are normal to one another. While mathematically convenient, they do not readily accommodate a fixed-altitude boundary at the ionosphere, nor do they allow the dipole magnetic field to intersect the boundary at an oblique angle, as Earth's field does. As a solution, a nonorthogonal set of dipole coordinates was developed by Lysak[58]. Equation (5.2) shows Lysak's coordinates in terms of their contravariant components:

$$u^1 = -\frac{R_I}{r} \sin^2 \theta \quad u^2 = \phi \quad u^3 = \frac{R_I^2}{r^2} \frac{\cos \theta}{\cos \theta_0} \quad (5.2)$$

688 Above, R_I is the position of the ionosphere relative to Earth's center; it's typically taken
689 to be $1 R_E + 100 \text{ km}$.

690 Like the dipole coordinates x , y , and z , Lysak's coordinates u^1 , u^2 , and u^3 correspond to
691 L -shell, azimuthal angle, and position along a field line respectively. However, compared
692 to z , u^3 has been renormalized using the invariant colatitude⁴ θ_0 . As a result, u^3 takes
693 the value $+1$ at the northern ionospheric boundary and -1 at the southern ionospheric
694 boundary for all field lines.

Because Lysak's coordinate system is not orthogonal — that is, because curves of constant u^1 and curves of constant u^3 can intersect at non-right angles — it's necessary to consider covariant and contravariant basis vectors separately.

$$\hat{e}_i \equiv \frac{\partial}{\partial u^i} \underline{x} \quad \hat{e}^i \equiv \frac{\partial}{\partial \underline{x}} u^i \quad (5.3)$$

Covariant basis vectors \hat{e}_i are normal to the curve defined by constant u^i , while contravariant basis vectors \hat{e}^i are tangent to the coordinate curve (equivalently, \hat{e}^i is normal to the plane defined by constant u^j for all $j \neq i$). These vectors are reciprocal to one another, and can be combined to give components of the metric tensor $\underline{\underline{g}}$ [19].

$$\hat{e}^i \cdot \hat{e}_j = \delta_j^i \quad g_{ij} \equiv \hat{e}_i \cdot \hat{e}_j \quad g^{ij} \equiv \hat{e}^i \cdot \hat{e}^j \quad (5.4)$$

⁴The invariant colatitude is the colatitude θ at which a field line intersects the ionosphere. It is related to the McIlwain parameter by $\cos \theta_0 \equiv \sqrt{1 - \frac{R_I}{L}}$.

695 The symbol δ_j^i is the Kronecker delta; the present work also makes use of the Levi-Civita
 696 symbol ε^{ijk} and Einstein's convention of implied summation over repeated indeces[22].

The metric tensor allows rotation between covariant and contravariant representations of vectors.

$$A_i = g_{ij} A^j \quad \text{and} \quad A^i = g^{ij} A_j \quad \text{where} \quad A_i \equiv \underline{A} \cdot \hat{e}_i \quad \text{and} \quad A^i \equiv \underline{A} \cdot \hat{e}^i \quad (5.5)$$

In addition, the determinant of the metric tensor is used to define cross products and curls⁵.

$$(\underline{A} \times \underline{B})^i = \frac{\varepsilon^{ijk}}{\sqrt{g}} A_j B_k \quad \text{and} \quad (\nabla \times \underline{A})^i = \frac{\varepsilon^{ijk}}{\sqrt{g}} \frac{\partial}{\partial u^j} A_k \quad \text{where} \quad g \equiv \det \underline{g} \quad (5.6)$$

Explicit forms of the basis vectors and metric tensor can be found in the appendix of Lysak's 2004 paper[58]. At present, it's sufficient to note the mapping between Lysak's basis vectors and the usual dipole unit vectors.

$$\hat{x} = \frac{1}{\sqrt{g^{11}}} \hat{e}^1 \quad \hat{y} = \frac{1}{\sqrt{g^{22}}} \hat{e}^2 \quad \hat{z} = \frac{1}{\sqrt{g^{33}}} \hat{e}^3 \quad (5.7)$$

The basis vectors can also be mapped to the spherical unit vectors, though Equation (5.8) is valid only at the ionospheric boundary.

$$\hat{\theta} = \frac{1}{\sqrt{g_{11}}} \hat{e}_1 \quad \hat{\phi} = \frac{1}{\sqrt{g_{22}}} \hat{e}_2 \quad \hat{r} = \frac{1}{\sqrt{g_{33}}} \hat{e}_3 \quad (5.8)$$

697 The coordinates converge at the equatorial ionosphere, so an inner boundary is necessary
 698 to maintain finite grid spacing. It's typically placed at $L = 2$. The outer boundary is
 699 at $L = 10$. The dipole approximation of Earth's magnetic field is tenuous at the outer
 700 boundary; however, in practice, wave activity is localized inside $L \sim 7$. The grid is
 701 spaced uniformly in u^1 , which gives finer resolution close to Earth and coarser resolution
 702 at large distances.

⁵The square root of the determinant of the metric tensor is called the Jacobian. It's sometimes denoted using the letter J , which is reserved for current in the present work.

703 Spacing in u^3 is set by placing grid points along the outermost field line. The points are
704 closest together at the ionosphere, and grow towards the equator. The spacing increases
705 in a geometric fashion, typically by 3 %.

706 Typically, Tuna uses a grid 150 points in u^1 by 350 points in u^3 . The result is a resolution
707 on the order of 10 km at the ionosphere, which increases to the order of 10^3 km at the
708 midpoint of the outermost field line.

709 There are no grid points in u^2 due to the two-and-a-half-dimensional nature of the
710 model. Fields are assumed to vary as $\exp(imu^2)$ — equally, $\exp(im\phi)$ — so derivatives
711 with respect to u^2 are equivalent to a factor of im . In effect, the real component of
712 each field is azimuthally in phase with the (purely real) driving, while imaginary values
713 represent behavior that is azimuthally offset. Azimuthal modenumbers span the range
714 $1 \lesssim m \lesssim 100$, consistent with observations of Pc4 and Pg events[16, 17, 69, 88].

715 The simulation’s time step is set based on the grid spacing. As is the convention, δt is
716 set to match the smallest Alfvén zone crossing time, scaled down by a Courant factor
717 (typically 0.1). It bears noting that the smallest crossing time need not correspond to
718 the smallest zone; the Alfvén speed peaks several thousand kilometers above Earth’s
719 surface, in the ionospheric Alfvén resonator[62]. A typical time step is on the order of
720 10^{-5} s.

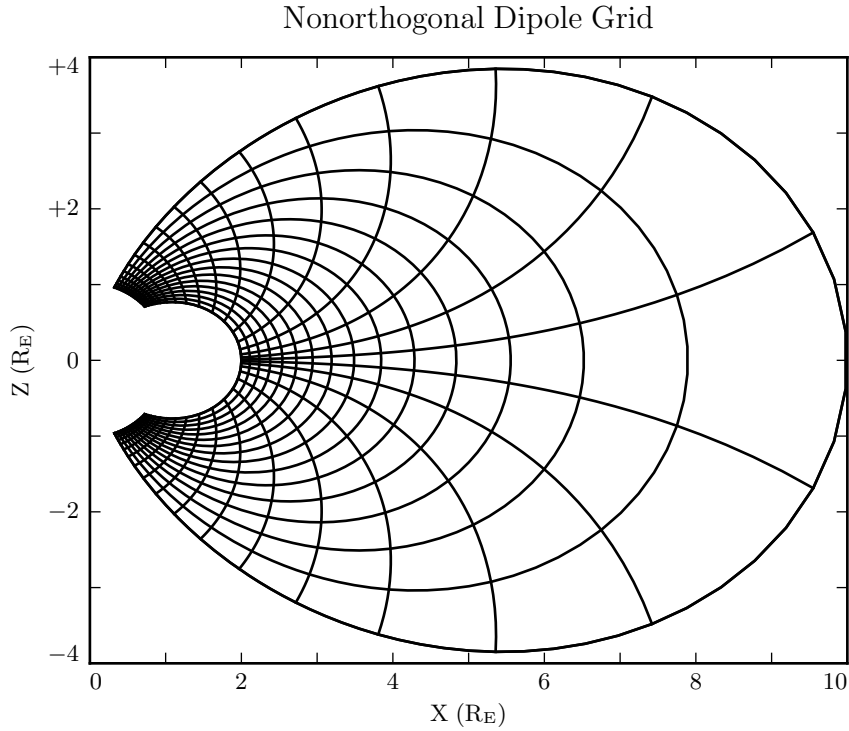


Figure 5.1: The model’s nonorthogonal dipole grid. Every fifth point is shown in each direction. The high concentration of grid points near Earth’s equator is a consequence of the coordinate system, which converges at the equatorial ionosphere. Earth (not shown) is centered at the origin with unit radius.

721 5.2 Physical Parameter Profiles

Tuna models Earth’s magnetic field to be an ideal dipole, so the zeroth-order field strength is written in the usual form:

$$\underline{B}_0 = 3.1 \times 10^4 \text{ nT} \left(\frac{R_E}{r} \right)^3 \left(2 \cos \theta \hat{r} - \sin \theta \hat{\theta} \right) \quad (5.9)$$

Number density is taken to be the sum of an inverse-radial-dependent auroral profile and a plasmaspheric profile dependent on the L -shell[62]:

$$n = n_{AZ} \frac{r_{AZ}}{r} + n_{PS} \exp\left(\frac{-L}{L_{PS}}\right) \left(\frac{1}{2} - \frac{1}{2} \tanh \frac{L - L_{PP}}{\delta L_{PP}} \right) \quad (5.10)$$

722 Where typical values are shown in Table 5.1.

Table 5.1: Typical Parameters for the Tuna Density Profile

Variable	Value	Description
L_{PS}	1.1	Scale L of the plasmasphere.
L_{PP}	4.0	Location of the plasmapause.
δL_{PP}	0.1	Thickness of the plasmapause.
n_{AZ}	$10 / \text{cm}^3$	Number density at the base of the auroral zone.
n_{PS}	$10^4 / \text{cm}^3$	Number density at the base of the plasmasphere.
r_{AZ}	1 R_E	Scale height of the auroral density distribution.

The perpendicular component of the electric tensor, ϵ_{\perp} , is computed based on Kelley's[47] tabulated ionospheric values, ϵ_K , which are adjusted to take into account the density profile in Equation (5.10).

$$\epsilon_{\perp} = \epsilon_K + \frac{Mn}{B_0^2} \quad (5.11)$$

723 Where M is the mean molecular mass, which is large ($\sim 28 \text{ u}$) at 100 km altitude, then
724 drops quickly (down to 1 u by $\sim 1000 \text{ km}$)[62].

725 The Alfvén speed profile is computed from the perpendicular electric constant in the
726 usual way, $v_A^2 \equiv \frac{1}{\mu_0 \epsilon_{\perp}}$. This form takes into account the effect of the displacement
727 current, which becomes important in regions where the Alfvén speed approaches the
728 speed of light.

729 While the density profile is held constant for all runs discussed in the present work,
730 the Alfvén speed profile is not. Four different profiles are used for the low-density

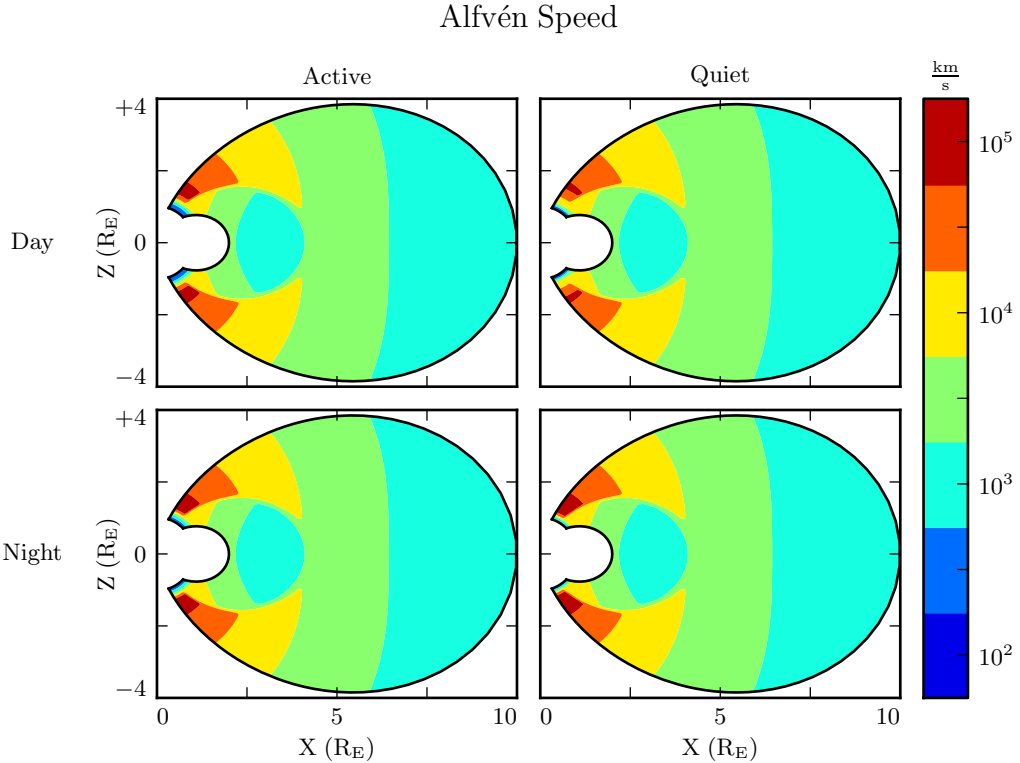


Figure 5.2: Alfvén speed profiles are based on low-density values tabulated by Kelley[47]. They are adjusted to take into account the density of the plasmapause and mass loading near the Earthward boundary.

731 perpendicular electric constant ϵ_K , corresponding to the differing ionospheric conditions
 732 between the dayside and the nightside, and between the high and low points in the
 733 solar cycle. These differences are visible in Figure 5.2, particularly in the size of the
 734 ionospheric Alfvén resonator (the peak in Alfvén speed in the high-latitude ionosphere).

735 Ionospheric conductivity profiles are also based on values tabulated by Kelley, adjusted
 736 by Lysak[62] to take into account the abundance of heavy ions near the Earthward
 737 boundary. Pedersen, Hall, and parallel conductivities are each resolved by altitude, as
 738 shown in Figure 5.3.

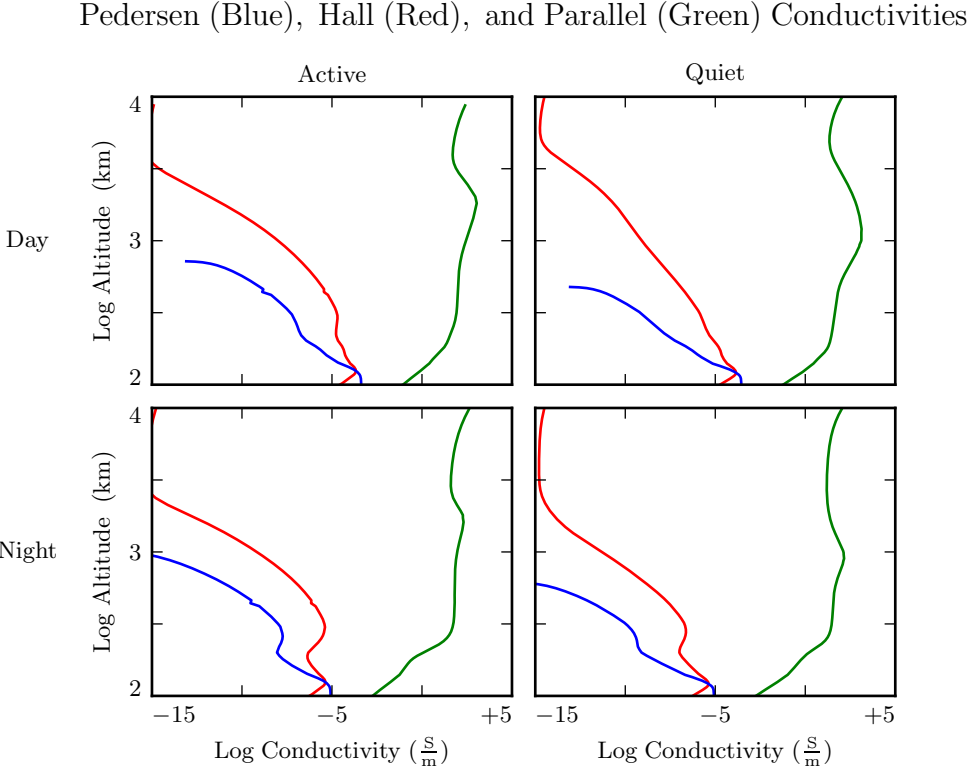


Figure 5.3: Ionospheric conductivity profiles are adapted by Lysak[62] from Kelley's tabulated values[47], in order to take into account the effects of heavy ions at low altitudes. These profiles allow Tuna to simulate magnetosphere-ionosphere coupling under a variety of conditions.

739 Tuna's physical parameter profiles are static over the course of each run. Even so-called
 740 ultra low frequency waves like Pc4 pulsations are fast compared to convective timescales
 741 in the magnetosphere.

742 5.3 Driving

743 Models similar to Tuna have traditionally been driven using compression at the outer
 744 boundary[58, 62, 97, 98]. Such driving acts as a proxy for solar wind compression,
 745 Kelvin-Helmholtz effects at the magnetopause, and so on. However, because of the

746 guided nature of high-modenumber Alfvén waves, simulations driven from the outer
747 boundary are constrained to the consideration of waves with low azimuthal modenumber
748 (equivalently, large azimuthal wavelength).

749 This issue is demonstrated in Figure 5.4. At low modenumber, energy delivered at
750 the outer boundary propagates across field lines in order to stimulate resonances in
751 the inner magnetosphere. However, as modenumber increases, Alfvén waves become
752 increasingly guided, and the inner magnetosphere is unaffected by perturbations at the
753 outer boundary.

754 In order to simulate high-modenumber Alfvén waves in the inner magnetosphere — such
755 as giant pulsations — a new driving mechanism is necessary. Perturbation of the ring
756 current is a natural choice, as Alfvén waves in the Pc4 range are known to interact with
757 ring current particles through drift and drift-bounce resonances. The ring current is a
758 dynamic region, particularly during and after geomagnetic storms and substorms; it's
759 easy to imagine the formation of localized inhomogeneities.

760 In order to estimate an appropriate magnitude for perturbations of the ring current, the
761 Sym-H storm index⁶ is used. The index is measured once per minute, and so cannot
762 directly detect ring current modulations in the Pc4 frequency range. Instead, the index
763 is transformed into the frequency domain, allowing a fit of its pink noise⁷.

764 As shown in Figure 5.5, a Fourier transform of the Sym-H index (taken here from the
765 June 2013 storm) suggests that magnetic field perturbations at Earth's surface due to
766 ring current activity in the Pc4 frequency range could be up to the order of 10^{-2} nT.
767 Supposing that the ring current is centered around $5 R_E$ geocentric, that corresponds to
768 a current on the order of 0.1 MA. Tuna's driving is spread using a Gaussian profile in
769 u^1 (typically centered at $L = 5$) and u^3 (typically centered just off the equator), with a
770 characteristic area of $1 R_E^2$; this gives a current density on the order of $10^{-4} \mu\text{A}/\text{m}^2$.

771 Admittedly, Sym-H is an imperfect tool for estimating the magnitude of localized per-
772 turbations to the ring current, particularly those with high modenumber. As a global

⁶Sym-H is analogous to Dst, and the two match each other closely[96]. The crucial difference in this case is that Sym-H is recorded at a higher frequency.

⁷Pink noise, also called $\frac{1}{f}$ noise, refers to the power law decay present in the Fourier transforms of all manner of physical signals.

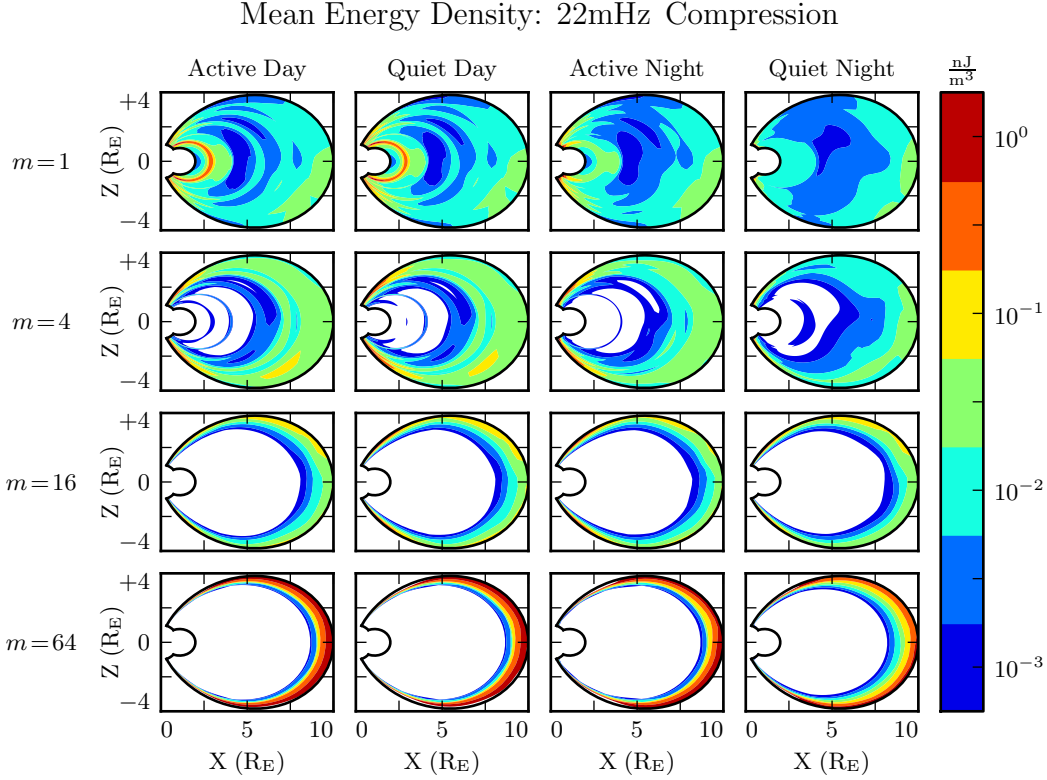


Figure 5.4: Each cell presents the mean energy density over the course of a 300s run, as a function of position, due to compressional driving at the outer boundary. Azimuthal modenumber varies by row, and ionospheric conditions vary by column. For runs with small azimuthal modenumber, it's clear that energy is able to propagate across field lines and stimulate wave activity in the inner magnetosphere. When the modenumber is large, energy is unable to penetrate to the inner magnetosphere. Notably, the large values on the bottom row should be taken with a grain of salt; it's not clear that the model's results are reliable when waves are continuously forced against the boundary.

- 773 index, its values are effectively averaged around Earth. Unlike in situ measurements,
 774 however, this method has the advantage of estimating total driving current (and thus
 775 total energy input).
- 776 In the results shown in Chapters 6 and 7, the driving current is sinusoidal, and delivered
 777 purely in the azimuthal direction (representing a perturbation to the magnitude of the

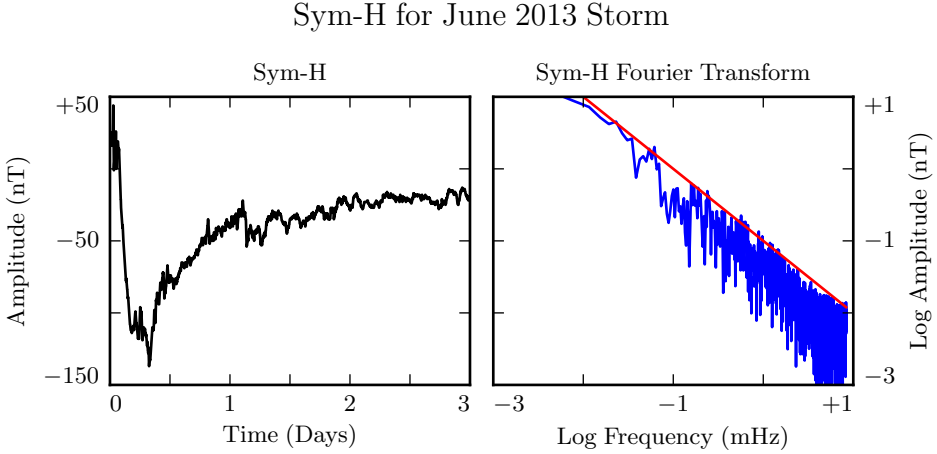


Figure 5.5: The Sym-H storm index[70] measures magnetic perturbations on Earth’s surface due to ring current activity. The amplitude of oscillations in the Pc4 range is estimated by fitting the pink noise in its Fourier transform.

ring current, but not to its direction). Tuna also allows several other driving waveforms, and the direction of the current could be modified with trivial modifications to the code.

5.4 Maxwell’s Equations

Tuna simulates the evolution of electromagnetic waves in accordance with Ampère’s law and Faraday’s law. Computation is carried out on a Yee grid[102]: electric fields and magnetic fields are offset by half a time step, and each field component is defined on either odd or even grid points in each dimension to ensure that curls are computed using centered differences.

The Ohmic current in Ampère’s law is replaced with $\underline{\sigma} \cdot \underline{E}$ per Kirchhoff’s formulation of Ohm’s law. Then, taking \underline{J} to represent the driving current discussed in Section 5.3, Maxwell’s equations are written

$$\frac{\partial}{\partial t} \underline{B} = -\nabla \times \underline{E} \quad \underline{\epsilon} \cdot \frac{\partial}{\partial t} \underline{E} = \frac{1}{\mu_0} \nabla \times \underline{B} - \underline{J} - \underline{\sigma} \cdot \underline{E} \quad (5.12)$$

It is convenient to introduce shorthand for the curl of each field: $\underline{C} \equiv \nabla \times \underline{E}$ and $\underline{F} \equiv \nabla \times \underline{B} - \mu_0 \underline{J}$. Or, recalling Equation (5.6),

$$C^i = \frac{\varepsilon^{ijk}}{\sqrt{g}} \frac{\partial}{\partial u^j} E_k \quad F^i = \frac{\varepsilon^{ijk}}{\sqrt{g}} \frac{\partial}{\partial u^j} B_k - J^i \quad (5.13)$$

In these terms, Faraday's law can simply be written:

$$\frac{\partial}{\partial t} B^i = -C^i \quad (5.14)$$

Writing each component out explicitly, and using the metric tensor (per Equation (5.5)) to eliminate contravariant magnetic field components⁸, Equation (5.14) becomes:

$$\begin{aligned} B_1 &\leftarrow B_1 - g_{11} \delta t C^1 - g_{13} \delta t C^3 \\ B_2 &\leftarrow B_2 - g_{22} \delta t C^2 \\ B_3 &\leftarrow B_3 - g_{31} \delta t C^1 - g_{33} \delta t C^3 \end{aligned} \quad (5.15)$$

⁷⁸⁶ Note that the \leftarrow operator is used in Equation (5.15) to indicate assignment, rather than
⁷⁸⁷ equality. Terms on the left are new, while those on the right are old.

Unlike Faraday's law, Ampère's law cannot be trivially solved. Not only does the time derivative of \underline{E} depend on its own future value, but the crosswise and azimuthal components of the equation are coupled by the Hall terms in the conductivity tensor. Fortunately, the electric tensor can be inverted, allowing a solution by integrating factors:

$$\underline{\underline{\epsilon}} \cdot \frac{\partial}{\partial t} \underline{E} = \frac{1}{\mu_0} \underline{F} - \underline{\underline{\sigma}} \cdot \underline{E} \quad \text{becomes} \quad \left(\underline{\underline{\Omega}} + \underline{\underline{\epsilon}} \frac{\partial}{\partial t} \right) \cdot \underline{E} = \underline{\underline{V}}^2 \cdot \underline{F} \quad (5.16)$$

⁸Fields are stored only in terms of their covariant components, and curls in terms of their contravariant components. This reduces Tuna's memory footprint (since each field need not be stored twice) as well as its computational cost (since time need not be spent rotating between bases). As a result, Tuna's solutions to Maxwell's equations are linear expressions whose coefficients are a mishmash of physical constants and geometric factors. To save time, each coefficient is computed once and stored, rather than being multiplied out from scratch with each time step.

Where $\underline{\underline{\mathbb{I}}}$ is the identity tensor and in x - y - z coordinates⁹,

$$\underline{\underline{V}^2} \equiv \frac{1}{\mu_0} \underline{\underline{\epsilon}}^{-1} = \begin{bmatrix} v_A^2 & 0 & 0 \\ 0 & v_A^2 & 0 \\ 0 & 0 & c^2 \end{bmatrix} \quad \text{and} \quad \underline{\underline{\Omega}} \equiv \underline{\underline{\epsilon}}^{-1} \cdot \underline{\underline{\sigma}} = \begin{bmatrix} \frac{\sigma_P}{\epsilon_{\perp}} & \frac{-\sigma_H}{\epsilon_{\perp}} & 0 \\ \frac{\sigma_H}{\epsilon_{\perp}} & \frac{\sigma_P}{\epsilon_{\perp}} & 0 \\ 0 & 0 & \frac{\sigma_0}{\epsilon_0} \end{bmatrix} \quad (5.17)$$

Multiplying through by $\exp(\underline{\underline{\Omega}} t)$ and applying the product rule, Equation (5.16) becomes¹⁰

$$\frac{\partial}{\partial t} \left(\exp(\underline{\underline{\Omega}} t) \cdot \underline{\underline{E}} \right) = \exp(\underline{\underline{\Omega}} t) \cdot \underline{\underline{V}^2} \cdot \underline{\underline{F}} \quad (5.18)$$

Equation (5.18) can then be integrated over a small time step δt and expressed in terms of the assignment operator introduced in Equation (5.15).

$$\underline{\underline{E}} \leftarrow \exp(-\underline{\underline{\Omega}} \delta t) \cdot \underline{\underline{E}} + \delta t \exp(-\underline{\underline{\Omega}} \frac{\delta t}{2}) \cdot \underline{\underline{V}^2} \cdot \underline{\underline{F}} \quad (5.19)$$

The tensor exponential is evaluated by splitting $\underline{\underline{\Omega}}$ into the sum of its diagonal and Hall components¹¹. The Hall exponential condenses into sines and cosines, giving a rotation around the magnetic field line:

$$\underline{\underline{E}} \leftarrow \exp(-\underline{\underline{\Omega}}' \delta t) \cdot \underline{\underline{R}}_z \left(\frac{-\sigma_H \delta t}{\epsilon_{\perp}} \right) \cdot \underline{\underline{E}} + \delta t \exp(-\underline{\underline{\Omega}}' \frac{\delta t}{2}) \cdot \underline{\underline{R}}_z \left(\frac{-\sigma_H \delta t}{2\epsilon_{\perp}} \right) \cdot \underline{\underline{V}^2} \cdot \underline{\underline{F}} \quad (5.20)$$

Where

$$\underline{\underline{R}}_z(\theta) = \begin{bmatrix} \cos \theta & -\sin \theta & 0 \\ \sin \theta & \cos \theta & 0 \\ 0 & 0 & 1 \end{bmatrix} \quad \text{and} \quad \underline{\underline{\Omega}}' \equiv \begin{bmatrix} \frac{\sigma_P}{\epsilon_{\perp}} & 0 & 0 \\ 0 & \frac{\sigma_P}{\epsilon_{\perp}} & 0 \\ 0 & 0 & \frac{\sigma_0}{\epsilon_0} \end{bmatrix} \quad (5.21)$$

⁹Note the parallel component of the present definition of $\underline{\underline{\Omega}}$ differs slightly from that used in Chapter 4, due to the present chapter's neglect of inertial effects; see Chapter 6.

¹⁰Tensor exponentiation is analogous to scalar exponentiation[37]: $\exp(\underline{\underline{T}}) \equiv \sum_n \frac{1}{n!} \underline{\underline{T}}^n$.

¹¹For tensors, $\exp(\underline{\underline{S}} + \underline{\underline{T}}) = \exp(\underline{\underline{S}}) \exp(\underline{\underline{T}})$ as long as $\underline{\underline{S}} \cdot \underline{\underline{T}} = \underline{\underline{T}} \cdot \underline{\underline{S}}$.

The parallel component of term of Equation (5.20) is simply

$$E_z \leftarrow E_z \exp\left(\frac{-\sigma_0 \delta t}{\epsilon_0}\right) + c^2 \delta t F_z \exp\left(\frac{-\sigma_0 \delta t}{2\epsilon_0}\right) \quad (5.22)$$

Or, using Equation (5.7) to map to the covariant basis,

$$E_3 \leftarrow E_3 \exp\left(\frac{-\sigma_0 \delta t}{\epsilon_0}\right) + c^2 \delta t (g_{31} F^1 + g_{33} F^3) \exp\left(\frac{-\sigma_0 \delta t}{2\epsilon_0}\right) \quad (5.23)$$

788 Tuna's conductivity profile gives a minimum value of $\frac{\sigma_0 \delta t}{\epsilon_0}$ on the order of 10^3 , making
 789 $\exp\left(\frac{-\sigma_0 \delta t}{\epsilon_0}\right)$ far too small to be stored in a double precision variable¹². That is, this
 790 model takes E_3 (and, proportionally, E_z) to be uniformly zero. This issue is revisited
 791 in Chapter 6.

The perpendicular components of Equation (5.20) give the expressions:

$$\begin{aligned} E_1 + \frac{g^{13}}{g^{11}} E_3 &\leftarrow E_1 \cos\left(\frac{-\sigma_H \delta t}{\epsilon_\perp}\right) \exp\left(\frac{-\sigma_P \delta t}{\epsilon_\perp}\right) \\ &+ E_2 \sin\left(\frac{-\sigma_H \delta t}{\epsilon_\perp}\right) \exp\left(\frac{-\sigma_P \delta t}{\epsilon_\perp}\right) \sqrt{\frac{g^{22}}{g^{11}}} \\ &+ E_3 \cos\left(\frac{-\sigma_H \delta t}{\epsilon_\perp}\right) \exp\left(\frac{-\sigma_P \delta t}{\epsilon_\perp}\right) \frac{g^{13}}{g^{11}} \\ &+ F^1 \cos\left(\frac{-\sigma_H \delta t}{2\epsilon_\perp}\right) \exp\left(\frac{-\sigma_P \delta t}{2\epsilon_\perp}\right) \frac{v_A^2 \delta t}{g^{11}} \\ &+ F^2 \sin\left(\frac{-\sigma_H \delta t}{2\epsilon_\perp}\right) \exp\left(\frac{-\sigma_P \delta t}{2\epsilon_\perp}\right) \frac{v_A^2 \delta t}{\sqrt{g^{11} g^{22}}} \end{aligned} \quad (5.24)$$

¹²Not coincidentally, $\frac{\sigma_0}{\epsilon_0}$ can also be written $\frac{\omega_P^2}{\nu}$. At the ionosphere, the collision frequency ν is fast compared to field line resonance timescales, but it's still slow compared to the plasma frequency.

and

$$\begin{aligned}
E_2 \leftarrow & -E_1 \sin\left(\frac{-\sigma_H \delta t}{\epsilon_{\perp}}\right) \exp\left(\frac{-\sigma_P \delta t}{\epsilon_{\perp}}\right) \sqrt{\frac{g^{11}}{g^{22}}} \\
& + E_2 \cos\left(\frac{-\sigma_H \delta t}{\epsilon_{\perp}}\right) \exp\left(\frac{-\sigma_P \delta t}{\epsilon_{\perp}}\right) \\
& - E_3 \sin\left(\frac{-\sigma_H \delta t}{\epsilon_{\perp}}\right) \exp\left(\frac{-\sigma_P \delta t}{\epsilon_{\perp}}\right) \frac{g^{13}}{\sqrt{g^{11} g^{22}}} \\
& - F^1 \sin\left(\frac{-\sigma_H \delta t}{2\epsilon_{\perp}}\right) \exp\left(\frac{-\sigma_P \delta t}{2\epsilon_{\perp}}\right) \frac{v_A^2 \delta t}{\sqrt{g^{11} g^{22}}} \\
& + F^2 \cos\left(\frac{-\sigma_H \delta t}{2\epsilon_{\perp}}\right) \exp\left(\frac{-\sigma_P \delta t}{2\epsilon_{\perp}}\right) \frac{v_A^2 \delta t}{g^{22}}
\end{aligned} \tag{5.25}$$

792 The E_3 terms in Equations (5.24) and (5.25) can be ignored at present. They are
793 revisited in Chapter 6.

794 It bears recalling that the driving current is defined as part of \underline{F} , per Equation (5.13).
795 When the driving current is purely azimuthal ($J^1 = J^3 = 0$), the driving is in principle
796 applied to both the poloidal and the toroidal electric fields through F^2 . However,
797 in practice, the driving applied to the toroidal electric field is vanishingly small. The
798 driving current J^2 is localized around $5 R_E$ geocentric, and $\exp\left(\frac{-\sigma_P \delta t}{2\epsilon_{\perp}}\right)$ drops off quickly
799 with altitude.

800 5.5 Boundary Conditions

801 Dirichlet and Neumann boundary conditions are applied to the electric field components
802 and magnetic field components respectively. That is, electric fields are zero at the inner
803 and outer boundaries, and magnetic fields normal to the inner and outer boundaries are
804 zero.

805 These boundary conditions can in principle cause nonphysical reflections at the bound-
806 ary¹³. In practice, however (with a noted exception in Chapter 7), wave activity is
807 concentrated well within the simulation domain. Simulation results are robust under

¹³See, for example, the bottom row of Figure 5.4.

808 an exchange of Dirichlet and Neumann boundary conditions, though a self-inconsistent
 809 set of boundary conditions (such as applying Neumann conditions to B_1 but Dirichlet
 810 conditions to B_3) quickly causes instability.

811 The Earthward boundary conditions are as follows.

Between the top of the neutral atmosphere and the bottom of the ionosphere, the model includes a thin, horizontal current sheet representing the ionosphere's E layer[58]. By integrating Ampère's law over the layer, it can be shown[27] that the horizontal electric field values at the edge of the grid are determined by the jump in the horizontal magnetic fields:

$$\underline{\underline{\Sigma}} \cdot \underline{E} = \frac{1}{\mu_0} \lim_{\delta r \rightarrow 0} \left[\hat{r} \times \underline{B} \right]_{R_I - \delta r}^{R_I + \delta r} \quad (5.26)$$

The integrated conductivity tensor $\underline{\underline{\Sigma}}$ is written in θ - ϕ coordinates as[58]:

$$\underline{\underline{\Sigma}} \equiv \begin{bmatrix} \frac{\Sigma_0 \Sigma_P}{\Sigma_0 \cos^2 \alpha + \Sigma_P \sin^2 \alpha} & \frac{-\Sigma_0 \Sigma_H}{\Sigma_0 \cos^2 \alpha + \Sigma_P \sin^2 \alpha} \\ \frac{\Sigma_0 \Sigma_H}{\Sigma_0 \cos^2 \alpha + \Sigma_P \sin^2 \alpha} & \Sigma_P + \frac{\Sigma_H^2 \sin^2 \alpha}{\Sigma_0 \cos^2 \alpha + \Sigma_P \sin^2 \alpha} \end{bmatrix} \quad (5.27)$$

812 Where α is the angle between the magnetic field and the vertical direction, given by
 813 $\cos \alpha \equiv \frac{-2 \cos \theta}{\sqrt{1+3 \cos^2 \theta}}$, and Σ_P , Σ_H , and Σ_0 are the height-integrated Pedersen, Hall,
 814 and parallel conductivities respectively. Their values are determined by integrating
 815 Kelley's[47] conductivity profiles from Earth's surface to the ionospheric boundary; val-
 816 ues are shown in Table 5.2.

Table 5.2: Integrated Atmospheric Conductivity (S)

	Σ_0	Σ_P	Σ_H
Active Day	424	0.65	6.03
Quiet Day	284	0.44	4.02
Active Night	9	0.01	0.12
Quiet Night	9	0.01	0.12

817 The atmospheric conductivities of the two nightside profiles are the same, though the
818 profiles differ significantly at higher altitudes, as shown in Section 5.2.

An expression for the horizontal electric fields at the boundary is obtained by inverting Equation (5.26). After mapping to covariant coordinates per Equation (5.8), and taking $\Sigma \equiv \det \underline{\underline{\Sigma}}$,

$$\begin{aligned} E_1 &\leftarrow \frac{1}{\mu_0 \Sigma} \lim_{\delta r \rightarrow 0} \left[-\Sigma_{\theta\phi} B_1 - \sqrt{\frac{g_{11}}{g_{22}}} \Sigma_{\phi\phi} B_2 \right]_{R_I-\delta r}^{R_I+\delta r} \\ E_2 &\leftarrow \frac{1}{\mu_0 \Sigma} \lim_{\delta r \rightarrow 0} \left[\sqrt{\frac{g_{22}}{g_{11}}} \Sigma_{\theta\theta} B_1 + \Sigma_{\phi\theta} B_2 \right]_{R_I-\delta r}^{R_I+\delta r} \end{aligned} \quad (5.28)$$

819 The atmospheric field is computed in terms of a scalar magnetic potential, Ψ , such
820 that $\underline{B} = \nabla \Psi$. The neutral atmosphere is considered to be a perfect insulator, giving
821 $\nabla \times \underline{B} = 0$. Combined with $\nabla \cdot \underline{B} = 0$ (per Maxwell's equations), this ensures that Ψ
822 satisfies Laplace's equation, $\nabla^2 \Psi = 0$, and thus can be written as a sum of harmonics.

Laplace's equation can be solved analytically; however, a numerical solution is preferable to ensure orthonormality on a discrete and incomplete¹⁴ grid. After separating out the radial and azimuthal dependence in the usual way, the latitudinal component of Laplace's equation is written in terms of $s \equiv -\sin^2 \theta$:

$$(4s^2 + 4s) \frac{d^2}{ds^2} Y_\ell + (4 + 6s) \frac{d}{ds} Y_\ell - \frac{m^2}{s} Y_\ell = \ell (\ell + 1) Y_\ell \quad (5.29)$$

Using centered differences to linearize the derivatives, Equation (5.29) becomes a system of coupled linear equations, one per field line. It is then solved numerically for eigenvalues $\ell (\ell + 1)$ and eigenfunctions Y_ℓ ¹⁵. In terms of the harmonics Y_ℓ , the magnetic potential between the Earth's surface and the top of the atmosphere is written using

¹⁴As discussed in Section 5.1, the grid is constrained to finite L , which excludes the equator as well as the poles.

¹⁵Solving Laplace's equation analytically results in spherical harmonics indexed by both ℓ and m , the separation constants for θ and ϕ respectively. In two and a half dimensions, ϕ is not explicitly resolved, so m is set manually.

coefficients a_ℓ and b_ℓ :

$$\Psi = \sum_\ell \left(a_\ell r^\ell + b_\ell r^{-\ell-1} \right) Y_\ell \quad (5.30)$$

As a boundary condition for Ψ , Earth is assumed to be a perfect conductor. This forces the magnetic field at Earth's surface to be horizontal; that is, $B_r = \frac{\partial}{\partial r} \Psi = 0$. Noting that solutions to Laplace's equation are orthonormal, each element of the sum in Equation (5.30) must be independently zero at R_E . This allows the coefficients a_ℓ and b_ℓ to be expressed in terms of one another.

$$b_\ell = \frac{\ell}{\ell+1} R_E^{2\ell+1} a_\ell \quad (5.31)$$

The current sheet at the top of the atmosphere is assumed to be horizontal, so the radial component of the magnetic field must be the same just above and just below it. Taking the radial derivative of Equation (5.30) at the top of the atmosphere, and eliminating b_ℓ with Equation (5.31), gives

$$B_r = \sum_\ell \ell a_\ell R_I^{\ell-1} \left(1 - \lambda^{2\ell+1} \right) Y_\ell \quad \text{where} \quad \lambda \equiv \frac{R_E}{R_I} \sim 0.975 \quad (5.32)$$

The summation is collapsed by “integrating” over a harmonic¹⁶. Inverse harmonics are obtained by inverting the eigenvector matrix. Then $Y_\ell \cdot Y_{\ell'}^{-1} = \delta_{\ell\ell'}$ by construction.

$$a_\ell = \frac{1}{\ell R_I^{\ell-1}} \frac{B_r \cdot Y_\ell^{-1}}{1 - \lambda^{2\ell+1}} \quad (5.33)$$

Combining Equations (5.30), (5.31), and (5.33) allows the expression of Ψ at the top and bottom of the atmosphere as a linear combination of radial magnetic field components

¹⁶Because the functions are defined on a discrete grid, their inner product is not an integral, but a sum: $B_r \cdot Y_\ell^{-1} \equiv \sum_i B_r[i] Y_\ell^{-1}[i]$.

at the bottom of the ionosphere.

$$\begin{aligned}\Psi_E &= \sum_{\ell} Y_{\ell} \frac{R_I}{\ell (\ell - 1)} \frac{(2\ell - 1) \lambda^{\ell}}{1 - \lambda^{2\ell+1}} B_r \cdot Y_{\ell}^{-1} \\ \Psi_I &= \sum_{\ell} Y_{\ell} \frac{R_I}{\ell (\ell - 1)} \frac{(\ell - 1) + \ell \lambda^{2\ell+1}}{1 - \lambda^{2\ell+1}} B_r \cdot Y_{\ell}^{-1}\end{aligned}\tag{5.34}$$

Horizontal magnetic fields are obtained by taking derivatives of Ψ .

$$B_1 = \frac{\partial}{\partial u^1} \Psi \quad B_2 = \frac{\partial}{\partial u^2} \Psi\tag{5.35}$$

- 823 Horizontal magnetic field values at the top of the atmosphere are used to impose bound-
- 824 ary conditions on the electric fields at the bottom of the ionosphere, per Equation (5.28).
- 825 Those at Earth's surface are valuable because they allow a direct comparison between
- 826 model output and ground magnetometer data, after being mapped to physical coordi-
- 827 nates per Equation (5.8).

828 **Chapter 6**

829 **Electron Inertial Effects**

830 As laid out in Chapter 5, Tuna resolves neither currents nor electric fields parallel to
831 the background magnetic field. This is unfortunate; parallel electric fields generated by
832 kinetic and inertial Alfvén waves (including fundamental field line resonances[77, 93])
833 are a topic of particular interest in the study of auroral particle precipitation.

Parallel currents and electric fields can be added to Tuna through the consideration of electron inertial effects in Ohm's law:

$$0 = \sigma_0 E_z - J_z \quad \text{becomes} \quad \frac{1}{\nu} \frac{\partial}{\partial t} J_z = \sigma_0 E_z - J_z \quad (6.1)$$

With the addition of the electron inertial term, it is necessary to track the parallel current independent of the parallel electric field¹. Solving by integrating factors² gives

$$J_3 \leftarrow J_3 \exp(-\nu \delta t) + \delta t \frac{ne^2}{m_e} E_3 \exp(-\nu \frac{\delta t}{2}) \quad (6.2)$$

¹The parallel current J_z is defined on the same points of the Yee grid as E_z . It is offset in time by half of a time step.

²The integrating factors technique is laid out explicitly for Ampère's law in Section 5.4.

From there, the parallel electric field can be updated directly; Equation (5.23) is replaced by the following:

$$E_3 \leftarrow E_3 + c^2 \delta t (g_{31} F^1 + g_{33} F^3) - \frac{\delta t}{\epsilon_0} J_3 \quad (6.3)$$

- 834 The present section explores the complications that arise from the addition of the elec-
- 835 tron inertial term to Ohm's law, as well as a few results that may be gleaned despite
- 836 those complications. Notably — for reasons discussed in Section 6.3 — the results
- 837 presented in Chapter 7 do not make use of the effects of electron inertia.
- 838 Inertial effects have been considered in previous numerical work, such as by Lysak and
- 839 Song[60, 61], but never at the global scale. Previous work has instead employed a quasi-
- 840 dipolar model which scales the cross-sectional area of flux tubes with altitude, but does
- 841 not properly account for their curvature.

842 6.1 The Boris Factor

With the addition of the electron inertial term, a cyclical dependence appears between Ampère's law and Ohm's law:

$$\frac{\partial}{\partial t} E_z \sim -\frac{1}{\epsilon_0} J_z \quad \text{and} \quad \frac{\partial}{\partial t} J_z \sim \frac{ne^2}{m_e} E_z \quad \text{so} \quad \frac{\partial^2}{\partial t^2} E_z \sim -\omega_P^2 E_z \quad (6.4)$$

- 843 That is, electron inertial effects come hand in hand with the plasma oscillation.
- 844 As mentioned in Chapter 4 and shown in Figure 6.1, plasma oscillation is quite fast —
- 845 several orders of magnitude smaller than Tuna's time step as determined in Section 5.1
- 846 ($\sim 10 \mu\text{s}$). This poses a conundrum. At Tuna's usual time step, the plasma oscillation
- 847 becomes unstable within seconds³. On the other hand, reducing the time step by three
- 848 orders of magnitude to resolve the plasma oscillation is computationally infeasible; a
- 849 run slated for an hour would require six weeks to complete.

³For stability, $\omega_P \delta t < 1$ is necessary.

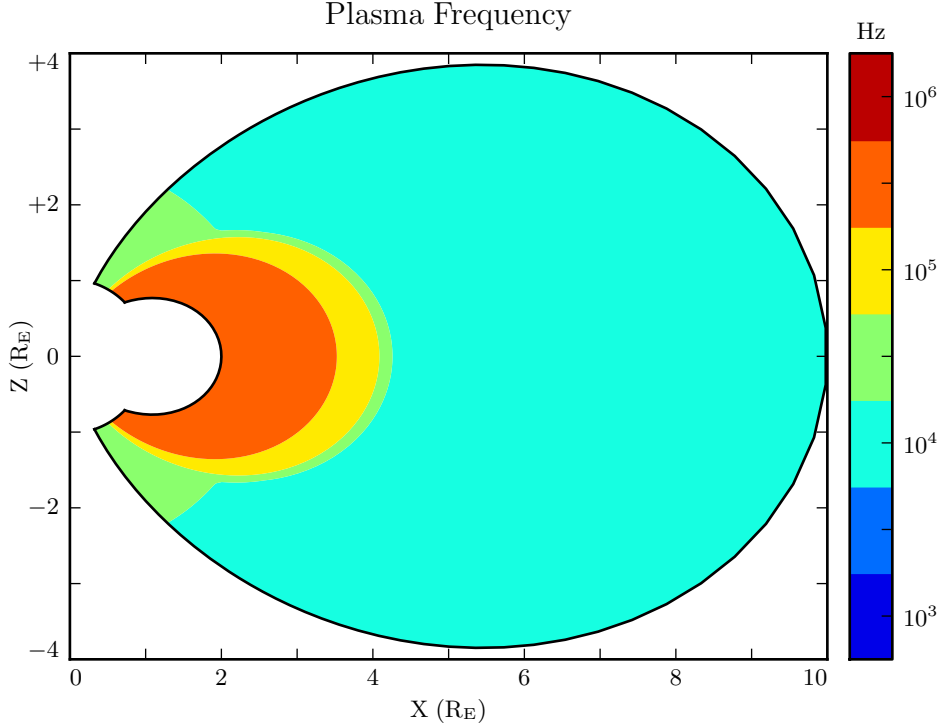


Figure 6.1: The plasma frequency reaches a peak value just under 10^6 Hz near the equator. Outside the plasmasphere, its value is closer to 10^4 Hz, which is still not well-resolved by Tuna's usual time step.

As it happens, this problem can be solved by artificially increasing the parallel electric constant above its usual value of ϵ_0 . Doing so lowers both the speed of light and the plasma frequency within the simulation. This technique — and others like it — has been widespread in numerical modeling since it was presented by Boris in 1970[6]. The following paraphrases an argument by Lysak and Song[60], outlining its validity specifically in the case of electron inertial effects.

Supposing that the current and electric field are oscillating at frequency ω , the parallel components of Ampère's law and Ohm's law can be written

$$-i\omega\epsilon_0 E_z = \frac{1}{\mu_0} (\nabla \times \underline{B})_z - J_z \quad -\frac{i\omega}{\nu} J_z = \sigma_0 E_z - J_z \quad (6.5)$$

Then, eliminating the current, the parallel electric field can be related to the curl of the magnetic field by⁴

$$\left(1 - \frac{\omega^2 - i\nu\omega}{\omega_P^2}\right) E_z = \frac{c^2}{\omega_P^2} (\nu - i\omega) (\nabla \times \underline{B})_z \quad (6.6)$$

- In Equation (6.6), $\frac{c}{\omega_P}$ is the electron inertial length. While the speed of light and the plasma frequency each depend on ϵ_0 , their ratio does not. This allows an estimation of how much the model should be affected by an artificially-large electric constant (and thus an artificially-small plasma frequency). So long as $\frac{\omega^2 - i\nu\omega}{\omega_P^2}$ remains small compared to unity, the model should behave physically.
- For waves with periods of a minute or so, even perhaps-implausibly large Boris factors are allowed; for example, increasing ϵ_0 by a factor of 10^6 gives $\left|\frac{\omega^2 + i\omega\nu}{\omega_P^2}\right| \lesssim 0.01$.

6.2 Parallel Currents and Electric Fields

- As discussed in Section 4.4, parallel electric fields in this regime are expected to be at least six orders of magnitude smaller than the perpendicular electric fields. Numerical results show general agreement: in Figure 6.2, the parallel electric field appears comparable to its perpendicular counterparts only after its been scaled up by a factor of 10^6 .

- As such, the inclusion of electron inertial effects does not appreciably impact the simulation's gross behavior. In Faraday's law, $\nabla \times \underline{E}$ is unaffected, to the extent that side-by-side magnetic field snapshots with and without electron inertial effects are not visibly distinguishable (not shown). In a sense, this is reassuring. It ensures that the present section does not cast doubt on the results presented in Chapter 7, where electron inertial effects are neglected.

⁴From Equation (4.4), $c^2 \equiv \frac{1}{\mu_0 \epsilon_0}$ and $\sigma_0 \equiv \frac{ne^2}{m_e \nu}$ and $\omega_P^2 \equiv \frac{ne^2}{m_e \epsilon_0}$.

Electric Field Snapshots: Quiet Day, 16mHz Current, $m = 16$

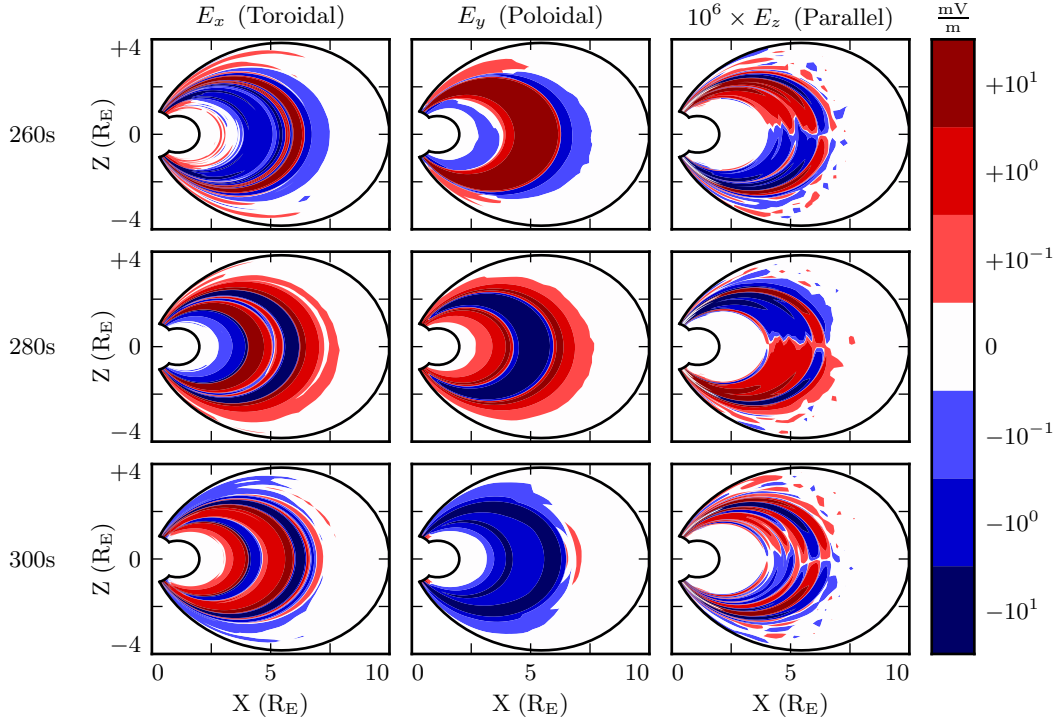


Figure 6.2: Parallel electric fields are smaller than perpendicular electric fields by about six orders of magnitude. As a result, parallel electric fields do not contribute significantly to $\nabla \times \underline{E}$ in Faraday's law.

- 875 Even if there is no significant feedback through Faraday's law, it's informative to con-
 876 sider the structures that arise in parallel currents and electric fields driven by pertur-
 877 bations in the ring current. For example, in Figure 6.2, the parallel electric field per-
 878 turbation (with maxima near the ionosphere) exhibits the opposite harmonic structure
 879 to the perpendicular electric field components (which peak near the equator).
- 880 Figure 6.3 shows how parallel currents lines up with the Poynting flux over time. Four
 881 runs are shown, one per row. The horizontal axis is time, and the vertical axis is latitude.
 882 The real and imaginary components of the parallel current are shown in the first and
 883 third columns respectively, while the second and fourth columns show the poloidal and
 884 toroidal Poynting flux. Values are taken at an altitude of 1000 km.

Current and Poynting Flux at 1000km: Quiet Day , 16mHz Current

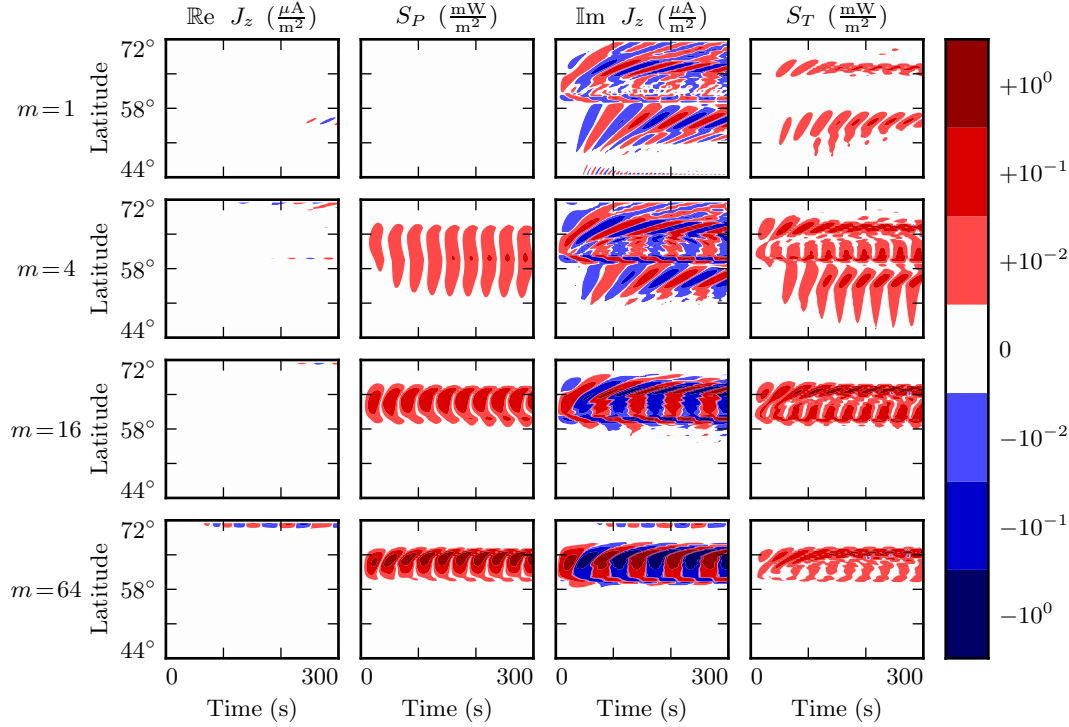


Figure 6.3: Parallel current and Poynting flux is shown for four runs, one per row, measured at an altitude of 1000 km. The parallel current is overwhelmingly imaginary, which implies a connection to the toroidal mode. Appropriately enough, the structure of the parallel current (particularly at low modenumber) seems to resemble the structure of the toroidal mode more than it does that of the poloidal mode. This is likely because the toroidal mode, with its sharp gradients across L -shells, dominates $(\nabla \times \underline{B})_z$.

- 885 Poloidal and toroidal fields are overwhelmingly real and imaginary respectively, because
 886 they are separated from one another by an azimuthal derivative (which carries a factor
 887 of i). However, when a wave's polarization is rotated by the Hall conductivity, there
 888 is no accompanying rotation in the complex plane — this gives rise to an imaginary
 889 component of the poloidal wave and a real component of the toroidal wave.
- 890 In Figure 6.3, the ionospheric conductivity is small, so the imaginary component of the
 891 parallel current dominates. This implies a connection between the parallel current and
 892 the toroidal mode, and indeed, the two do exhibit qualitatively similarities. At $m = 4$

893 in particular, the poloidal and toroidal Poynting fluxes are similar in strength much of
894 the time, yet the form of the parallel current strongly resembles that of the toroidal
895 Poynting flux over the poloidal.

896 The toroidal mode's dominant effect on the parallel current at small m is not surprising.
897 As shown in Figure 6.2, toroidal waves vary sharply in L^5 . When the poloidal and
898 toroidal magnetic fields are comparable in magnitude, $\frac{\partial}{\partial x} B_y$ typically exceeds $\frac{\partial}{\partial y} B_x$ (at
899 least for $m \lesssim 32$).

900 Whereas the imaginary component of the parallel current corresponds to that carried
901 into the ionosphere by Alfvén waves, its real component comes from electric fields rotated
902 by the Hall conductivity. Figure 6.4 shows the same four runs as Figure 6.3, but
903 measured at 100 km, the Earthward boundary of the simulation. At that point, the real
904 and imaginary components are similar in magnitude.

905 In Figure 6.4, as in Figure 6.3, the imaginary component of the parallel current prefer-
906entially follows the toroidal Poynting flux. This is particularly apparent at $m = 16$,
907 where the poloidal Poynting flux is clearly stronger, yet the structure of the imaginary
908 current resembles that of the toroidal Poynting flux. The real parallel current, on the
909 other hand, appears to follow the poloidal Poynting flux.

910 Put another way, low- m poloidal waves seem to primarily give rise to field-aligned
911 currents only after being rotated to the toroidal mode by the Hall conductivity. At
912 high modenumber, the two modes contribute comparably to the formation of parallel
913 currents.

It's also possible to consider the effect of parallel currents and electric fields on the
ionosphere's energy budget, per Poynting's theorem:

$$\frac{\partial}{\partial t} u = -\nabla \cdot S - J \cdot E \quad (6.7)$$

914 The magnitude of the parallel current tops out over $1 \mu\text{A}/\text{m}^2$, just shy of the up-to-tens
915 of $\mu\text{A}/\text{m}^2$ inferred from ground observations and seen in situ[8, 45, 80]. However, this

⁵The sharp definition in L of the toroidal mode compared to the poloidal mode is also the topic of significant discussion in Chapter 7.

Current and Poynting Flux at 100km: Quiet Day , 16mHz Current

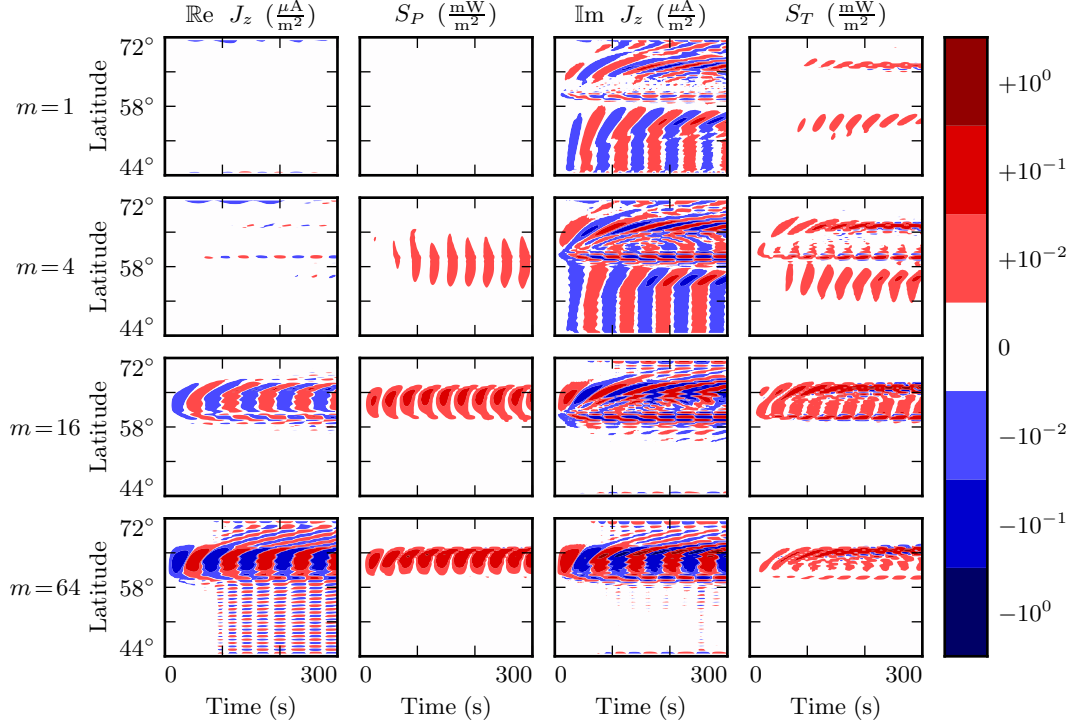


Figure 6.4: The above slices are taken from the same runs shown in Figure 6.3, but at an altitude of 100 km instead of 1000 km. The primary difference between the two altitudes is the strength of the ionospheric Hall conductivity, which directly couples the poloidal and toroidal modes. The Hall-rotated fields give rise to a real component of the parallel current, the structure of which follows the poloidal Poynting flux (as it rotates to the toroidal mode).

current is not a significant contributor to ionospheric Joule dissipation. As shown in Figure 6.5, the energy deposited in the ionosphere by the Poynting flux matches closely with the energy lost to Joule dissipation — as it should, to conserve energy. But, according to the model, Pedersen and Hall are dominant. The parallel component of $\underline{J} \cdot \underline{E}$ is smaller by several orders of magnitude.

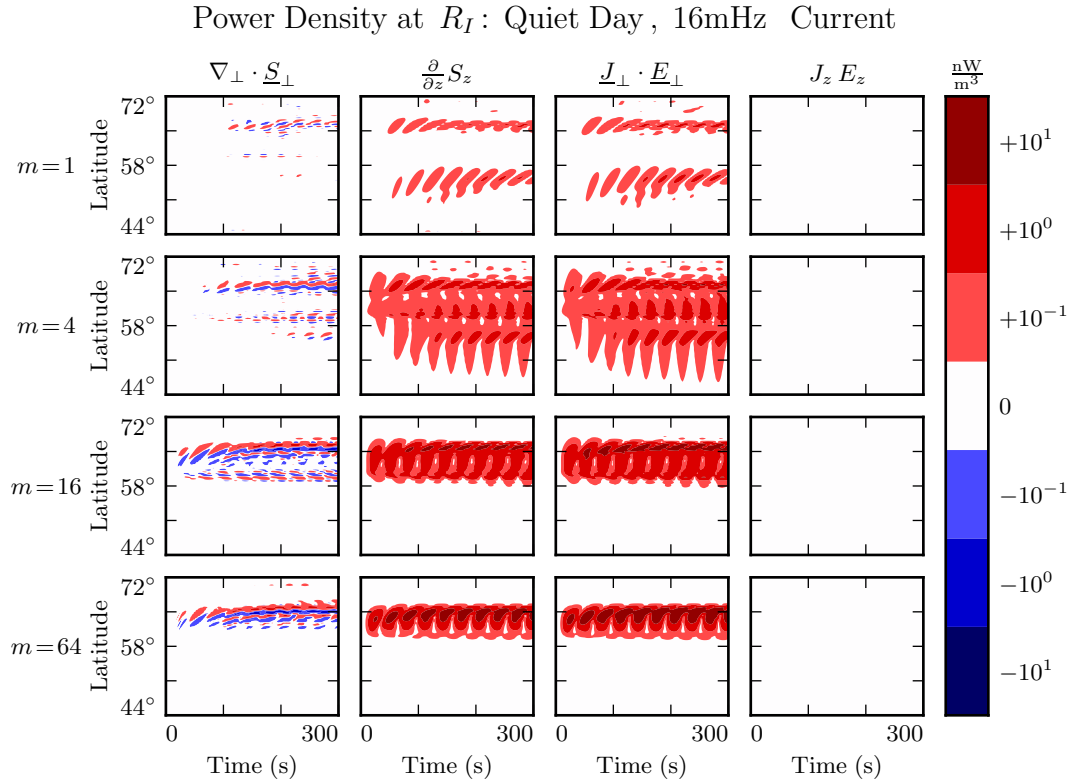


Figure 6.5: While field-aligned currents can be of significant size, they are not particularly good at depositing energy in the ionosphere. Energy deposited by the Poynting flux matches closely with Joule dissipation from the perpendicular currents, while $J_z E_z$ is smaller by several orders of magnitude.

921 6.3 Inertial Length Scales

- 922 It's not quite fair to compare the parallel and perpendicular contributions to $\nabla \times \underline{E}$ as
 923 is done in Section 6.2. Perpendicular electric fields are on the order of 1 mV/m, with
 924 wavelengths on the order of 10^5 km; they cause magnetic fields to change at a rate of
 925 around 0.1 nT/s. Parallel electric fields, closer to 10^{-6} mV/m, would need to vary over
 926 length scales of 0.1 km to match with that.
- 927 Such scales are believable. The characteristic length scale of the plasma oscillation is the
 928 electron inertial length, $\frac{c}{\omega_P}$, which is on the order of 1 km in the auroral ionosphere and

929 0.1 km in the low-altitude plasmasphere. However, Tuna’s grid out bottoms out closer
 930 to 10 km. That is, with the inclusion of electron inertial effects, the grid is too coarse
 931 to resolve all of the waves expected to be present. The model is prone to instability as
 932 a result — for example, “wiggles” are visible in the bottom-left subplot of Figure 6.4.

933 Figure 6.6 shows a run with perpendicular resolution smaller than the electron inertial
 934 length, side by side with an analogous run on the typical grid described in Chapter 5. In
 935 order to carry out the inertial-scale run, several concessions were made to computational
 936 cost. The run simulates only a duration of 100 s (other figures in the present chapter,
 937 and those in Chapter 7, show 300 s), and the grid covers only the auroral latitudes from
 938 $L = 5$ to $L = 7$.

Parallel Electric Fields: Quiet Day, 100s of 16mHz Current, $m = 16$

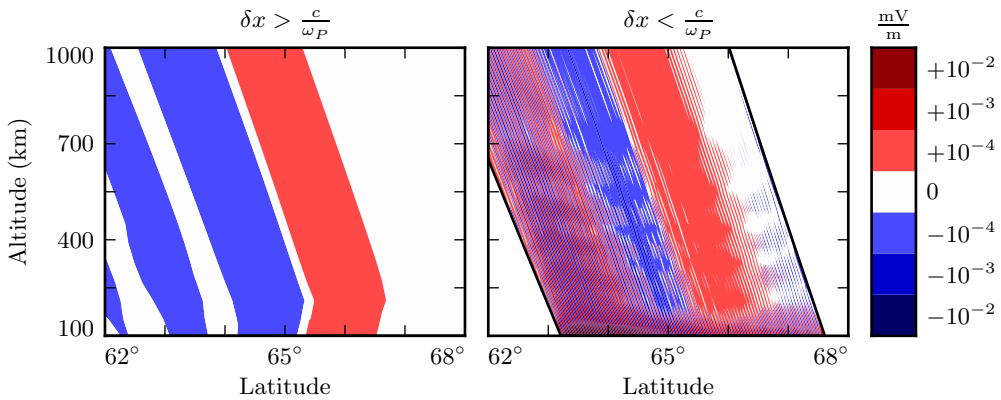


Figure 6.6: The parallel electric field develops significant structure when the perpendicular grid resolution is smaller than the electron inertial length. Unfortunately, such runs are prohibitively expensive. The subplot on the right — which still fails to resolve wave structure properly — represents a 100-fold increase in computational time compared to that on the left.

939 Even so, the run presents a significant computational expense. Spread over 16 cores,
 940 a 100 s run on Tuna’s usual grid takes well under an hour. The inertial-scale run
 941 barely finished in 96 hours, the cutoff at the Minnesota Supercomputing Institute. This
 942 is because runtime goes as the inverse square of grid resolution; not only does finer

resolution require more grid cells, but it also gives rise to proportionally smaller crossing times, imposing a smaller time step.

The snapshot shown in Figure 6.6 uses a perpendicular grid resolution of 0.7 km at the Earthward edge, which just satisfies the Nyquist rate for the minimum inertial length of 1.7 km. It’s still too coarse. There is clearly some small-scale structure developing in the ionosphere, but it’s not well resolved. The large number of “wiggles” portends an imminent crash.

Tuna’s grid can be limited by considering only a small range of L -shells, as in Figure 6.6, but ultimately enough points are necessary to resolve the entire length of a magnetic field line. The time step also must remain small — because waves can propagate in any direction, the perpendicular Courant condition must be respected. That is, at present, Tuna’s limited ability to resolve inertial effects is simply a scaling issue.

6.4 Discussion

The present chapter is a proof of concept: the addition of electron inertial effects to Tuna presents a promising first-principles-based approach to the investigation of parallel currents and electric fields associated with field line resonances. Electric fields arise which are consistent in magnitude with those predicted by the dispersion relation, and parallel currents fall within an order of magnitude or so of observed values, even when inertial length scales are not properly resolved.

Results in Section 6.2 suggest a disparity between low- m poloidal and toroidal FLRs in terms of the parallel current response. At low altitude, where the two modes are directly coupled by the Hall conductivity, both seem to be accompanied by parallel currents. However, in regions of low Hall conductivity, parallel currents appear to preferentially accompany toroidal waves. This is likely a result of the toroidal mode’s sharp gradients across L -shells.

Future work could consider the relationship between the dynamic height-integrated potentials and the accompanying parallel currents, specifically with respect to the Knight relation[50]. Inertial effects could also be accompanied by test particles, in order to

971 gauge the precipitation that would be expected to accompany global Alfvénic potential
972 structures.

973 Unfortunately, simulations are prone to instability when inertial length scales are not
974 properly resolved. And, at least at present, resolving those scales poses a prohibitive
975 computational expense. For this reason, the consideration of inertial effects is limited to
976 the present chapter; results in Chapter 7 make use of the core version of Tuna presented
977 in Chapter 5, which does not include the effects of electron inertia.

978 Notably, the addition or omission of parallel currents and electric fields does not appear
979 to significantly alter the behavior of perpendicular electric fields or magnetic fields.
980 Because the parallel electric fields are relatively small, $\nabla \times \underline{E}$ is essentially unaffected
981 by their inclusion. Joule dissipation from parallel currents also does not seem to be a
982 significant in comparison to that from Pedersen and Hall currents.

983 **Chapter 7**

984 **Numerical Results**

985 The primary motivation for Tuna’s development is the fact that Pc4s and Pgs exhibit
986 a variety of heretofore-unconnected properties, and that existing models are limited in
987 their ability to investigate them. The present chapter discusses the core results Tuna has
988 so far produced. Particular attention is paid to the importance of azimuthal modenumber — a characteristic which is particularly difficult to study using three-dimensional
989 models, and which is of importance to poloidal-toroidal coupling, compressional propa-
990 gation, and giant pulsations.
991

992 **7.1 Modenumber and Compression**

993 It’s well known that the poloidal FLR mode is compressional at low modenumber, but
994 guided at high modenumber. However, the relationship is not well quantified. Theoreti-
995 cal work has historically been concerned with the limits $m \rightarrow 0$ and $m \rightarrow \infty$ [14, 76], and
996 only a handful of satellite observations have explicitly considered an event’s azimuthal
997 modenumber[17, 69, 88]. Using results from Tuna, the present section examines the
998 strength of the poloidal wave’s compressional component at an ensemble of finite mod-
999 enumbers.

1000 Figures 7.1 and 7.2 show magnetic field snapshots taken from a pair of runs; the first
1001 uses a small azimuthal modenumber, and the second uses a large one. The runs are

1002 otherwise identical: both simulations use the quiet dayside ionospheric profile, and both
1003 are driven at 22 mHz.

1004 The differences between the two runs are striking. At low modenumber, wave activity
1005 is visible throughout the simulation domain. Structure in the poloidal magnetic field is
1006 only vaguely governed by the dipole geometry, and the compressional magnetic field is
1007 comparably strong to the two perpendicular components.

1008 In contrast, at high modenumber, the poloidal magnetic field is localized to $L \sim 5$, where
1009 the driving is delivered. The compressional field is weaker than the poloidal field by
1010 at least an order of magnitude. A third-harmonic poloidal mode is visible at the outer
1011 boundary — its magnitude is just barely large enough to be visible on the logarithmic
1012 scale. The gap between $L \sim 5$ (where 22 mHz matches a first-harmonic FLR) and
1013 $L \sim 10$ (where 22 mHz matches a third-harmonic FLR) speaks to the evanescence of
1014 non-guided waves above the compressional Alfvén cutoff frequency¹.

1015 In both the low- m and high- m runs, toroidal activity is more or less coincident with
1016 poloidal activity — as is to be expected, since the driving is purely poloidal, and so
1017 the poloidal mode must be the source of the toroidal mode. It is further notable that
1018 the toroidal mode is sharply guided. Particularly in Figure 7.2, strong, narrow, toroidal
1019 FLRs of opposite phase can be seen oscillating very close to one another. Strong poloidal
1020 waves, in contrast, are smeared in L .

1021 Snapshots are not shown for runs carried out using the other ionospheric profiles (active
1022 day, quiet night, and active night). The morphology of their waves is qualitatively
1023 similar. The differences between the profiles is considered in Sections 7.2 to 7.4.

1024 Figure 7.3 quantifies the compressional component of the poloidal mode as a function of
1025 modenumber. Each subplot corresponds to a different run of Tuna; the runs shown in
1026 Figures 7.1 and 7.2 are in the rightmost column, second from the top and second from the
1027 bottom respectively. The red line indicates the ratio between the RMS compressional
1028 magnetic field and the RMS poloidal magnetic field; both averages are taken over the
1029 entire simulation “volume” each time step. Mean values are shown in black.

¹See Section 4.4.

1030 At $m = 1$, the compressional and poloidal magnetic fields are comparable in magnitude.
1031 As m increases, however, the compressional component quickly falls off. The compres-
1032 sional component is half the strength of the poloidal component at $m \sim 5$, and a quarter
1033 by $m \sim 10$. Similar behavior is seen using the active dayside and active nightside pro-
1034 files (not shown). On the quiet nightside (not shown), the compressional component of
1035 the poloidal mode does not fall off quite as sharply; $\left| \frac{B_z}{B_x} \right|$ falls to 50 % at $m \sim 8$ and to
1036 25 % at $m \sim 16$.

1037 A slight frequency dependence is apparent across each row in Figure 7.3. Compressional
1038 coupling falls off slower for waves at higher frequency. This is because higher-frequency
1039 waves are that much closer to the cutoff frequency, and so their propagation across
1040 L -shells is that much less evanescent.

1041 Notably, the waves considered in the present work are fundamental harmonics. The
1042 compressional behavior of the poloidal mode may vary for the (more-common) second
1043 harmonic: Radoski suggests that the asymptotic value of $\left| \frac{B_z}{B_x} \right|$ is inversely proportional
1044 to the harmonic number[76].

Magnetic Field Snapshots: Quiet Day , 22mHz Current, $m = 2$

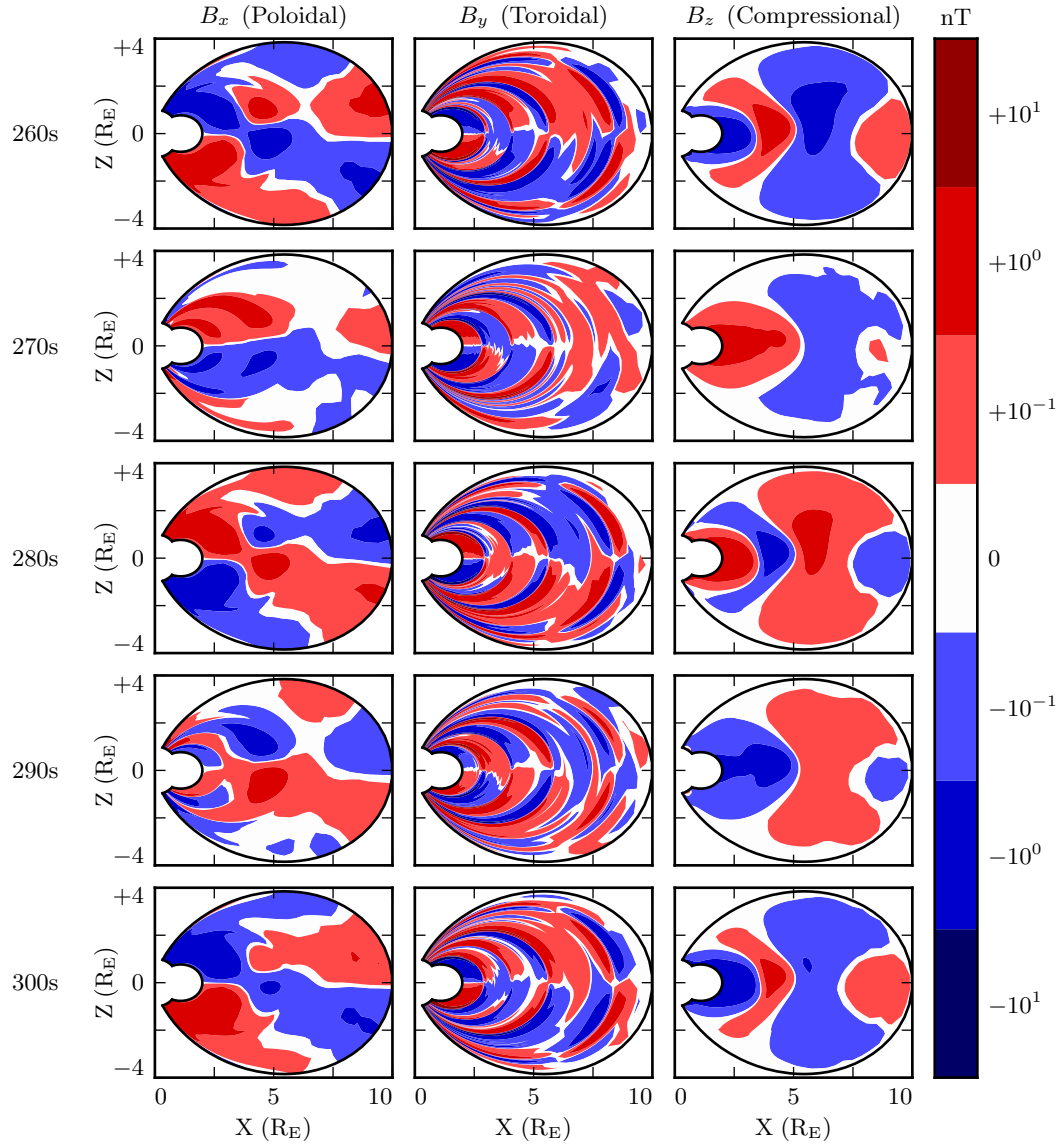


Figure 7.1: Each row in the above figure is a snapshot in time. The three columns show the simulated poloidal, toroidal, and compressional magnetic fields. Due to the run's low azimuthal modenumber, the poloidal mode has a significant compressional component. This is visible both in the fact that B_z is comparable in size to B_x , and in that structure in B_x is only vaguely guided by the geometry of the magnetic field. Toroidal waves, in contrast, are sharply guided.

Magnetic Field Snapshots: Quiet Day , 22mHz Current, $m = 32$

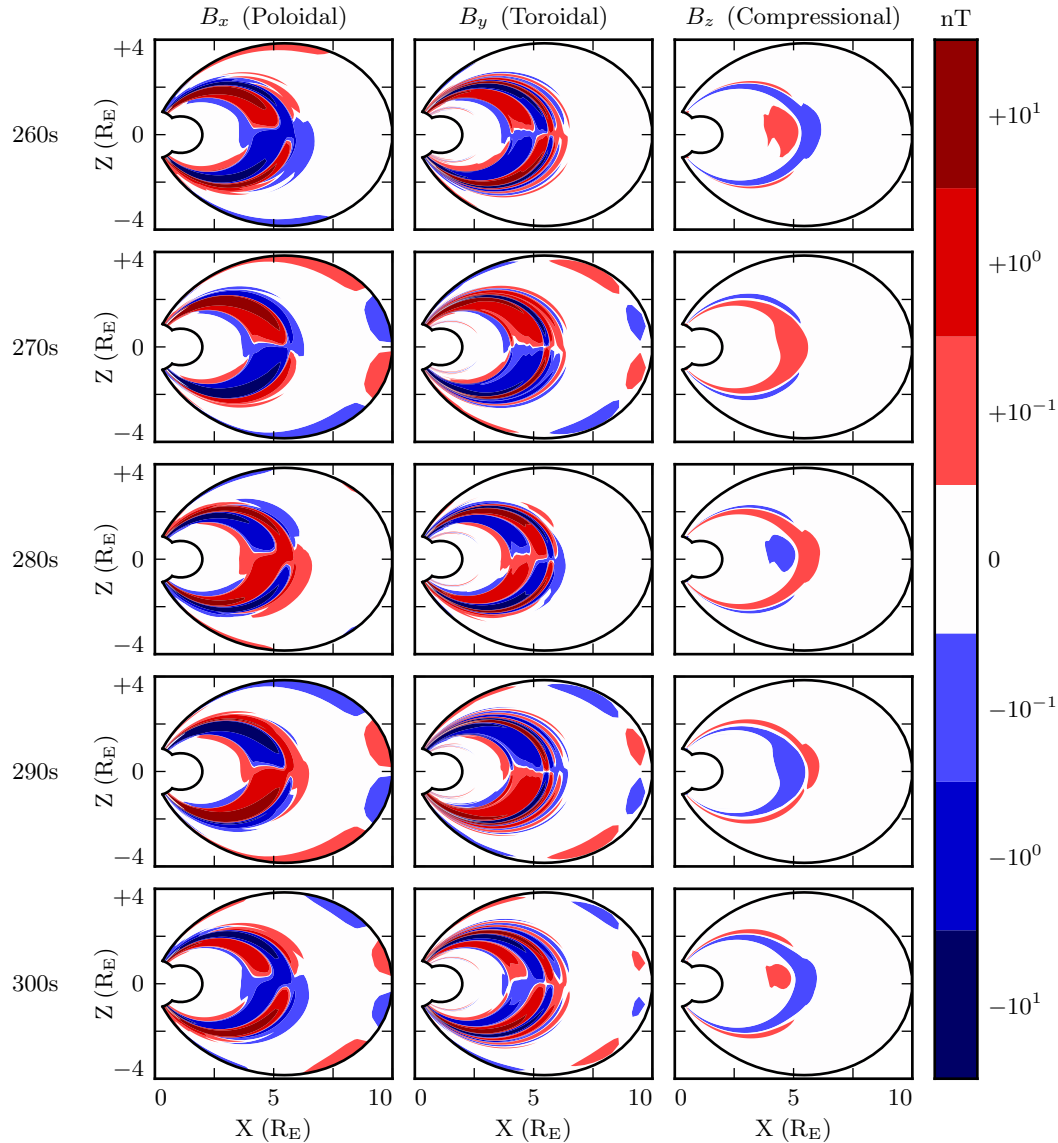


Figure 7.2: The above figure is analogous to Figure 7.1, but the run uses a large azimuthal modenumber. The change has a dramatic effect. The poloidal wave is concentrated much more sharply in L , and its compressional component is weaker by an order of magnitude. Regardless of modenumber, toroidal waves exist at a range of L shells similar to poloidal waves, and show sharp definition across L -shells.

Compressional Coupling to the Poloidal Mode: Quiet Day

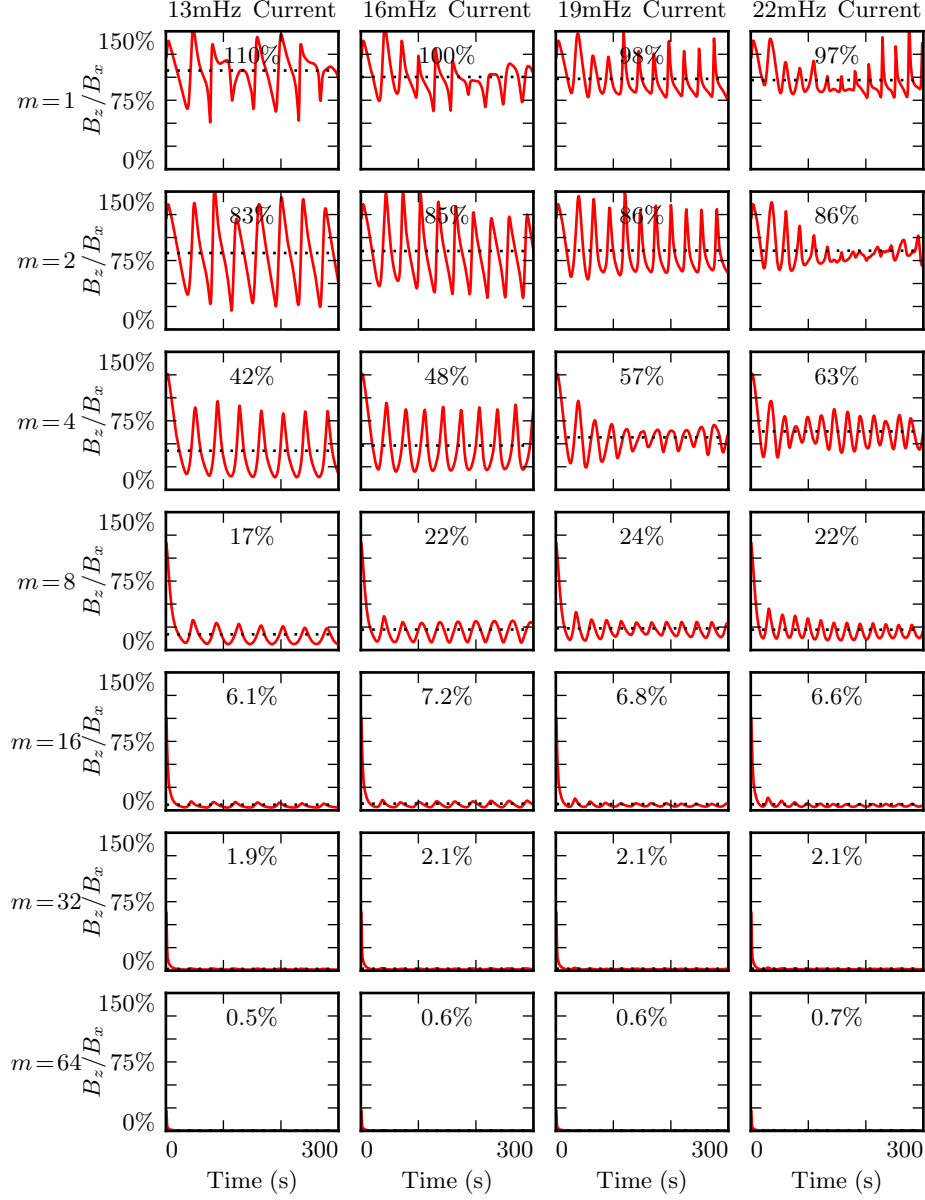


Figure 7.3: Each subplot above corresponds to a different run; the runs shown in Figures 7.1 and 7.2 are in the rightmost column, second from the top and second from the bottom respectively. Red lines indicate the ratio between the RMS compressional and poloidal magnetic fields. Mean values are shown in black. The compressional field is comparable to the poloidal field at $m = 1$, but falls quickly.

1045 **7.2 Resonance and Rotation on the Dayside**

1046 In his 1974 paper, Radoski argues that a poloidally-polarized wave should asymptotically
1047 rotate to the toroidal polarization[76] as a result of the curved derivative in the meridional plane. The question of finite poloidal lifetimes is considered further in a
1048 1995 paper by Mann and Wright[65], using a straightened field line and an Alfvén speed
1049 gradient in the “radial” direction. They also found a rotation over time from poloidal to
1050 toroidal polarization, with the characteristic time proportional to the azimuthal mode-
1051 number.
1052

1053 The present section builds on the aforementioned results by relaxing several of their non-
1054 physical assumptions. Tuna’s geometry is more realistic than Radoski’s half-cylinder or
1055 the box model used by Mann and Wright. Previous work has considered the evolution
1056 of an initial condition, while the simulations shown below include driving delivered
1057 over time. In addition, Tuna features a finite, height-resolved ionospheric conductivity
1058 profile, rather than the perfectly-reflecting boundaries used in the past.

Each subplot in Figure 7.4 is analogous to Figure 3 in Mann and Wright’s paper[65]. Blue lines show the total energy in the poloidal mode as a function of time. Red lines show toroidal energy. Runs are organized analogous to those in Figure 7.3: drive frequency is constant down each column, and azimuthal modenum is constant across each row. Axis bounds are held constant across all subplots. The poloidal and toroidal energy are computed by integrating over the electromagnetic energy density, per Poynting’s theorem:

$$U_P = \int \frac{dV}{2\mu_0} \left(B_x^2 + \frac{1}{v_A^2} E_y^2 \right) \quad U_T = \int \frac{dV}{2\mu_0} \left(B_y^2 + \frac{1}{v_A^2} E_x^2 \right) \quad (7.1)$$

1059 Where the differential volume dV is computed using the Jacobian² to account for Tuna’s
1060 unusual geometry. The integral is evaluated in u^1 and u^3 but not u^2 (Tuna’s missing
1061 half-dimension), which gives energy in units of gigajoule per radian. More than anything
1062 else, this serves as a reminder that Pc4 pulsations are localized in MLT.

²See Section 5.1.

1063 The 28 runs shown in Figure 7.4 use an ionospheric profile corresponding to the dayside
1064 during times of low solar activity, where the conductivity is relatively high. The active
1065 and quiet dayside profiles are briefly contrasted in Section 7.4; for the most part, the
1066 focus of the present work is on the difference between the dayside and the nightside
1067 (Section 7.3). Differences between the two dayside profiles are small in comparison.

1068 The fact that red (toroidal) lines appear at all in Figure 7.4 speaks to a net rotation
1069 of energy from the poloidal mode to the toroidal. As discussed in Section 5.3, Tuna's
1070 driving is delivered purely into the poloidal electric field, reflecting a perturbation in
1071 the magnitude of the ring current.

1072 As expected, the rotation from poloidal to toroidal is slowest at large azimuthal mode-
1073 numbers. The toroidal energy overtakes the poloidal energy within a single drive period
1074 at small m ; at $m = 64$, the most of the energy is in the poloidal mode for ~ 10 peri-
1075 ods. However, the relationship between azimuthal modenumber and rotation timescale
1076 is not linear, as was suggested by Mann and Wright. Instead, in a practical setting, the
1077 rotation is fastest at $m \sim 4$.

1078 This is explained by the compressional character of the poloidal mode. At very low
1079 modenumber, energy in the poloidal mode moves readily across L -shells. A significant
1080 fraction of that energy is lost to the outer boundary before rotating to the toroidal
1081 mode. At high modenumber, compressional propagation is evanescent, so all energy
1082 in the poloidal mode must ultimately rotate to the toroidal mode or be lost to Joule
1083 dissipation.

1084 Joule dissipation is a major player in the system's energy economy. However, due to the
1085 highly conductive dayside ionosphere, dissipation timescales are in the tens of Pc4 wave
1086 periods. Energy loss through Joule dissipation asymptotically balances energy input
1087 from driving, but most of that energy is not lost until after it has rotated from the
1088 poloidal mode to the toroidal. As such, in most runs shown in Figure 7.4, the energy
1089 content of the toroidal mode asymptotically exceeds that of the poloidal mode.

1090 The asymptotic energy content of the system also depends on how well the drive fre-
1091 quency matches the local eigenfrequency. If the two do not match, energy is lost to
1092 destructive interference between the standing wave and the driving.

1093 In principle, energy moves between the poloidal and toroidal modes due to their direct
1094 coupling through the ionospheric Hall conductivity. In practice, this effect does not
1095 move large amounts of energy. When the runs shown in Figure 7.4 are repeated with
1096 the Hall conductivity set to zero, the resulting energy curves are not visibly different
1097 (not shown).

1098 The low- m runs at 19 mHz merit additional discussion. These runs accumulate energy
1099 over a large number of wave periods, while the low- m waves at 13 mHz, 16 mHz, and
1100 22 mHz do not. This effect is likely nonphysical. At 19 mHz, a third-harmonic resonance
1101 forms very close to the outer boundary, and is likely enhanced by nonphysical reflections
1102 against the simulation boundary.

1103 The presence of individual harmonics can be seen in the contours shown in Figures 7.5
1104 and 7.6. These figures show the same runs as Figure 7.4, arranged in the same way on
1105 the page. However, instead of showing the total energy integrated over the simulation
1106 domain, the energy densities are averaged over the volume of each flux tube individually.
1107 Figure 7.5 shows contours of poloidal energy density and Figure 7.6 shows toroidal
1108 energy density.

1109 The top few rows of Figure 7.5 confirm that the poloidal mode's compressional nature is
1110 to blame for its failure to accumulate energy at low modenumber. Waves move so readily
1111 across field lines that no visible amount of energy builds up at $L \sim 5$, the location of the
1112 driving. Some energy moves inward, and is trapped by the peak in Alfvén speed just
1113 inside the plasmapause, while the rest moves to the outer boundary. The time spent
1114 moving across field lines counts against the poloidal mode's finite lifetime, inhibiting
1115 the buildup of poloidal energy density even at L -shells where the wave matches the local
1116 eigenfrequency.

1117 As m increases, the energy distribution becomes more concentrated in L , though indi-
1118 vidual features remain fairly broad. At $m = 8$, runs at 13 mHz and 16 mHz are inclined
1119 to build up energy just inside the plasmapause, while those at 19 mHz and 22 mHz res-
1120 onate just outside the plasmapause; in all four cases, the energy is spread over a range
1121 of at least 1 in L .

1122 The peak energy density in the bottom-right run (22 mHz driving, $m = 64$) is by far the
1123 largest of any run in Figure 7.5. The azimuthal modenumber is large, so the poloidal
1124 mode is purely guided; energy is not smeared across multiple L -shells. And, crucially, the
1125 frequency of the driving matches closely with the Alfvén frequency at $L \sim 5$. Other runs
1126 on the bottom row are also guided, but they reach lower asymptotic energy densities
1127 because of a mismatch between the drive frequency and the local eigenfrequency —
1128 resulting in destructive interference between the standing wave and its driver.

1129 Giant pulsations are typically seen at ~ 10 mHz, well below the 22 mHz poloidal peak
1130 shown in Figure 7.5. Part of the discrepancy is likely due to the position of the driving.
1131 Pgs are most common at latitudes of $\sim 66^\circ$, which maps out to $L \sim 6$, whereas these
1132 runs are driven at $L \sim 5$. The size of the plasmapause also has a significant effect.
1133 When the runs in Figure 7.5 are repeated with the plasmapause at $L = 5$ instead of
1134 $L = 4$, the strongest resonance (driven at $L \sim 5$) drops from 22 mHz to 16 mHz (not
1135 shown).

1136 Whereas the poloidal contours are smeared over a swath of L -shells (though the high- m
1137 runs less so), the toroidal contours in Figure 7.6 appear only where the wave frequency
1138 matches the local eigenfrequency. A horizontal line drawn through the Alfvén speed
1139 frequency profiles (recall Figure 3.1) intersects the profile up to three times: once as
1140 the Alfvén frequency drops through the Pc4 range from its low-latitude peak, again as
1141 the Alfvén frequency rises sharply at the plasmapause, and a third time as the Alfvén
1142 frequency drops asymptotically. Toroidal waves can be seen resonating at all three of
1143 these locations in the $m = 4$, 22 mHz run in Figure 7.6, along with a third harmonic at
1144 large L . This is consistent with observations: toroidal resonances are noted for having
1145 frequencies which depend strongly on L , in contrast to the poloidal mode's less-strict
1146 relationship between frequency and location.

1147 In only one of the runs shown in Figure 7.5 does the poloidal mode attain an energy
1148 density on the order of 10^{-1} nJ/m³. On the other hand, the toroidal mode reaches
1149 $\sim 10^{-1}$ nJ/m³ in six of the runs in Figure 7.6. That is, the poloidal mode only exhibits
1150 a high energy density on the dayside only when conditions are ideal; the toroidal mode
1151 isn't nearly so particular.

Poloidal (Blue) and Toroidal (Red) Energy: Quiet Day

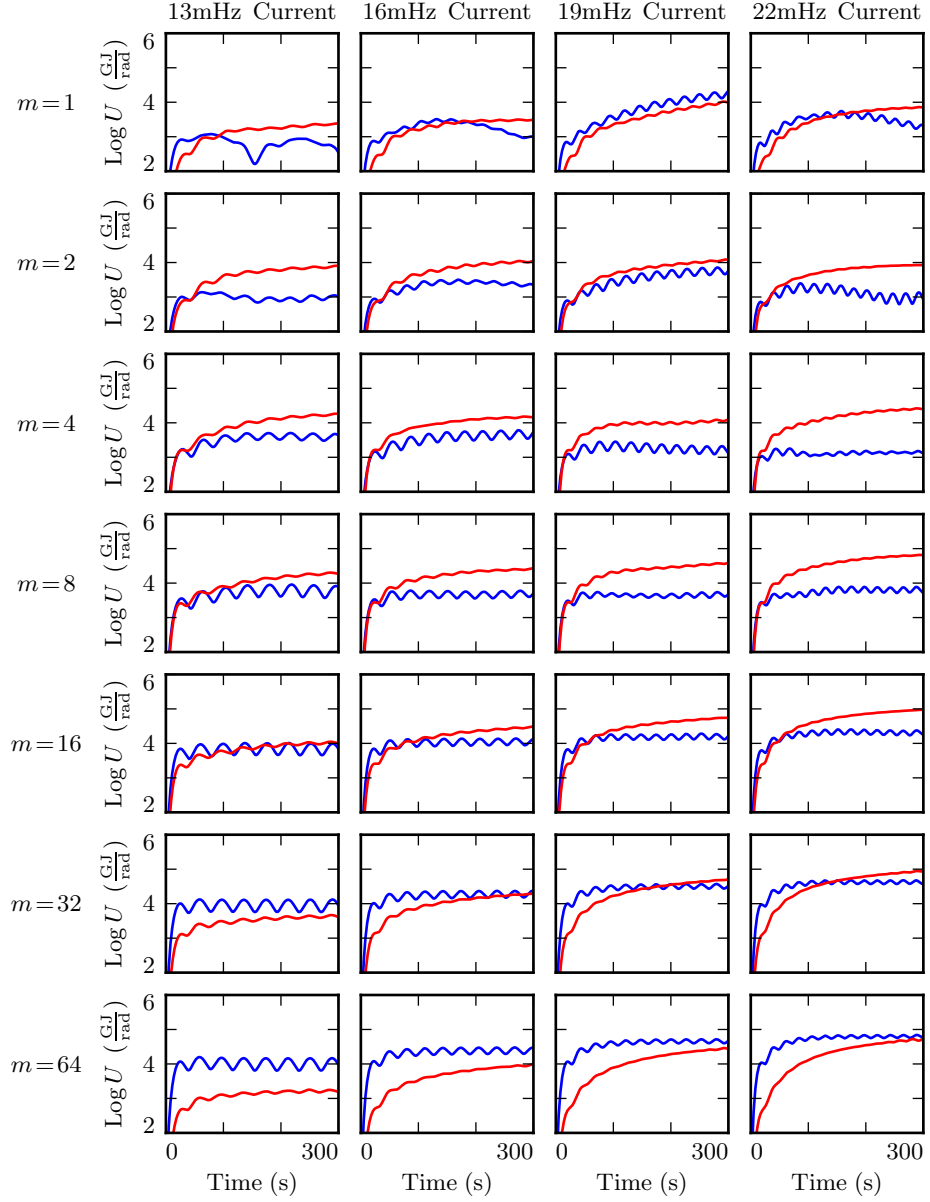


Figure 7.4: Each subplot above shows the poloidal (blue) and toroidal (red) energy for a simulation as a function of time. Each row contains four simulations, each with the same azimuthal modenumber; the seven rows in each column share a drive frequency. Driving is purely poloidal, but energy rotates asymptotically to the toroidal mode, and rotation is slowest at high modenumber.

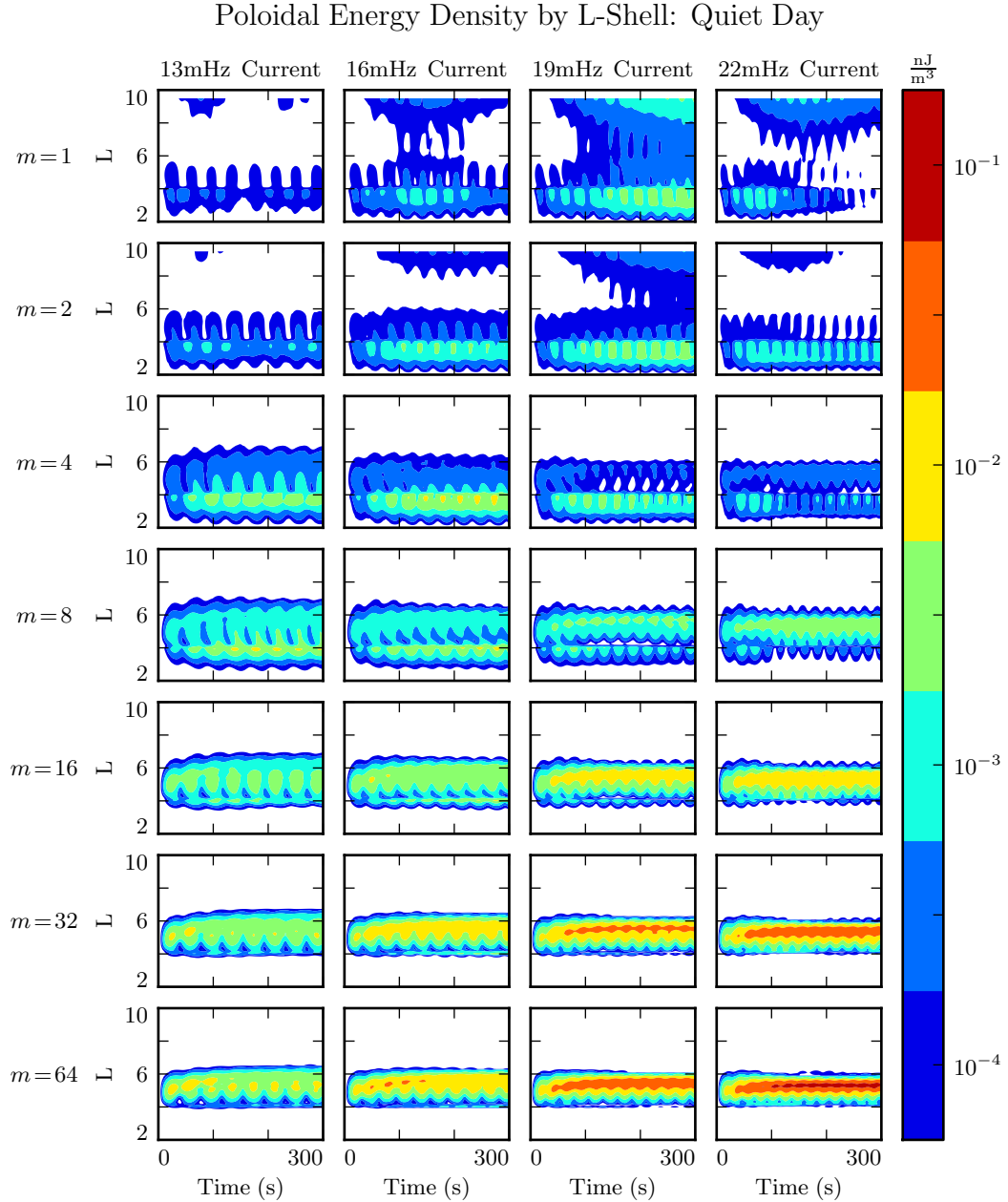


Figure 7.5: At low modenumber (top rows), the compressional nature of the poloidal mode allows energy to escape the simulation. At high modenumber (lower rows), the poloidal mode is guided; energy is trapped at the L -shell where it's injected, and rotation to the toroidal mode is slow — ideal conditions for resonance. But energy buildup is lackluster except where the drive frequency matches the local eigenfrequency (best in the rightmost row).

Toroidal Energy Density by L-Shell: Quiet Day

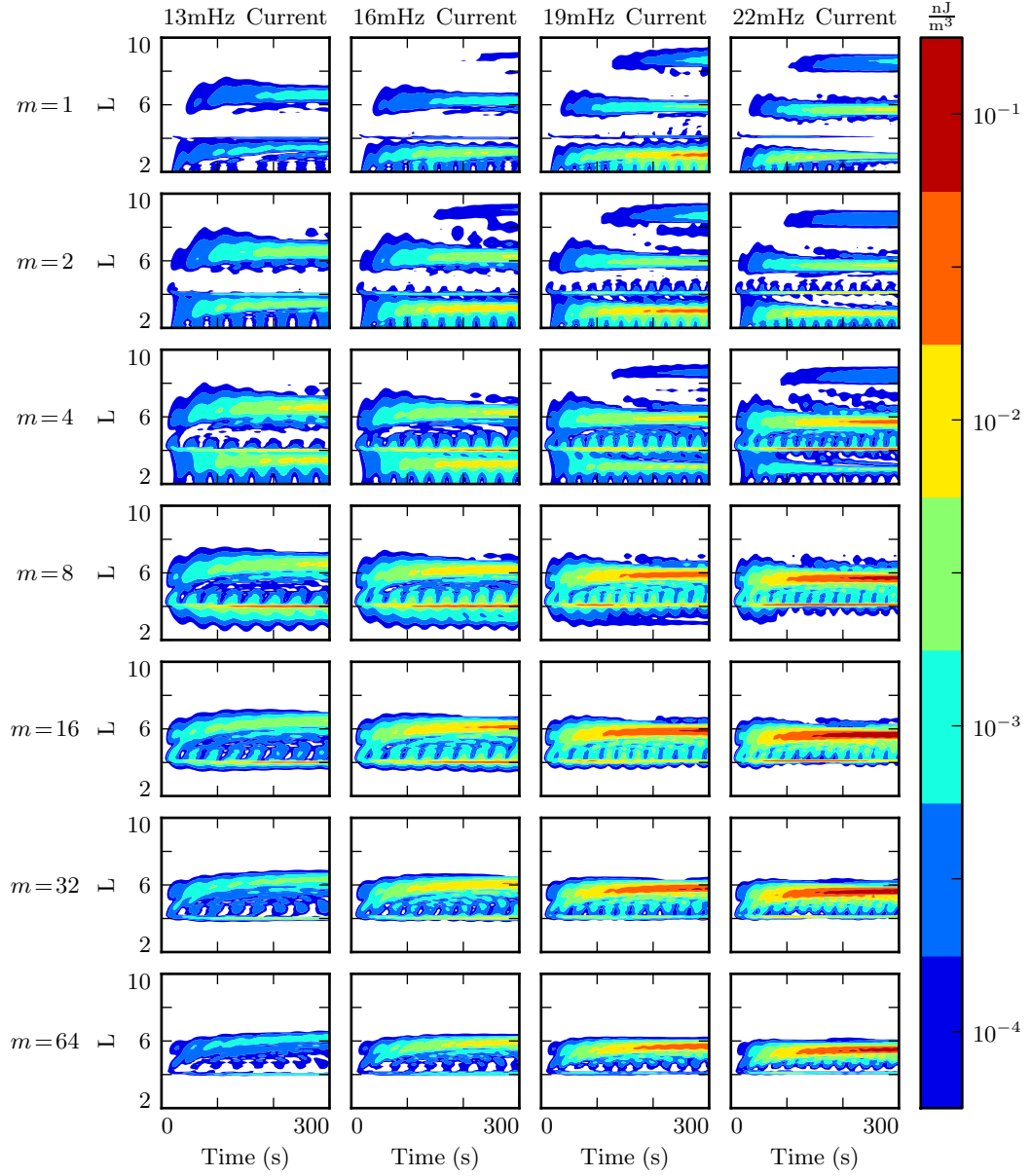


Figure 7.6: Whereas the poloidal mode is smeared in L due to its compressional nature, the toroidal mode is focused at L shells where it's resonant. In general, when the conductivity is high, the toroidal mode also exhibits a higher asymptotic energy density than the poloidal mode (Figure 7.5).

1152 **7.3 Resonance and Rotation on the Nightside**

- 1153 Compared to the dayside ionosphere employed in Section 7.2, conductivity on the night-
1154 side is much lower. Runs in the present section use Tuna’s ionospheric profile corre-
1155 sponding to the nightside during quiet solar conditions. The two nightside profiles are
1156 briefly compared in Section 7.4, but for the most part the present work is concerned
1157 with the behavior of the nightside compared to that on the dayside.
- 1158 Other than the change in ionospheric profile, Figures 7.7 to 7.9 are analogous to Fig-
1159 ures 7.4 to 7.6. Each subplot corresponds to a different 300s run of Tuna. Drive
1160 frequency is constant down each column, and azimuthal modenumber is constant across
1161 each row.
- 1162 The low conductivity on the nightside gives rise to strong Joule dissipation. Waves are
1163 damped out in just a few bounces, so asymptotic energy values are reached quickly.
1164 No combination of frequency and modenumber gives rise to the accumulation of energy
1165 over multiple drive periods.
- 1166 As on the dayside, rotation of energy from the poloidal to toroidal mode is fastest at
1167 $m \sim 4$. Unlike the dayside, however, dissipation on the nightside is fast compared to
1168 the rotation of energy to the toroidal mode. Toroidal energy does not asymptotically
1169 exceed the poloidal energy by a significant margin in any run shown in Figure 7.7. At
1170 $m = 64$, where the rotation timescale is slowest, no more than 10% of the energy in the
1171 poloidal mode rotates to the toroidal mode before being lost.
- 1172 Also similar to the dayside, low- m runs driven at 19 mHz and 22 mHz resonate very
1173 close to the outer boundary. As before, the buildup of energy is likely nonphysical.
- 1174 Poloidal contours on the nightside (Figure 7.8) are weaker than those on the dayside,
1175 and build up energy over less time, but otherwise similar. At low modenumber, poloidal
1176 energy propagates across L -shells, preventing the significant accumulation of energy
1177 anywhere. As the modenumber increases, energy is contained near the driving at $L \sim 5$.
1178 The strongest response is seen at 13 mHz on the bottom row, where the modenumber is
1179 at its largest and the frequency matches closest with the local eigenfrequency. Even in

1180 that case, dissipation timescales are comparable to the oscillation period, so the wave
1181 only persists in the presence of continuous driving.

1182 Toroidal energy contours on the nightside exhibit significantly different behavior from
1183 those on the dayside.

1184 At low modenumber, the nightside toroidal mode (Figure 7.9) contains less energy
1185 than on the dayside, but it still shows some preference for sharp resonances where the
1186 drive frequency matches the local Alfvén frequency. At moderate modenumbers, as on
1187 the dayside, the toroidal mode is more or less comparable in strength to its poloidal
1188 counterpart. It's only at high modenumber that the difference between the dayside
1189 and nightside toroidal contours become truly dramatic. Whereas on the dayside, most
1190 energy is asymptotically deposited in the toroidal mode, on the nightside most poloidal
1191 energy is dissipated faster than the poloidal-to-toroidal rotation timescale. At $m = 64$,
1192 where the poloidal mode is at its strongest, the toroidal mode is at its weakest; it barely
1193 registers, even on Figure 7.9's log scale.

Poloidal (Blue) and Toroidal (Red) Energy: Quiet Night

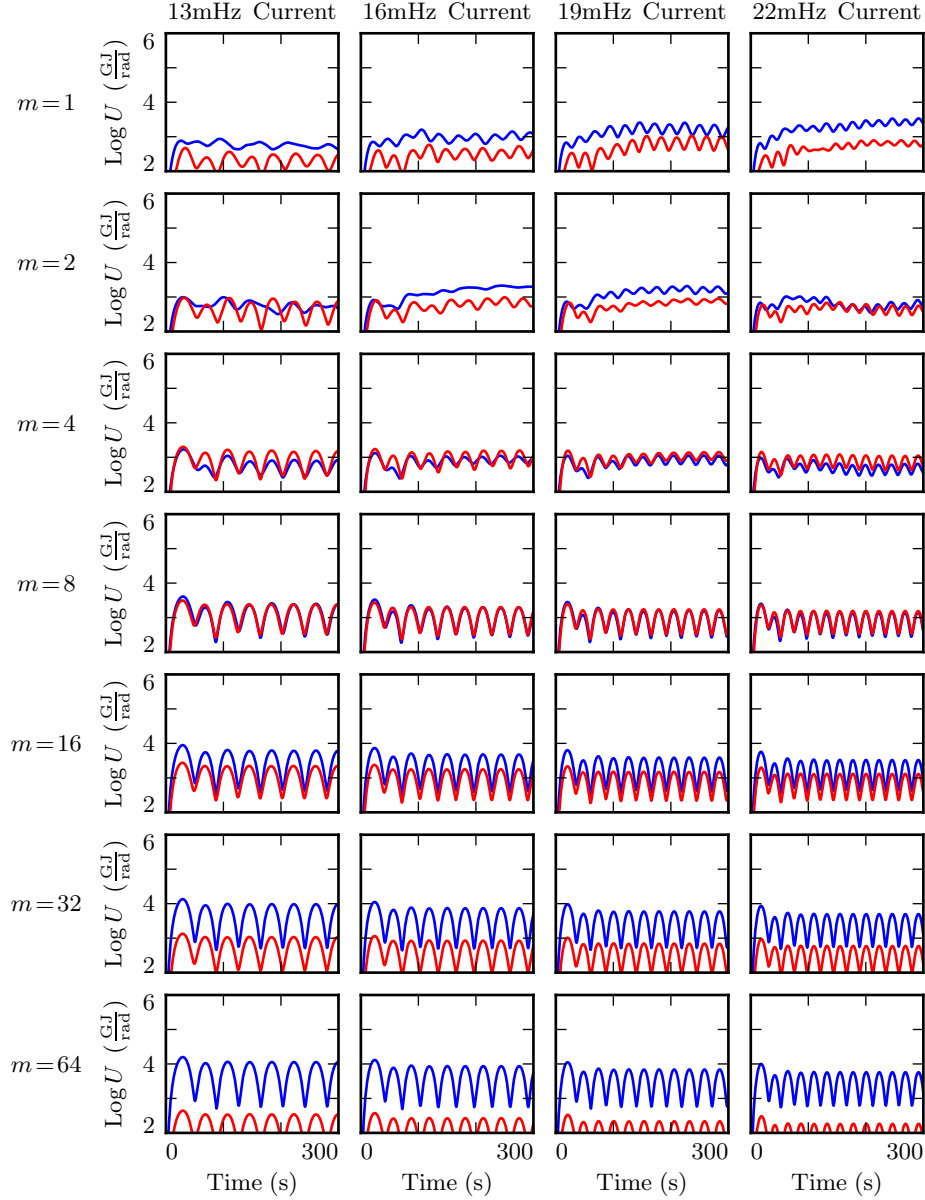


Figure 7.7: The energy content of each FLR on the nightside resembles that of a damped, driven oscillator. Energy is periodically added to the system, but most is lost too fast to rotate to the toroidal mode, particularly at high modenumber. There is no significant buildup of energy over multiple periods. Runs at $m = 1$ (top row) are an apparent exception, likely due to a nonphysical interaction with the boundary.

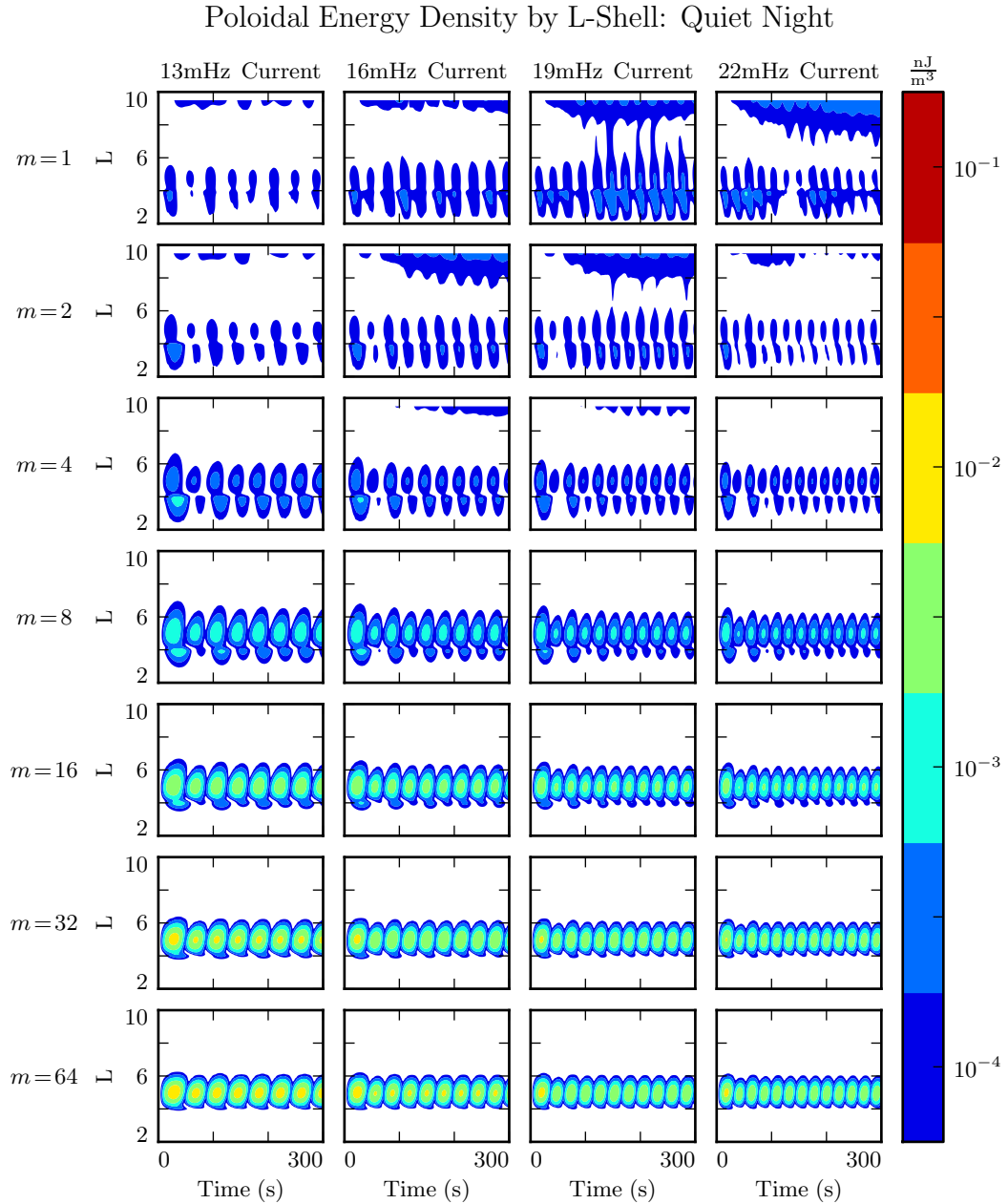


Figure 7.8: As on the dayside (Figure 7.5), low-modenumber poloidal waves (top rows) readily propagate across L -shells and escape the simulation domain. Energy density builds up most effectively at high modenumbers, where the poloidal mode is guided, and poloidal-to-toroidal rotation is slow. Even in this case, however, dissipation is fast enough to prevent energy from accumulating over multiple drive periods.

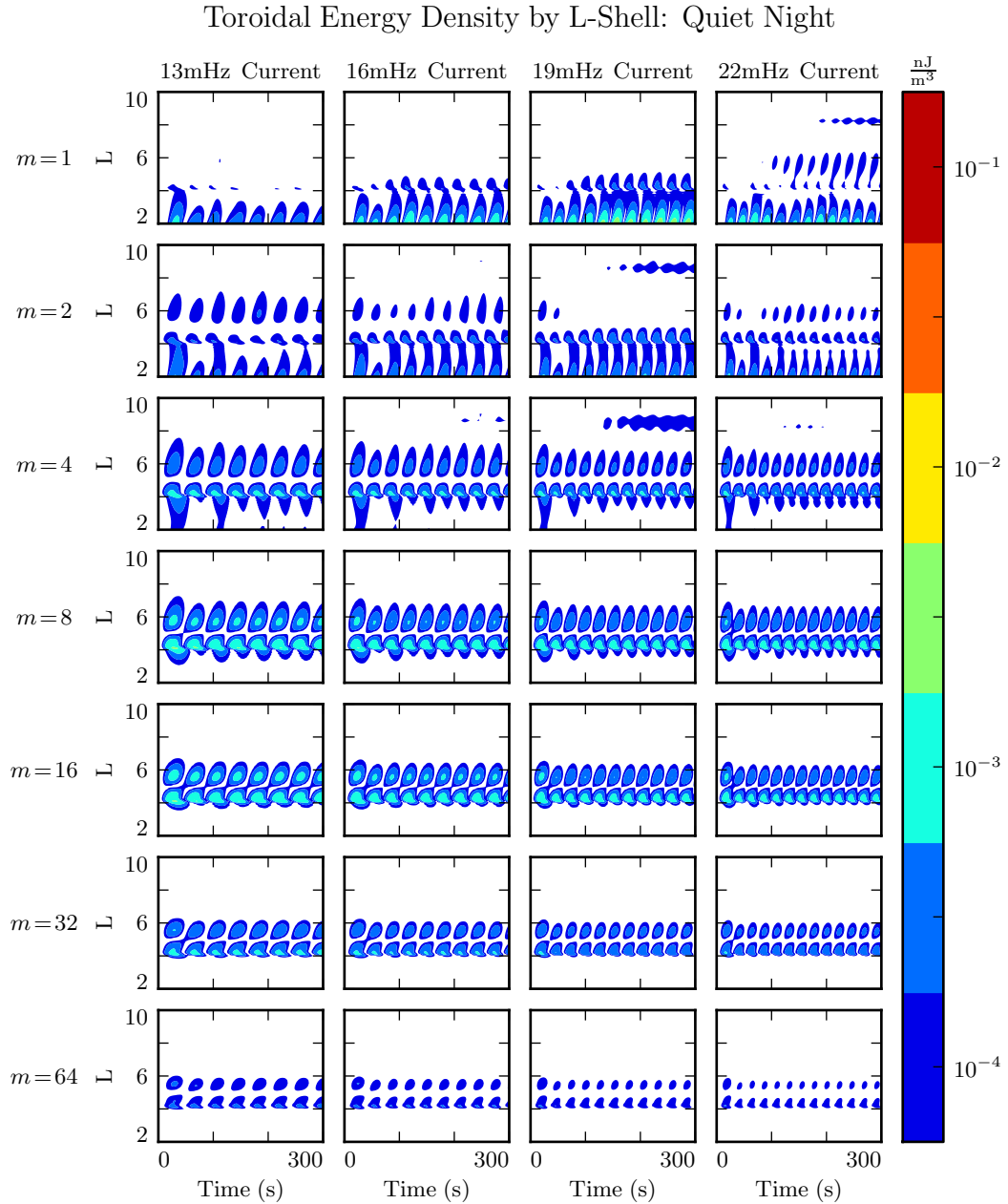


Figure 7.9: On the dayside (Figure 7.6), most energy rotates asymptotically to the toroidal mode. On the night side, the same is not true, since the poloidal mode quickly loses energy to Joule dissipation. At high modenumber, where the poloidal-to-toroidal rotation timescale is in the tens of wave periods, almost all of the energy is dissipated from the poloidal mode rather than rotating to the toroidal mode.

1194 7.4 Ground Signatures and Giant Pulsations

1195 While the majority of the action is in space, the majority of FLR observations have
1196 historically been ground-based. The present section explores simulations (including
1197 those discussed in Sections 7.2 and 7.3) in terms of their ground signatures rather than
1198 their integrated energy distributions.

1199 Figures 7.10 and 7.11 show fourteen runs each, two per row. Contours give magnetic
1200 fields at the ground, plotted against time on the horizontal axis and latitude on the
1201 vertical axis. Modenumber is held constant across each row, as in the above sections;
1202 columns show north-south and east-west ground signatures using an ionospheric profile
1203 for active (first and second columns respectively) and quiet (third and fourth columns).

1204 As noted in Chapter 3, the magnetic polarization of a low frequency Alfvén wave is
1205 rotated by $\sim 90^\circ$ as it passes through the ionosphere. The east-west field on the ground
1206 (B_ϕ) corresponds to the poloidal polarization in space, and the north-south field on the
1207 ground (B_θ) corresponds to the toroidal mode.

1208 The most striking feature of Figures 7.10 and 7.11 is the modenumber dependence.
1209 As modenumber increases, the magnetic field signatures become sharply localized in
1210 latitude. At high m , ground signatures are concentrated between 60° and 70° , peaking
1211 near 64° , roughly coincident with the foot point of the $L = 5$ field line; ionospheric
1212 ducting is not significant in the Pc4 regime.

1213 At low modenumber, magnetic signatures are weak on the ground because the waves
1214 in space are also weak. At high modenumber, waves in space are strong, but so is the
1215 attenuation of magnetic signatures by the atmosphere³. The “sweet spot” at which
1216 magnetic ground signatures are maximized falls at $m = 16$ to $m = 32$.

1217 Tuna shows stronger ground signatures on the dayside than on the nightside, more or
1218 less in proportion with the difference in magnitude in space. Energy on the dayside
1219 (which depends on field magnitude squared) peaks an order of magnitude larger than
1220 that on the nightside. Peak ground signatures on the dayside are larger by a factor of
1221 four: 45 nT compared to 11 nT. On both the dayside and the nightside, peak ground

³See Equation (3.3).

1222 signatures are in B_ϕ , the east-west magnetic field component; both peaks are also at
1223 $m = 16$, and both are seen in runs using the ionospheric profile for quiet solar activity.

1224 It's further notable that the ground signatures — particularly those on the nightside
1225 — exhibit a change in chirality based on latitude. At low latitude, B_θ leads B_ϕ , which
1226 creates a counterclockwise signature on the ground (in the northern hemisphere). At
1227 high latitude, the phase is reversed, resulting in a clockwise ground signature.

1228 These results match well with the properties associated with Pgs: east-west polarization
1229 — latitude-dependent chirality, peak latitude of $\sim 66^\circ$, and azimuthal modenumber
1230 of 16 to 35. Just about the only properties missing are the azimuthal drift (which is
1231 beyond the scope of the present model) and the distribution in MLT. Pgs are most
1232 commonly observed pre-dawn, but morning and evening ionospheric profiles are not
1233 presently implemented for Tuna.

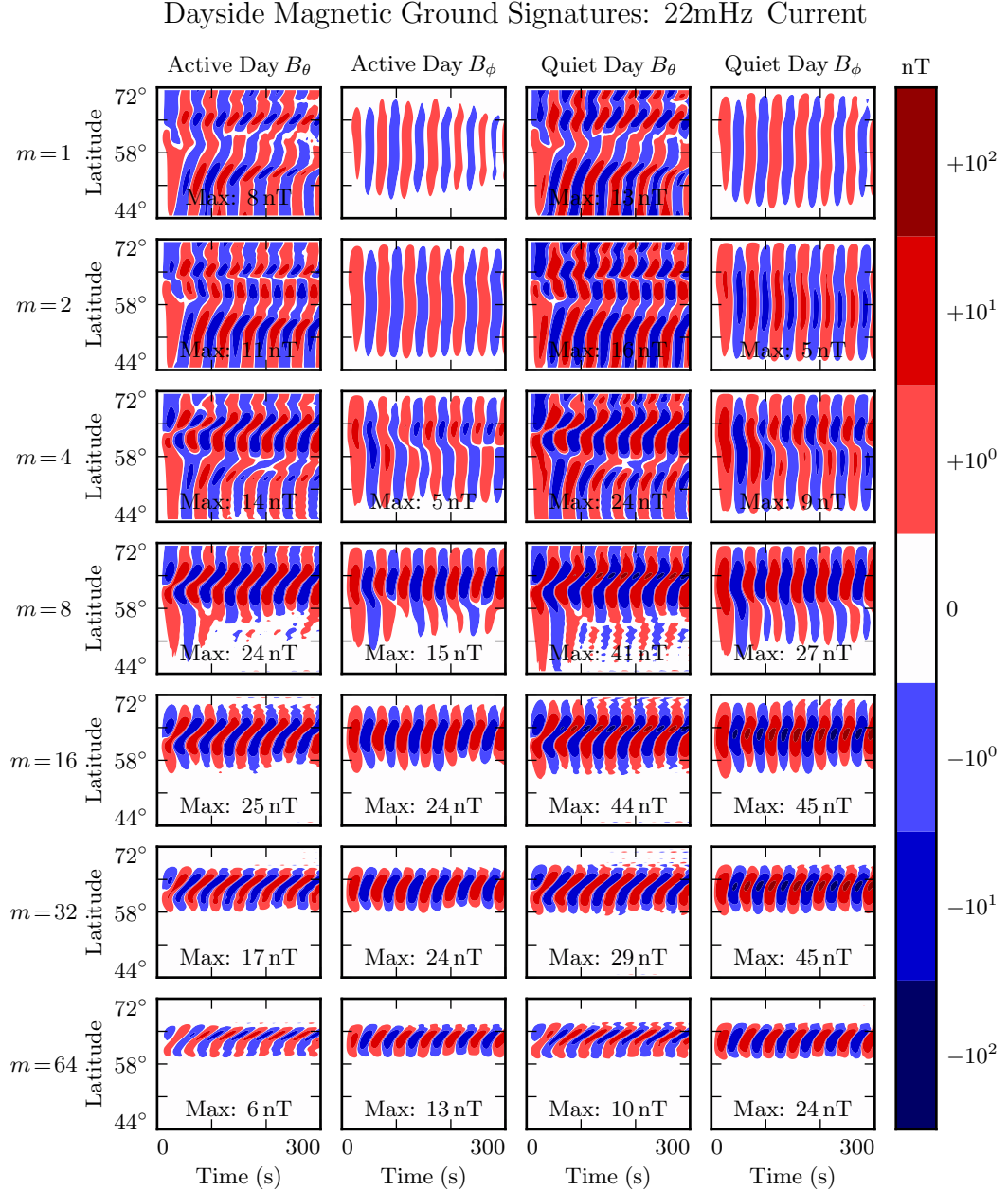


Figure 7.10: The magnetic ground signatures are shown for fourteen runs, two per row. Azimuthal modenumber is constant across each row. Polarization and ionospheric profile vary by column, per the headers. Ground signatures at low modenumber are weak because the waves in space are weak, while those at high modenumber are attenuated by the atmosphere. Considering both effects, ground signatures seem to be maximized at $m = 16$ to $m = 32$. Peak amplitudes above 3 nT are marked.

Nightside Magnetic Ground Signatures: 13mHz Current

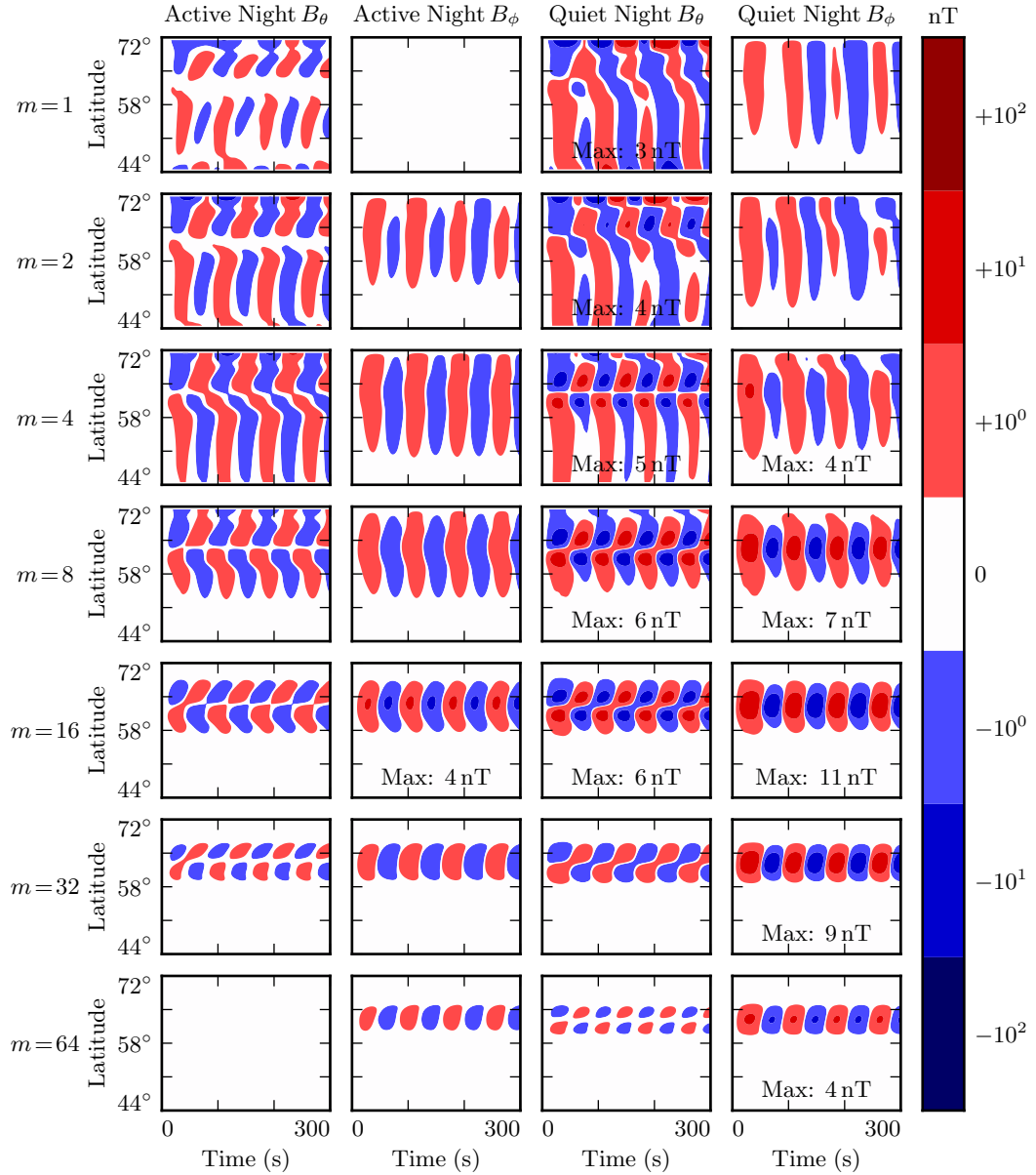


Figure 7.11: Nightside ground signatures are less strongly peaked than those on the dayside, but qualitative features are the same: the strongest signals are in B_ϕ , peaked over just a few degrees in latitude, at a modenumber of 16 or 32, under quiet ionospheric conditions.

1234 **7.5 Discussion**

1235 The above results show agreement with a number of past FLR studies. In addition,
1236 several novel connections are suggested between known properties of FLRs.

1237 The compressibility of poloidal FLRs at low modenumber, but not high modenumber,
1238 is reproduced and quantified. At $m \sim 1$, the poloidal and compressional components of
1239 an FLR in the Pc4 range are comparable in magnitude. At $m \gtrsim 6$, $\left| \frac{B_z}{B_x} \right| \lesssim \frac{1}{2}$, and at
1240 $m \gtrsim 12$, $\left| \frac{B_z}{B_x} \right| \lesssim \frac{1}{4}$.

1241 The present results also suggest that compressional character of poloidal Pc4s is to blame
1242 for the weak relationship between L and frequency, compared to that seen in toroidal
1243 events. Toroidal resonances are defined sharply in L regardless of modenumber, while
1244 poloidal resonances are smeared in L — particularly at low m , but to some degree at
1245 high m as well.

1246 The asymptotic rotation of energy from the poloidal mode to the toroidal mode is
1247 reproduced; at small m , the rotation timescale is comparable to a wave period, while
1248 at large modenumber it's on the order of 10 periods. On the dayside, little energy
1249 is lost to Joule dissipation on rotation timescales, suggesting that the poloidal mode
1250 is a significant source of energy for same-harmonic toroidal waves. On the nightside,
1251 dissipation timescales are comparable to wave periods, suggesting that the poloidal
1252 mode gives rise to toroidal waves less effectively.

1253 Ground signatures at low modenumber are shown to be weak because waves in space are
1254 weak; this is particularly true for poloidal waves — a non-guided wave can't very well
1255 resonate along a field line — but also true of toroidal waves insomuch as poloidal waves
1256 are their source. FLRs resonate most strongly at high m , but high- m signatures are
1257 also attenuated by the atmosphere. The balance between the two effects falls around m
1258 of 16 to 32. It's further suggested that a high- m driver will cause a weak resonance in
1259 place rather than tunneling across field lines to a matching eigenfrequency, and that the
1260 same driving should give rise to stronger ground signatures during times of low solar
1261 activity, on both the dayside and the nightside.

1262 The findings together suggest, awkwardly, that the morphology of giant pulsations re-
1263 veals relatively little about their origins.

1264 One can consider a hypothetical magnetosphere subject to constant driving: broadband
1265 in frequency, broadband in modenumber, just outside the plasmapause. Low- m poloidal
1266 waves will quickly rotate to the toroidal mode (and/or propagate away). High- m waves
1267 will resonate in place, accumulating energy over time, and giving rise to “multiharmonic
1268 toroidal waves”[87]; Fourier components that do not match the local eigenfrequency
1269 will accumulate energy over just a few wave periods before reaching asymptotic values.
1270 Waves with very high modenumbers will be attenuated by the ionosphere. The response
1271 on the ground will be counterclockwise at low latitude, clockwise at high latitude, peaked
1272 at $16 \lesssim m \lesssim 32$, mostly east-west polarized, and notably stronger during quiet solar
1273 conditions. In other words, the measurements will look very much like a giant pulsation.

1274 The present results offer no explanation as to the tendency of giant pulsations to drift
1275 azimuthally, or to appear pre-dawn in MLT — though the latter is addressed by the
1276 observational results in Chapter 8.

₁₂₇₇ **Chapter 8**

₁₂₇₈ **Van Allen Probe Observations**

₁₂₇₉ The results presented in Chapter 7 are interesting on their own, but become particularly
₁₂₈₀ valuable when combined with observational data. Unfortunately, only a small number
₁₂₈₁ of studies to date have explored how Pc4 observation rate is affected by the harmonic
₁₂₈₂ and polarization structure of those waves. While Pc4 pulsations have previously been
₁₂₈₃ studied in terms of both harmonic[4, 14, 26, 43, 81, 90] and polarization[2, 16, 17, 52, 56],
₁₂₈₄ no past survey has characterized each event in terms of both properties.

₁₂₈₅ This has largely been due to observational constraints. The classification of a wave's
₁₂₈₆ harmonic is best carried out by computing the phase offset of the magnetic and electric
₁₂₈₇ field waveforms, simultaneous in situ measurements of which have only recently become
₁₂₈₈ available since the launch of THEMIS[3] in 2007 and the Van Allen Probes[84] in 2012.
₁₂₈₉ The Van Allen Probes are particularly well-suited to the study of Pc4 pulsations as
₁₂₉₀ their apogee of $L \sim 6$ coincides closely with eigenfrequencies in the Pc4 range.

₁₂₉₁ The present chapter uses data from the Van Allen Probes mission to survey the oc-
₁₂₉₂ currence rate of FLRs in the Pc4 range as a function of parity and polarization, as
₁₂₉₃ well as magnitude, frequency, and phase. The tools used to perform the present anal-
₁₂₉₄ ysis — SPEDAS and the SPICE kernel — are publicly available. They, along with
₁₂₉₅ the Python routines used to download, filter, and plot the data, can be found at
₁₂₉₆ <https://github.com/UMN-Space-Physics>.

1297 8.1 Sampling Bias and Event Selection

1298 The present analysis makes use of Van Allen Probe data from October 2012 to August
1299 2015 — the entire range available at the time of writing. Between the two probes, that's
1300 just over 2000 days of observation.

1301 For the purposes of the present work, the two probes are taken to be independent
1302 observers. A preliminary estimate shows that Pc4 events are sufficiently narrow in
1303 MLT that they are rarely ($\sim 1\%$) seen by both probes simultaneously. The events are
1304 also short-lived enough that they are rarely seen by the two probes passing through the
1305 same region of space, no more than a few hours apart. That said, a future investigation
1306 into the few events that are seen by both probes could offer significant insight into the
1307 structure and behavior of these waves.

1308 Electric and magnetic field data are collected using the probes' EFW[100] and EMFISIS
1309 instruments respectively. Level 3 values are used, averaged over the ten-second probe
1310 spin period¹. Three-dimensional electric field data is obtained by using the $\underline{E} \cdot \underline{B} = 0$
1311 assumption; at such low frequencies, this is more accurate than measurements taken
1312 using the spin-axis boom. Notably, this assumption is taken only when the probe's spin
1313 plane is offset from the magnetic field by at least 15° . The rest of the data — about
1314 half — is discarded, potentially introducing a sampling bias in MLT.

1315 A further bias is introduced by the probes' non-integer number of precessions around
1316 Earth. As of July 2014, apogee had completed one full precession[16]. The present work
1317 considers roughly one and a half precessions; the nightside has been sampled at apogee
1318 twice as often as the dayside.

1319 The spatial distribution of usable data — that is, data for which three-dimensional elec-
1320 tric and magnetic fields are available at the desired accuracy — is shown in Figure 8.1.
1321 Bins are unitary in L and in MLT. The distribution of the data in magnetic latitude is
1322 not shown; the Van Allen Probes are usually localized to within 10° of the equatorial
1323 plane.

1324¹The fastest Pc4 pulsations have periods of 45 s, so a ten-second measurement cadence easily satisfies
the Nyquist rate.

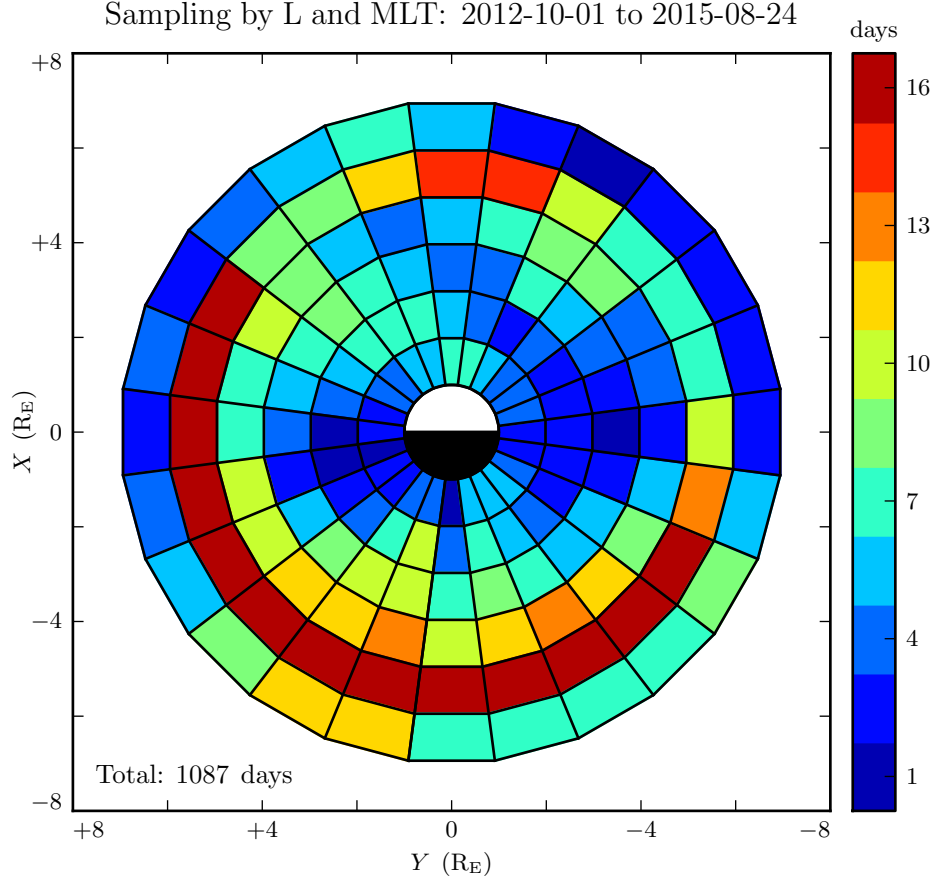


Figure 8.1: The above figure shows the spatial distribution of sampling by the Van Allen Probes. Bins are unitary in the polar coordinates L and MLT; the spatial scale is indicated by the SM X and Y axes. The Van Allen Probes have precessed one and a half times around Earth, so the nightside has been double-sampled at apogee, resulting in a significant sampling bias.

1324 Field measurements are transformed into the same dipole coordinates used in Chapters 5
 1325 and 7. The background magnetic field is estimated using a ten-minute running average
 1326 of the magnetic field measurements; that defines the z axis. The y axis is set parallel
 1327 to $\hat{z} \times \underline{r}$, where \underline{r} is the probe's geocentric position vector. The x axis is then defined
 1328 per $\hat{x} \equiv \hat{y} \times \hat{z}$. This scheme guarantees that the axes are right-handed and pairwise
 1329 orthogonal[56].

1330 The \sim 1000 days of usable data are considered half an hour at a time, which gives a fre-
 1331 quency resolution of \sim 0.5 mHz in the discrete Fourier transform. Spectra are computed
 1332 for all six field components: \tilde{B}_x , \tilde{B}_y , \tilde{B}_z , \tilde{E}_x , \tilde{E}_y , and \tilde{E}_z . The background magnetic
 1333 field is subtracted before transforming the magnetic field components, leaving only the
 1334 perturbation along each axis². Each waveform is also shifted vertically so that its mean
 1335 over the thirty minute event is zero.

Poynting flux along the field is computed from the electric and magnetic field transforms.
 A factor of $\left(\frac{r}{R_I}\right)^3$ compensates the compression of the flux tube, so that the resulting
 values are effective at the ionosphere. Poloidal and toroidal Poynting flux, respectively,
 are given by:

$$\tilde{S}_P \equiv -\left(\frac{r}{R_I}\right)^3 \frac{1}{\mu_0} \tilde{E}_y \tilde{B}_x^* \quad \tilde{S}_T \equiv \left(\frac{r}{R_I}\right)^3 \frac{1}{\mu_0} \tilde{E}_x \tilde{B}_y^* \quad (8.1)$$

1336 An example event — both electric and magnetic field measurements and real and imag-
 1337 inary Poynting flux spectra — is shown in Figure 8.2.

1338 The poloidal and toroidal channels are independently checked for Pc4 waves. For each
 1339 channel, a Gaussian profile is fit to the magnitude of the Poynting flux, $|\tilde{S}(\omega)|$. If the
 1340 fit fails to converge, or if the peak of the Gaussian does not fall within 5 mHz of the
 1341 peak value of \tilde{S} , the event is discarded. Events are also discarded if their frequencies
 1342 fall outside the Pc4 frequency range (7 mHz to 25 mHz) or if their amplitudes fall below
 1343 0.005 mW/m² (out of consideration for instrument sensitivity).

1344 The magnitude threshold is set in Poynting flux instead of magnetic field (which is more
 1345 typical) in an effort to reduce bias in event selection. When events are selected based on
 1346 the magnitude of the wave magnetic field, odd waves become more difficult to detect,
 1347 due to their magnetic field node at the equator. In fact, Dai et al mention explicitly
 1348 in their 2015 survey that the magnetic field threshold is meant to preferentially select
 1349 even events[16].

²As in Chapters 4 to 7, B_x , refers not to the full magnetic field in the x direction, but to the perturbation in the x direction from the zeroth-order magnetic field. The same is true for B_y and B_z .

1350 Events are discarded if their parity is ambiguous. The electric field and the magnetic
1351 field must be coherent at a level of 0.9 or better (judged at the discrete Fourier transform
1352 point closest to the peak of the Gaussian fit). Any event within 3° of the magnetic
1353 equator is also not used; as discussed in Chapter 3, in order to distinguish an odd mode
1354 from an even mode, it's necessary to know whether the observation is made north or
1355 south of the equator.

1356 A visual inspection of events shows that those with broad “peaks” in their spectra are
1357 typically not peaked at all — that are bad fits of noisy or multiharmonic data. A
1358 threshold is set at a FWHM of 3 mHz (equally, a standard deviation of 1.27 mHz). Any
1359 event with a Gaussian fit broader than that is discarded.

1360 Notably, events are not filtered on their phase — that is, on the division of their energy
1361 between standing and traveling waves. This is the topic of Section 8.5.

Waveforms and Spectra: Even Toroidal Wave

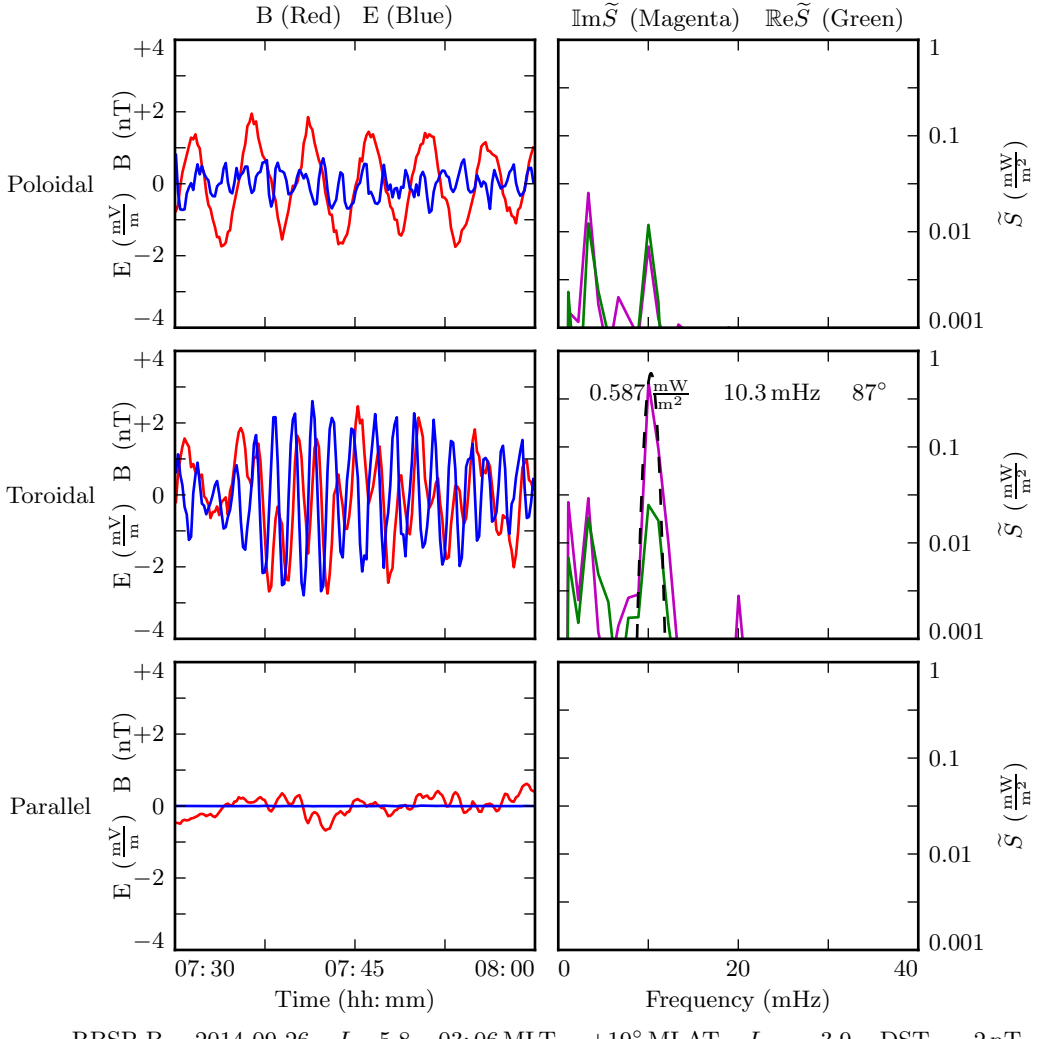


Figure 8.2: An example half-hour event is shown. On the left, components of the electric and magnetic field measurements are shown. On the right are the real and imaginary components of the corresponding Poynting flux spectra. A ~ 3 mHz magnetic oscillation is visible in the poloidal channel, as is an electric field oscillation at ~ 10 mHz; peaks appear at both frequencies in the corresponding spectrum, but no poloidal event is selected because the oscillations are not coherent. In the toroidal channel, a clear standing wave (phase of 87°) is evident at 10.3 mHz. The black dotted line shows a Gaussian fit of the Poynting flux magnitude.

1362 8.2 Events by Mode

1363 The filters described in Section 8.1 yield 451 half-hour Pc4 events, the spatial distribution
1364 of which is shown in Figure 8.3. In each bin, the event count is normalized to the amount of usable data (Figure 8.1). Bins shown in white contain zero events. The rate
1366 in the bottom corner is an overall mean; it's an estimate of how often Pc4 events would
1367 be observed if the sampling were distributed uniformly in space.

1368 Consistent with previous work[2, 16, 52, 56], Pc4 events peak on the dayside and are
1369 rarely observed at $L < 4$. Nearly 30 % of the usable data shown in Figure 8.1 is taken at $L < 4$, yet only 13 of the 451 events (3 %) appear there.

1371 On the other hand, the present work runs contrary to recent results by Dai et al in terms of Pc4 event rates with respect to the plasmapause (not shown). Their analysis found (poloidal) Pc4 pulsations to be comparably common inside and outside the plasmapause[16]. In the present work, only 1374 TODO: 40 of the 451 events 1375 TODO: (5 %) fall inside the plasmasphere, despite the fact that 40 % of the available data falls within the plasmasphere. It's possible that the discrepancy is due to differing definitions of the location of the plasmapause; Dai et al identify the plasmapause by the maximum gradient in electron number density, while the present work takes an electron density of 100 /cm^3 to mark the plasmapause³. Event selection criteria also vary significantly between the present survey and that conducted by Dai et al — their work shows poloidal events located based on high-cadence magnetic field data only, while the present work also considers toroidal waves and electric fields, but at lower cadence.

1383 The same events in Figure 8.3 are shown again in Figure 8.4, partitioned by polarization and parity. In an effort to mitigate the effects of small number statistics, the bins in Figure 8.4 span two hours each in MLT and do not break at all in L . These same large bins are used in Sections 8.3 to 8.5.

1387 The distribution of even poloidal events in Figure 8.4 is consistent with that reported by Dai et al[16]: the observation rate is peaked at noon, and extends across the dusk side. Notably, Dai et al focused on even poloidal waves. While they did not explicitly

3Per ongoing work by Thaller.

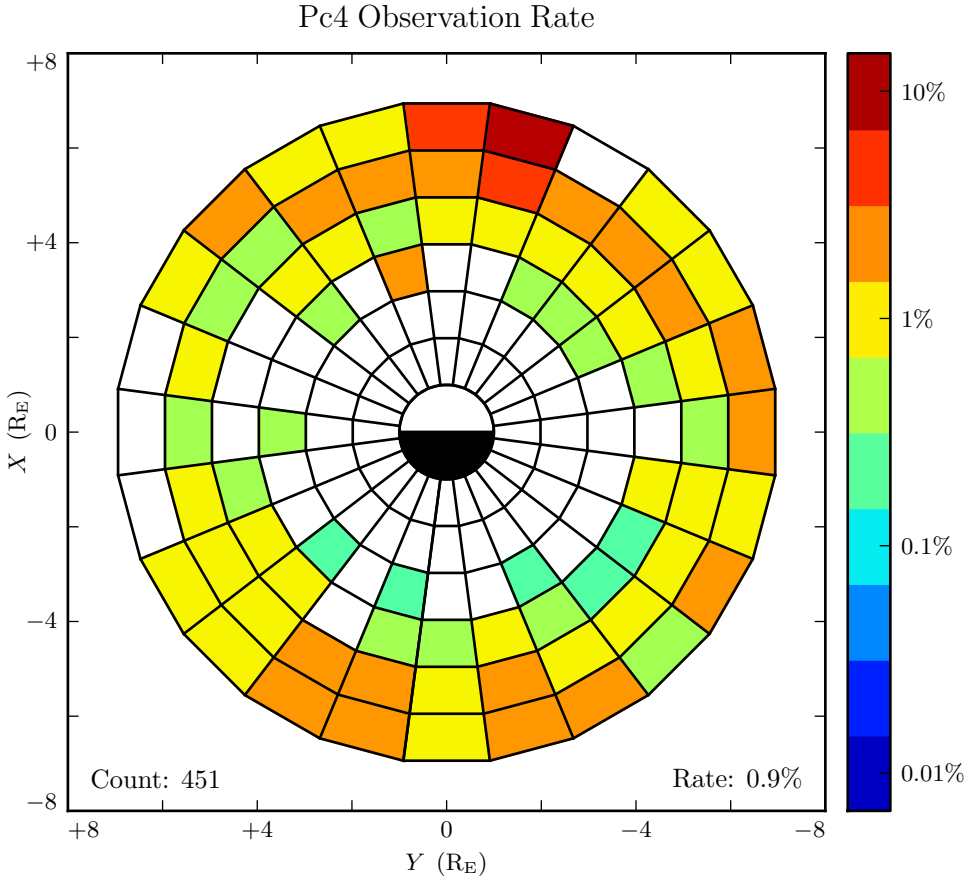


Figure 8.3: The above figure shows the spatial distribution of all 451 observed Pc4 events. Counts are normalized by the amount of usable data in each bin. The value in the bottom-right corner is the mean of the rate in each bin, with the rate in each bin weighed by the area of that bin. Events where the poloidal and toroidal channel both trigger ($\sim 10\%$ of events) are counted as only a single event. Bins shown in white contain zero events.

remove odd events from the sample, they did introduce a threshold in the magnetic field. This threshold is preferentially satisfied by even waves (which have a magnetic field antinode near the equator) compared to odd waves (which have a magnetic field node). Dai et al characterized the parity of only a quarter of his events; among those, they found even harmonics to outnumber odd harmonics ten-to-one.

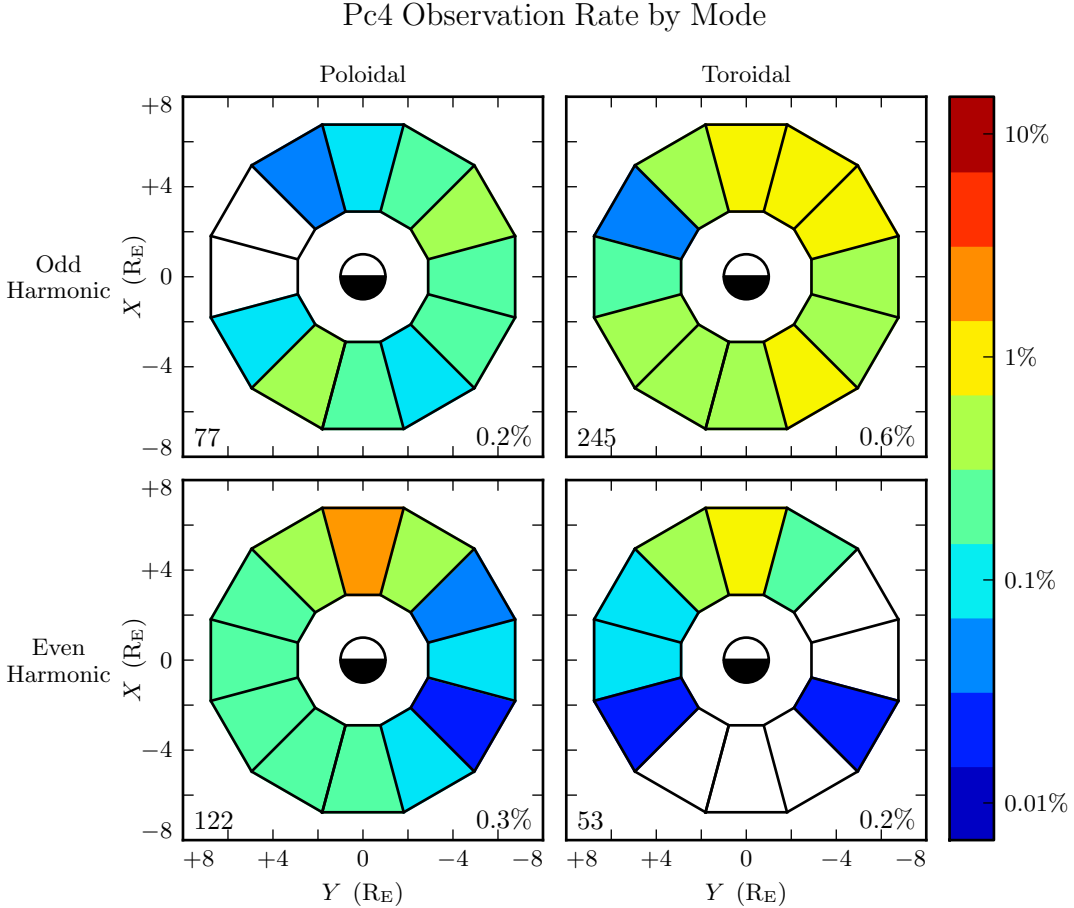


Figure 8.4: The above figure shows the spatial distribution for the same 451 events shown in Figure 8.3, partitioned by polarization and parity. The selection criteria described in Section 8.1 ensure that both properties are known for all events. Event counts are normalized by the time spent by the amount of usable data in each bin. Counts shown in the bottom-left corners do not sum to 451 because some events trigger on both the poloidal channel and the toroidal channel.

1395 In fact — to the degree that they can be straightforwardly compared — the distributions
 1396 in Figure 8.4 also show agreement with work by Anderson et al[2] (using AMPTE/CCE),
 1397 Kokubun et al[52] (using ATS6), Liu et al[56] (using THEMIS), and Motoba at al[69]
 1398 (using GOES). Toroidal events dominate overall, and are primarily seen on the morning

1399 side. Poloidal events are spread broadly in MLT, with a peak near noon and odd
1400 harmonics in the early morning.

1401 Crucially, the present work can offer insight into how previous results fit together. Unlike
1402 events considered in previous works, those shown in Figure 8.4 have all been categorized
1403 in terms of both polarization and parity. And, crucially, the selection process has not
1404 introduced a bias with respect to polarization or parity (at least not an obvious one).

1405 The even events shown in Figure 8.4 show good agreement with the numerical results in
1406 Chapter 7. The even poloidal and even toroidal distributions are qualitatively similar, as
1407 might be expected if even poloidal waves served as a source for even toroidal waves. Even
1408 poloidal waves are more prevalent, suggesting a typical event duration comparable to the
1409 poloidal-to-toroidal rotation timescale. And even toroidal events are skewed dayward
1410 compared to even poloidal events, consistent with numerical result that a significant
1411 amount of energy on the nightside is lost to Joule dissipation before rotating to the
1412 toroidal mode.

1413 The same can be said to some extent for the odd events in Figure 8.4, though the trends
1414 are less strong. Odd poloidal and odd toroidal events are both scarce on the dusk flank.
1415 On the dawn flank, poloidal events skew nightward, while toroidal events are spread
1416 broadly — that is, they are skewed dayward compared to the poloidal events. However,
1417 it’s unclear why odd toroidal events outnumber odd poloidal events to such a degree.

1418 When the 451 events are broken down by mode in Figure 8.4, the result is 77 odd
1419 poloidal events, 122 even poloidal events, 245 odd toroidal events, and 53 even toroidal
1420 events — a total of 497 events. The total is greater than 451 because in $\sim 10\%$ of
1421 events, the poloidal and toroidal channels trigger independently. Such cases are marked
1422 as a single event in Figure 8.3, but the toroidal and poloidal events are both shown in
1423 Figure 8.4.

1424 Double-triggering can be taken as a crude proxy for event quality. When the channels
1425 both trigger independently, the two events almost always (44 of 46 events) exhibit the
1426 same parity. This suggests a poloidal wave with sufficient power, and a sufficient narrow
1427 spectral peak, that it can still be seen after much of its energy has rotated to the toroidal
mode.

1429 Due to the small sample size of double events (20 odd and 24 even), little can be said of
1430 their spatial distribution (not shown). They are generally consistent with events overall:
1431 odd double events fall mostly on the morningside and even double events fall mostly
1432 near noon. Perhaps more notable is their pattern of occurrence. Odd double events
1433 rarely occur twice on the same date (the 20 events are distributed across 18 different
1434 dates) while even events often happen on the same date as one another (24 events on
1435 14 dates).

1436 8.3 Events by Amplitude

1437 The events shown in Figure 8.4 span two orders of magnitude in amplitude. One might
1438 reasonably be concerned that the spatial distributions presented in Section 8.2 are dom-
1439 inated by small events, while Pc4 events large enough to be noteworthy follow a different
1440 distribution entirely.

1441 The distribution of event magnitudes is presented in Figure 8.5, graded based on the
1442 peak of the Gaussian fit of each event's Poynting flux, $|\tilde{S}(\omega)|$. Mean and median
1443 values are listed for each mode. Most events are small, with Poynting flux well below
1444 0.1 mW/m^2 when mapped to the ionosphere. Only a handful of events — 3 out of 451
1445 — exceed 1 mW/m^2 .

1446 Perhaps the most notable feature of Figure 8.5 is the relative uniformity of the distri-
1447 bution of even poloidal events. If a higher magnitude threshold is imposed, as shown in
1448 Figure 8.6, the proportion of even poloidal events rises appreciably.

1449 All else being equal, one might expect the amplitude distribution of even toroidal events
1450 to mimic that of even poloidal events, since poloidal waves asymptotically rotate to
1451 toroidal waves. However, this does not seem to be the case. The mean and median
1452 magnitudes are more or less consistent across even toroidal events, odd toroidal events,
1453 and odd poloidal events, while even poloidal events are significantly larger.

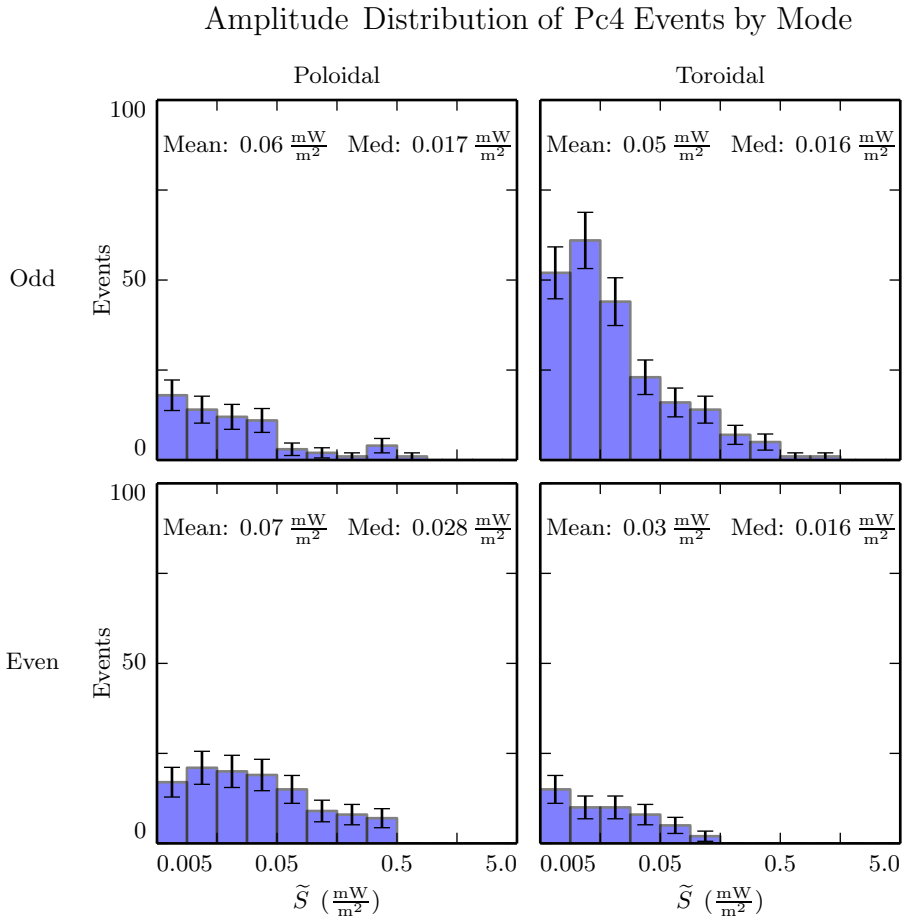


Figure 8.5: Amplitude distribution is shown for Pc4 events by parity and polarization, based on the peak of the spectrum's Gaussian fit. The amplitude distribution of even poloidal events seems to fall off less sharply than that of the other modes — the median even poloidal event is more than half again the median overall.

Distribution of Pc4 Events by Mode and Amplitude

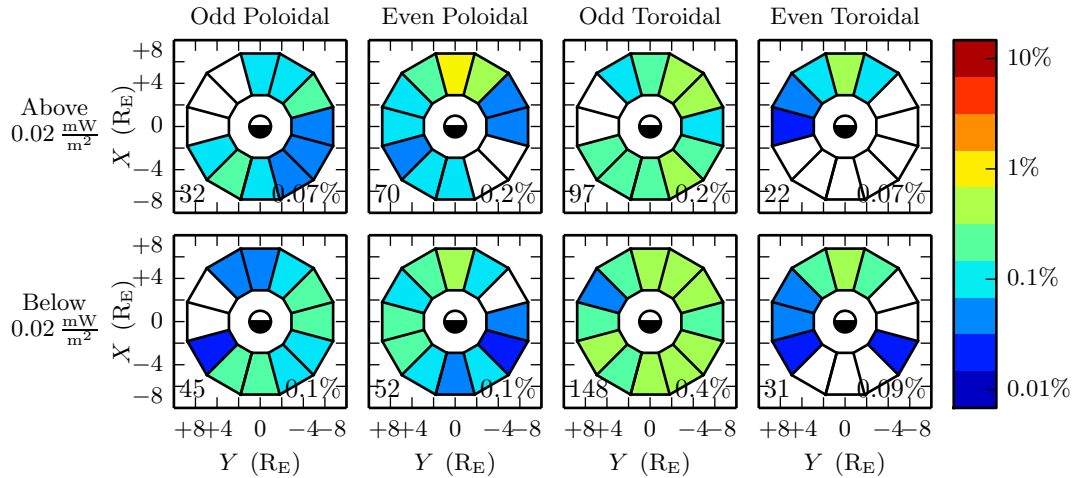


Figure 8.6: The above figure shows the distribution of Pc4 event observations by mode. Event magnitude cutoff is constant across each row. The spatial distribution for each mode does not change significantly as a function of cutoff amplitude. However, when considering only large-amplitude events, even poloidal events become proportionally more common.

1454 **8.4 Events by Frequency**

1455 The difference in magnetospheric conditions between the dayside and the nightside
1456 suggest that different eigenfrequencies should arise between dayside and nightside res-
1457 onances at the same L -shell. In fact, this phenomenon has been observed directly;
1458 the frequencies of azimuthally-drifting FLRs have been shown to change over time[69].

1459 The effect is attributed to the difference in mass loading (and thus Alfvén speed) as a
1460 function of MLT.

1461 This effect was furthermore apparent in the numerical results shown in Chapter 7, where
1462 Alfvén speeds on the dayside (based on empirical profiles) gave rise to significantly higher
1463 eigenfrequencies than those on the nightside.

1464 In Figure 8.7, events at 9 mHz to 15 mHz (center row) are shifted slightly nightward
1465 compared to those at 7 mHz to 9 mHz (top row), but the effect is far less pronounced
1466 than what is suggested by Sections 7.2 and 7.3.

1467 The frequency distribution for each mode is shown in Figure 8.8. The most distinctive
1468 feature, certainly, is the frequency peak in the odd toroidal mode near 9 mHz. This is
1469 in line with the idea that toroidal waves exhibit frequencies that depend sharply on L ,
1470 as discussed in Chapter 7. While the Van Allen Probes' orbits do cover a large range of
1471 L -shells, their observations (and thus the selected events) are concentrated near apogee
1472 at $L \sim 6$.

1473 As might be expected, Figure 8.8 also shows even events to exhibit higher frequencies
1474 overall than odd events.

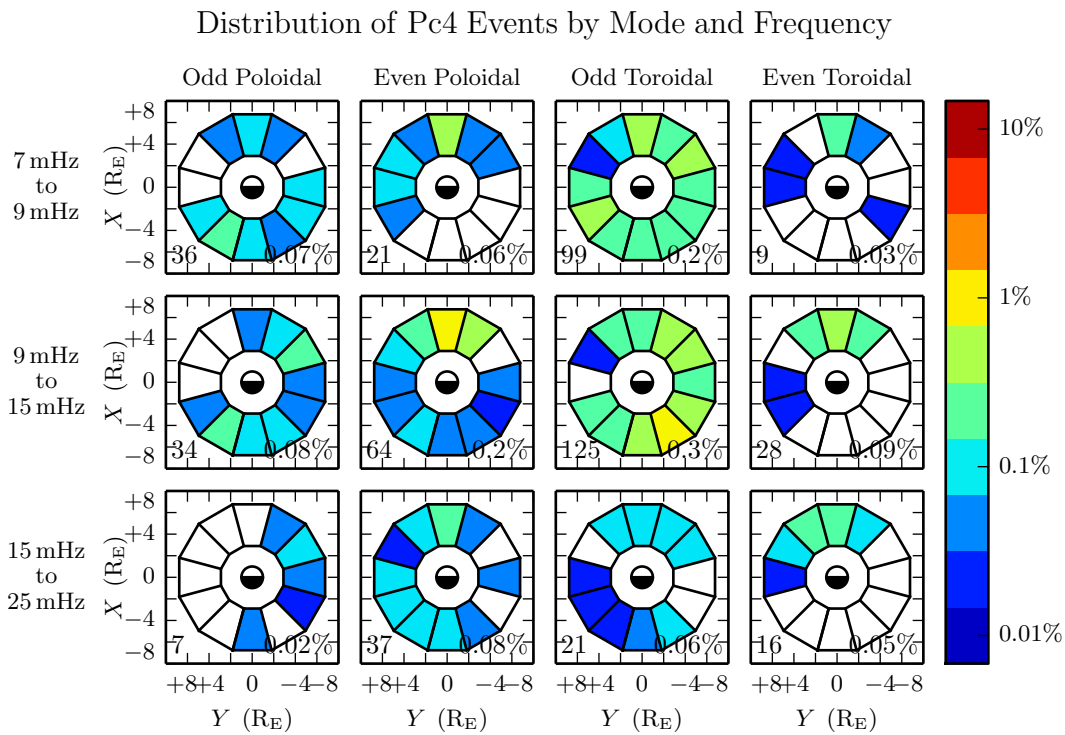


Figure 8.7: Event distributions above are shown in terms of mode (column) as well as event frequency (row). Mid-frequency Pc4 events are shifted somewhat nightward compared to low-frequency Pc4 events, as might be expected from the dayside's faster Alfvén speed.

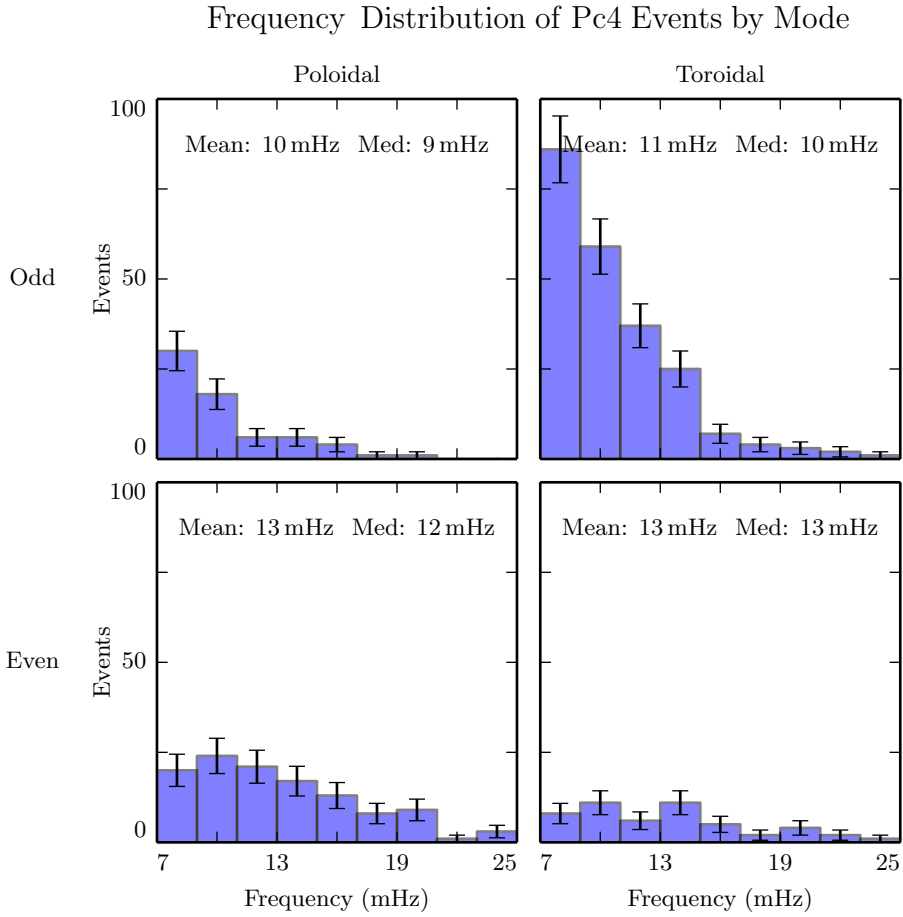


Figure 8.8: Frequency distributions are shown for all events, divided by harmonic and polarization. Odd toroidal events exhibit a particularly sharp peak in frequency, which is consistent with the toroidal mode's strong correlation with the local eigenfrequency. Poloidal modes appear more spread out in frequency, which is also consistent with past observations and with the numerical results in Chapter 7.

¹⁴⁷⁵ 8.5 Events by Phase

¹⁴⁷⁶ The phase of a wave — that is, the phase offset between a wave's electric and magnetic
¹⁴⁷⁷ fields — indicates how its energy is partitioned between the standing and traveling
¹⁴⁷⁸ wave modes. An ideal standing wave has a phase of $\pm 90^\circ$, and thus its Poynting flux is
¹⁴⁷⁹ completely imaginary. A traveling wave, on the other hand, has electric and magnetic
¹⁴⁸⁰ fields in phase (or in antiphase), and is associated with a net movement of energy,
¹⁴⁸¹ usually toward the ionosphere.

¹⁴⁸² Wave phase is a topic of significant interest, since it allows an estimate to be made of
¹⁴⁸³ the wave's lifetime. And, because phase can only be determined using simultaneous
¹⁴⁸⁴ electric and magnetic field measurements, it has only recently become observable.

The energy per unit volume, and the rate at which energy is carried out of that volume
by Poynting flux, are respectively given by:

$$U = \frac{R^3}{2\mu_0} B^2 \quad \frac{\partial}{\partial t} U = \frac{R^2}{\mu_0} EB \cos \varphi \quad (8.2)$$

¹⁴⁸⁵ Where B , E , and R are the characteristic magnetic field magnitude, electric field mag-
¹⁴⁸⁶ nitude, and length scale. The phase, $\varphi \equiv \arctan \frac{\text{Im} \tilde{S}}{\text{Re} \tilde{S}}$, enters because only real Poynting
¹⁴⁸⁷ flux carries energy.

The ratio of the two quantities in Equation (8.2) gives a characteristic timescale over
which energy leaves the system

$$\tau \equiv \frac{BR}{2E \cos \varphi} \quad (8.3)$$

¹⁴⁸⁸ In the present case, magnetic fields are on the order of 1 nT and electric fields are on
¹⁴⁸⁹ the order of 1 mV/m. A reasonable scale length might be 10^4 km, the distance traversed
¹⁴⁹⁰ by the probe over the course of a half-hour event near apogee (notably, back-to-back
¹⁴⁹¹ events are unusual).

¹⁴⁹² At a phase of 80° , this timescale is comparable to a Pc4 wave period. At 135° , where
¹⁴⁹³ energy is divided evenly between the standing and traveling wave, the timescale is just

1494 7 seconds. A wave with a phase so far from 90° would quickly vanish unless it were
1495 constantly being replenished.

1496 An example of just such an event is shown in Figure 8.9. The left column shows
1497 electric and magnetic field waveforms in blue and red respectively. The right shows
1498 the corresponding spectra: imaginary Poynting flux in magenta (corresponding to the
1499 strength of the standing wave) and real Poynting flux in green (for the traveling wave).
1500 The black line is a Gaussian fit to the magnitude of the Poynting flux.

1501 The poloidal channel shows a mostly-standing wave, with a phase of 79° . The coherent
1502 activity in the compressional magnetic field implies a low azimuthal modenumber, and
1503 thus a fast rotation of energy from the poloidal mode to the toroidal mode. It's likely
1504 the rotation of energy from the poloidal mode contributes significantly to the toroidal
1505 mode's lifetime; the toroidal wave's phase is 130° , so its energy should be carried away
1506 quickly by Poynting flux.

1507 The selection process described in Section 8.1 does not explicitly consider phase. How-
1508 ever, the discrete Fourier transform is performed over a half-hour time span. An event
1509 with a comparatively short lifetime would be unlikely to register. It's unsurprising to
1510 see the events in Figure 8.10 are tightly clustered near 90° .

1511 It's further notable in Figure 8.10 that the odd events are more spread out in phase
1512 than the even events. Near the equator, odd modes have an electric field antinode and
1513 a magnetic field node; per Equation (8.3), an odd mode's lifetime should be longer than
1514 that of an even mode with the same phase.

1515 Unlike amplitude (Section 8.3) and frequency (Section 8.4), events partitioned by phase
1516 do not exhibit appreciably different spatial distributions, as shown in Figure 8.11.

1517 Comparisons are limited by the small event counts in several of the subplots; however,
1518 coarsely speaking, events with phases of 75° and worse (left column) show spatial dis-
1519 tributions more or less in proportion with events phased 85° or better (right column).
1520 Figure 8.10 uses the absolute value of each event's phase, as does Figure 8.11.

Waveforms and Spectra: Odd Poloidal Wave and Odd Toroidal Wave

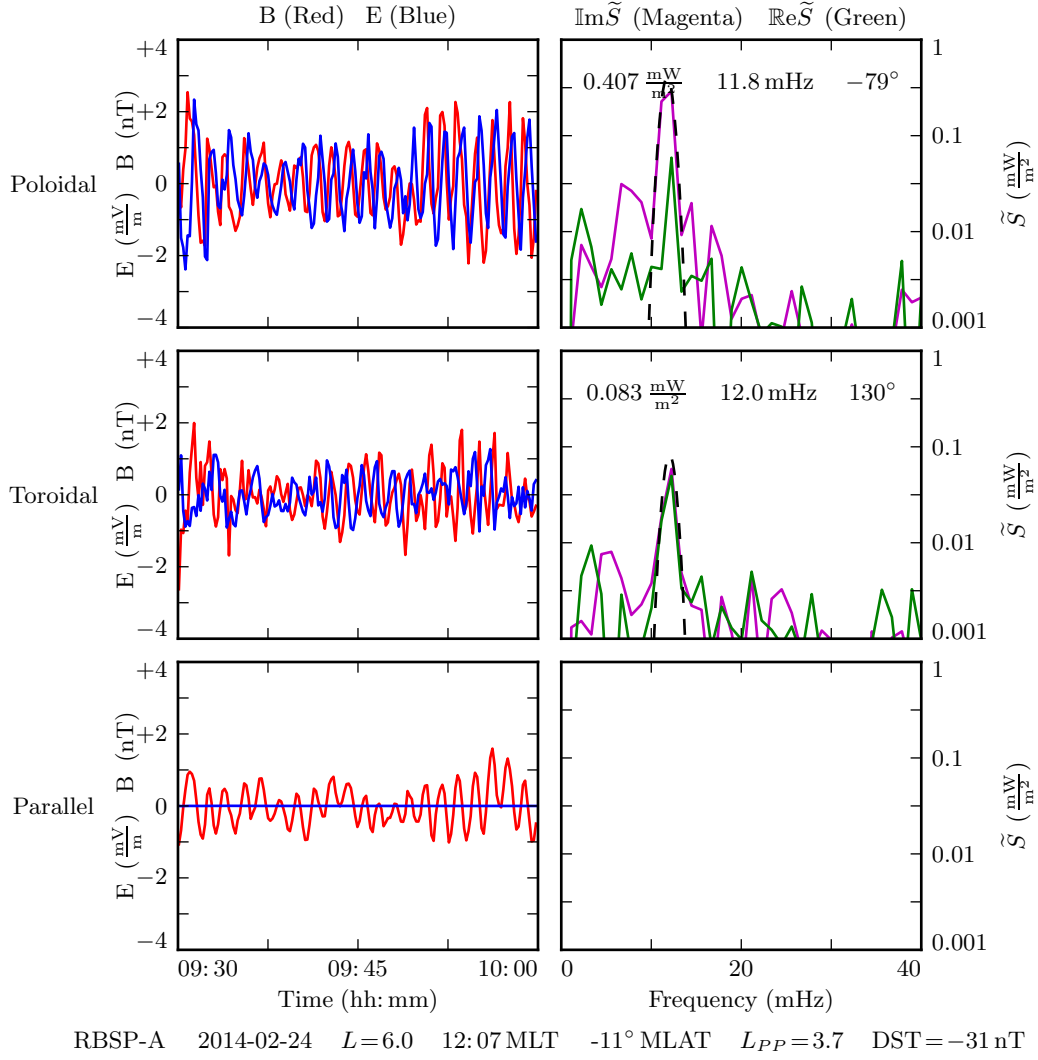


Figure 8.9: The above is a double event, where the poloidal and toroidal channels have been independently selected as events. The poloidal channel shows a wave with most of its energy in the standing wave (phase of 79°). The toroidal mode has a significant traveling component (phase of 130°). The compressional activity implies a low modenumber, which would cause energy to rotate quickly from the poloidal mode to the toroidal mode — evidently at a sufficient rate to replenish the losses due to the traveling mode's real Poynting flux.

Phase Distribution of Pc4 Events by Mode

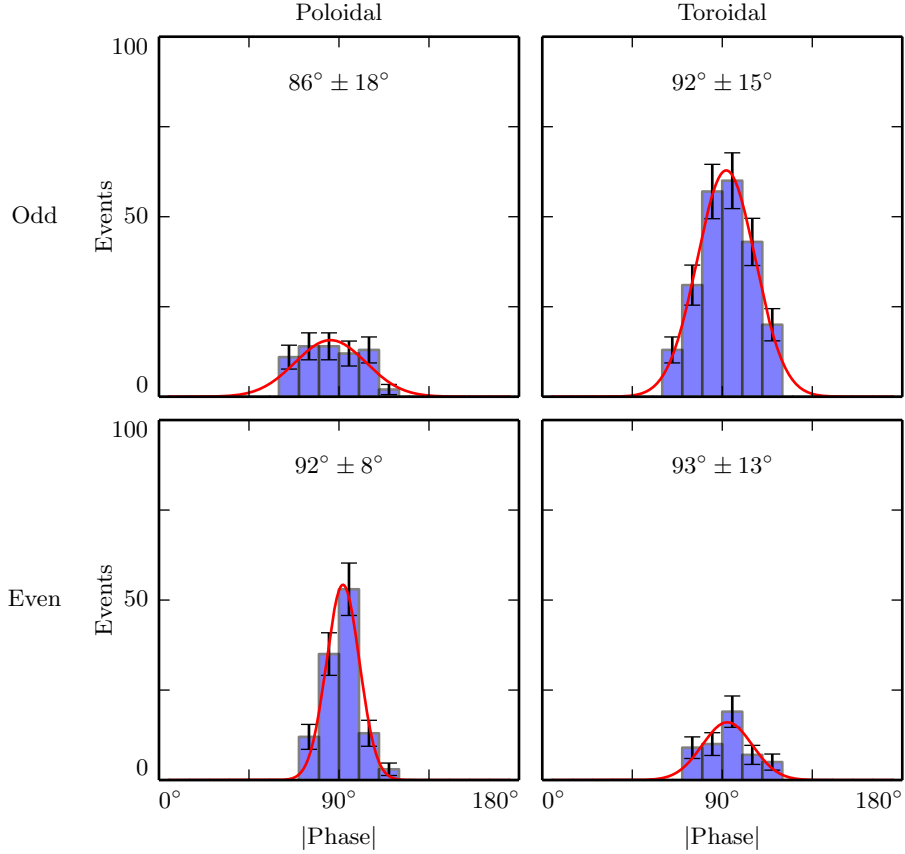


Figure 8.10: The (absolute) phase of the selected Pc4 events is shown above. All modes show phase distributions peaked around 90° . This reflects the fact that a significant traveling wave component quickly carries energy away from an FLR. Odd events are spread more broadly in phase than even events. This is consistent with the odd modes' electric field antinode near the equator, where events are observed; the characteristic loss timescale depends on $\frac{B}{E}$ per Equation (8.3).

Distribution of Pc4 Events by Mode and Phase

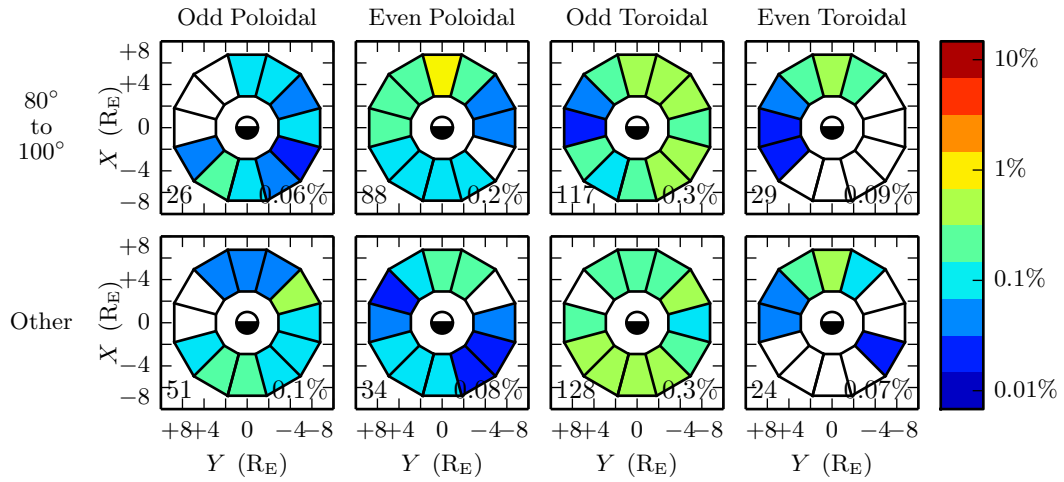


Figure 8.11: The observation rate of events is shown above, divided by (absolute) phase as well as mode. The closer a phase to 90° , the more of an event's energy is in the standing wave, rather than the traveling wave. The spatial distribution of events is more or less consistent between waves with phases very close to 90° and those with a significant traveling wave component.

1521 **8.6 Discussion**

1522 The present chapter gives a survey of \sim 500 thirty-minute Pc4 events, each characterized
1523 in terms of both parity and polarization, and selected in a way that does not introduce
1524 an apparent bias in either property. No past study has so thoroughly disentangled the
1525 parity and polarization of these waves.

1526 Coarsely speaking, event distributions are found to be consistent with past surveys.
1527 Toroidal events dominate overall, and are primarily seen on the morning side. Poloidal
1528 events are spread broadly in MLT, with a peak near noon and distinctive odd harmonics
1529 in the early morning. From there, the simultaneous consideration of harmonic and
1530 polarization, combined with the numerical results from Chapter 7, offers significant
1531 insight.

1532 The near-noon peak of poloidal Pc4 events is shown to be due to even events (a majority
1533 subset). Odd poloidal events occur preferentially near midnight and across the morning
1534 side. Similarly, toroidal events are mostly odd, and it is specifically the odd toroidal
1535 events which occur on the morningside, while even toroidal events peak near noon.

1536 The spatial distribution of even poloidal events looks much like the spatial distribution of
1537 even toroidal events, except that the toroidal distribution is skewed dayward compared
1538 to the poloidal. The same can be said of the odd events. This is consistent (per
1539 Chapter 7) with poloidal events as an effective source for (same-parity) toroidal events
1540 on the dayside, and a less-effective source on the nightside.

1541 As a corollary, the distribution of odd poloidal events is found to closely resemble
1542 the distribution of giant pulsations: midnight and morning. This (consistent with the
1543 numerical results shown in Chapter 7) suggests that the distinctive properties attributed
1544 to giant pulsations are in fact shared by odd poloidal Pc4s overall.

1545 Curiously, only a small minority (18 %) of toroidal events are found to be odd, while a
1546 majority (61 %) of poloidal events are even. This disparity may offer clues to the source
1547 of these waves, or hint at a harmonic dependence in the rate of poloidal-to-toroidal
1548 rotation.

1549 All events are found to follow a similar amplitude distribution, except for even poloidal
1550 events, which are notably larger. The cause is unclear.

1551 Event phase is also considered. Most events of both polarizations are shown to have
1552 absolute phase in the range 80° to 100° , indicating that the traveling component of
1553 $Pc4$ pulsations is small compared to the standing component. Odd events are found to
1554 be spread more broadly in phase; this is likely a consequence of being measured near
1555 the equator, where (due to the electric field antinode) the lifetime of an odd event is
1556 significantly larger than that of an even event with the same phase.

1557 **Chapter 9**

1558 **Conclusion**

1559 Field line resonances in the Pc4 frequency range are known to exhibit a number of
1560 heretofore-unconnected properties. The present work discusses the development of
1561 Tuna, a numerical model created with Pc4s in mind. Using Tuna, Pc4s are mod-
1562 eled across varying frequencies, azimuthal modenumber, and ionospheric conductivity
1563 profiles, suggesting novel connections between Pc4 properties. Numerical results are
1564 complemented by a survey of Pc4 events measured by the Van Allen Probes.

1565 **9.1 Code Development**

1566 Tuna is a two and a half dimensional model — it uses Maxwell’s equations to simulate
1567 the evolution of three-dimensional Alfvén waves on a two-dimensional slice of the mag-
1568 netosphere. Features include a nonorthogonal dipole geometry, a choice between several
1569 height-resolved ionospheric conductivity tensors, and a novel driving mechanism: ring
1570 current perturbation. Tuna has the capacity to simulate parallel currents and electric
1571 fields through the consideration of electron inertial effects, though those effects are dis-
1572 abled by default for the sake of stability. Tuna’s source code and support scripts are
1573 publicly available at <https://github.com/UMN-Space-Physics>.

1574 Future development on Tuna could further parallelize the code using MPI; doing so could
1575 allow the electron inertial length to be properly resolved (which would in turn stabilize

1576 the electron inertial effects). Other potential improvements include dynamic ionospheric
1577 profiles, which become more conductive as energy is deposited in the ionosphere, defor-
1578 mation of the ideal dipole grid, and north-south asymmetry in the ionospheric profile
1579 to account for Earth’s tilt.

1580 9.2 Numerical Work

1581 Tuna suggests several novel results.

1582 Poloidal FLRs are shown to rotate to the toroidal mode on timescales comparable to the
1583 oscillation period, suggesting poloidal waves as a significant source for toroidal waves.
1584 On the nightside, the dissipation timescale is comparable to the oscillation period as
1585 well, so much poloidal energy is lost before rotating to the toroidal mode.

1586 Numerical results also suggest that the distinctive ground signatures attributed to giant
1587 pulsations may be features of odd poloidal Pc4s overall. Generic odd poloidal waves are
1588 shown to exhibit peak ground signatures at $m = 16$ to 32, which are sharply peaked at
1589 auroral latitudes, and which occur preferentially during times of quiet solar activity.

1590 At low m , poloidal waves move readily across L -shells, allowing energy to easily escape
1591 the simulation — such waves can hardly even be called field line resonances. At high
1592 m , the poloidal mode becomes guided, though it is never defined as sharply in L as
1593 the toroidal mode. This is consistent with observations showing toroidal frequencies to
1594 depend strongly on L compared to poloidal frequencies.

1595 The present work exclusively used an odd, sinusoidal, poloidal driver; however, Tuna has
1596 the capacity to deliver more interesting driving waveforms as well, and higher harmonics
1597 could be added with trivial modifications to the code. Test particles could be added,
1598 which would be particularly interesting in runs including electron inertial effects (and
1599 thus parallel electric fields). Tuna could also be used to consider “in situ” measurements
1600 of wave phase.

1601 **9.3 Van Allen Probe Pc4 Survey**

1602 Using data from the Van Allen Probes EMFISIS and EMF instruments, the present work
1603 shows \sim 500 half-hour Pc4 events, each classified by both polarization and harmonic.
1604 Scripts used to download, process, and plot the data are available at <https://github.com/UMN-Space-Physics>.

1606 Odd poloidal events are shown to be concentrated from midnight through the morning
1607 — as with the numerical results, it seems that giant pulsations are unusual compared
1608 to Pc4s overall, but not compared to odd poloidal Pc4s specifically.

1609 Odd toroidal events exhibit a similar distribution to odd poloidal events, but are skewed
1610 dayward across the morningside. The same is true for even events: even poloidal events
1611 peak at noon and are spread across the evening side, while even toroidal events peak at
1612 noon and are far less spread. These distributions are consistent with the poloidal mode
1613 as a significant source for same-harmonic toroidal events, particularly on the dayside,
1614 as suggested by the numerical results.

1615 Overall, poloidal and toroidal events exhibit disparate distributions because poloidal
1616 events are primarily even, while toroidal events are mostly odd; the cause is not appar-
1617 ent.

1618 The body of Pc4 events available in Van Allen Probe data is growing over time. After the
1619 probes complete their second precession, event statistics on the dayside should improve
1620 considerably, allowing more meaningful consideration of subsets of the events, such as
1621 those that take place during geomagnetically active times. Furthermore, the present
1622 work considered the two Van Allen Probes to be independent observers, but future
1623 work could look into the few Pc4 events which are observed simultaneously (or in quick
1624 succession) by both probes. This could offer significant insight into the spatial structure
1625 and temporal evolution of Pc4s — particularly when complemented by numerical work!

1626 References

- 1627 [1] H. Alfvén. On the cosmogony of the solar system III. *Stockholms Observatoriums*
1628 *Annaler*, 14:9.1–9.29, 1946.
- 1629 [2] B. J. Anderson, M. J. Engebretson, S. P. Rounds, L. J. Zanetti, and T. A. Potemra.
1630 A statistical study of Pc 3-5 pulsations observed by the AMPTE/CCE magnetic
1631 fields experiment, 1. occurrence distributions. *J. Geophys. Res.*, 95(A7):10495,
1632 1990.
- 1633 [3] V. Angelopoulos. The THEMIS mission. *Space Science Reviews*, 141(1-4):5–34,
1634 2008.
- 1635 [4] C. W. Arthur and R. L. McPherron. The statistical character of Pc 4 magnetic
1636 pulsations at synchronous orbit. *J. Geophys. Res.*, 86(A3):1325, 1981.
- 1637 [5] K. Birkeland. Expédition norvégienne de 1899-1900 pour l'étude des aurores
1638 boréales. *Mat. Naturvidensk. Kl.*, KI(I), 1901.
- 1639 [6] J. P. Boris. A physically motivated solution of the Alfvén problem. *NRL Memo-*
1640 *randum Report*, 2167, 1970.
- 1641 [7] A. Brekke, T. Feder, and S. Berger. Pc4 giant pulsations recorded in Tromsø,
1642 1929-1985. *Journal of Atmospheric and Terrestrial Physics*, 49(10):1027–1032,
1643 1987.
- 1644 [8] C. W. Carlson, R. F. Pfaff, and J. G. Watzin. The fast auroral Snapshot (FAST)
1645 mission. *Geophys. Res. Lett.*, 25(12):2013–2016, 1998.

- 1646 [9] A. A. Chan, M. Xia, and L. Chen. Anisotropic alfvén-balloonning modes in Earth's
1647 magnetosphere. *J. Geophys. Res. Space Physics*, 99(A9):17351–17366, 1994.
- 1648 [10] L. Chen and A. Hasegawa. A theory of long-period magnetic pulsations: 1. steady
1649 state excitation of field line resonance. *J. Geophys. Res.*, 79(7):1024–1032, 1974.
- 1650 [11] L. Chen and A. Hasegawa. Kinetic theory of geomagnetic pulsations: 1. internal
1651 excitations by energetic particles. *J. Geophys. Res.*, 96(A2):1503, 1991.
- 1652 [12] C. Z. Cheng and Q. Qian. Theory of ballooning-mirror instabilities for anisotropic
1653 pressure plasmas in the magnetosphere. *J. Geophys. Res.*, 99(A6):11193, 1994.
- 1654 [13] G. Chisham and D. Orr. Statistical studies of giant pulsations (pgs): Harmonic
1655 mode. *Planetary and Space Science*, 39(7):999–1006, 1991.
- 1656 [14] W. D. Cummings, R. J. O'Sullivan, and P. J. Coleman. Standing Alfvén waves in
1657 the magnetosphere. *J. Geophys. Res.*, 74(3):778–793, 1969.
- 1658 [15] L. Dai. Collisionless magnetic reconnection via Alfvén eigenmodes. *Phys. Rev.*
1659 *Lett.*, 102(24), 2009.
- 1660 [16] L. Dai, K. Takahashi, R. Lysak, C. Wang, J. R. Wygant, C. Kletzing, J. Bonnell,
1661 C. A. Cattell, C. W. Smith, R. J. MacDowall, S. Thaller, A. Breneman, X. Tang,
1662 X. Tao, and L. Chen. Storm time occurrence and spatial distribution of Pc4
1663 poloidal ULF waves in the inner magnetosphere: A Van Allen Probes statistical
1664 study. *J. Geophys. Res. Space Physics*, 120:4748–4762, 2015.
- 1665 [17] L. Dai, K. Takahashi, J. R. Wygant, L. Chen, J. Bonnell, C. A. Cattell, S. Thaller,
1666 C. Kletzing, C. W. Smith, R. J. MacDowall, D. N. Baker, J. B. Blake, J. Fennell,
1667 S. Claudepierre, H. O. Funsten, G. D. Reeves, and H. E. Spence. Excitation of
1668 poloidal standing Alfvén waves through drift resonance wave-particle interaction.
1669 *Geophys. Res. Lett.*, 40:4127–4132, 2013.
- 1670 [18] A. W. Degeling, R. Rankin, and Q.-G. Zong. Modeling radiation belt electron
1671 acceleration by ULF fast mode waves, launched by solar wind dynamic pressure
1672 fluctuations. *J. Geophys. Res. Space Physics*, 119(11):8916–8928, 2014.

- 1673 [19] W. D. D'haeseleer, W. N. G. H. J. D. Callen, and J. L. Shohet. *Flux Coordinates*
1674 *and Magnetic Field Structure*. Springer-Verlag, New York, 1991.
- 1675 [20] J. W. Dungey. The attenuation of Alfvén waves. *J. Geophys. Res.*, 59(3):323–328,
1676 1954.
- 1677 [21] J. W. Dungey. Interplanetary magnetic field and the auroral zones. *Phys. Rev.*
1678 *Lett.*, 6(2):47–48, 1961.
- 1679 [22] A. Einstein. Die grundlage der allgemeinen relativitätstheorie. *Ann. Phys.*,
1680 354:769–822, 1916.
- 1681 [23] S. R. Elkington, M. K. Hudson, and A. A. Chan. Acceleration of relativistic
1682 electrons via drift-resonant interaction with toroidal-mode Pc-5 ULF oscillations.
1683 *Geophys. Res. Lett.*, 26(21):3273–3276, 1999.
- 1684 [24] M. J. Engebretson, D. L. Murr, K. N. Erickson, R. J. Strangeway, D. M. Klumpar,
1685 S. A. Fuselier, L. J. Zanetti, and T. A. Potemra. The spatial extent of radial
1686 magnetic pulsation events observed in the dayside near synchronous orbit. *J.*
1687 *Geophys. Res.*, 97(A9):13741, 1992.
- 1688 [25] M. J. Engebretson, L. J. Zanetti, T. A. Potemra, and M. H. Acuna. Harmonically
1689 structured ulf pulsations observed by the ampte cce magnetic field experiment.
1690 *Geophysical Research Letters*, 13(9):905–908, 1986.
- 1691 [26] M. J. Engebretson, L. J. Zanetti, T. A. Potemra, D. M. Klumpar, R. J. Strange-
1692 way, and M. H. Acuña. Observations of intense ULF pulsation activity near the
1693 geomagnetic equator during quiet times. *J. Geophys. Res.*, 93(A11):12795, 1988.
- 1694 [27] S. Fujita and T. Tamao. Duct propagation of hydromagnetic waves in the upper
1695 ionosphere, 1, electromagnetic field disturbances in high latitudes associated with
1696 localized incidence of a shear Alfvén wave. *J. Geophys. Res.*, 93(A12):14665, 1988.
- 1697 [28] K.-H. Glassmeier. Magnetometer array observations of a giant pulsation event. *J.*
1698 *Geophys.*, 48:127–138, 1980.
- 1699 [29] K.-H. Glassmeier. On the influence of ionospheres with non-uniform conductivity
1700 distribution on hydromagnetic waves. *J. Geophys.*, 54(2):125–137, 1984.

- 1701 [30] K.-H. Glassmeier, S. Buchert, U. Motschmann, A. Korth, and A. Pedersen. Con-
1702 cerning the generation of geomagnetic giant pulsations by drift-bounce resonance
1703 ring current instabilities. *Ann. Geophysicae*, 17:338–350, 1999.
- 1704 [31] C. Goertz. Kinetic alfvén waves on auroral field lines. *Planetary and Space Science*,
1705 32(11):1387–1392, 1984.
- 1706 [32] C. K. Goertz and R. W. Boswell. Magnetosphere-ionosphere coupling. *J. Geophys.*
1707 *Res.*, 84(A12):7239, 1979.
- 1708 [33] J. Goldstein. Plasmasphere response: Tutorial and review of recent imaging re-
1709 sults. *Space Science Reviews*, 124(1-4):203–216, 2006.
- 1710 [34] C. A. Green. Giant pulsations in the plasmasphere. *Planetary and Space Science*,
1711 33(10):1155–1168, 1985.
- 1712 [35] J. L. Green and S. Boardsen. Duration and extent of the great auroral storm of
1713 1859. *Advances in Space Research*, 38(2):130–135, 2006.
- 1714 [36] C. Greifinger and P. S. Greifinger. Theory of hydromagnetic propagation in the
1715 ionospheric waveguide. *J. Geophys. Res.*, 73(23):7473–7490, 1968.
- 1716 [37] B. C. Hall. *Lie Groups, Lie Algebras, and Representations*. Graduate Texts in
1717 Mathematics. Springer, New York, second edition, 2015.
- 1718 [38] Y. X. Hao, Q.-G. Zong, Y. F. Wang, X.-Z. Zhou, H. Zhang, S. Y. Fu, Z. Y.
1719 Pu, H. E. Spence, J. B. Blake, J. Bonnell, J. R. Wygant, and C. A. Kletzing.
1720 Interactions of energetic electrons with ULF waves triggered by interplanetary
1721 shock: Van allen probes observations in the magnetotail. *J. Geophys. Res. Space*
1722 *Physics*, 119(10):8262–8273, 2014.
- 1723 [39] L. Harang. *Pulsations in the terrestrial magnetic records at high latitude stations*.
1724 Grondahl, 1942.
- 1725 [40] O. Hillebrand, J. Muench, and R. L. McPherron. Ground-satellite correlative
1726 study of a giant pulsation event. *Journal of Geophysics Zeitschrift Geophysik*,
1727 51:129–140, 1982.

- 1728 [41] W. J. Hughes. Magnetospheric ULF waves: A tutorial with a historical perspec-
 1729 tive. In M. J. Engebretson, K. Takahashi, and M. Scholer, editors, *Solar Wind*
 1730 *Sources of Magnetospheric Ultra-Low-Frequency Waves*, volume 81 of *Geophys.*
 1731 *Monogr.*, pages 1–12. American Geophysical Union, Washington, DC, 1994.
- 1732 [42] W. J. Hughes and D. J. Southwood. The screening of micropulsation signals by
 1733 the atmosphere and ionosphere. *J. Geophys. Res.*, 81(19):3234–3240, 1976.
- 1734 [43] W. J. Hughes, D. J. Southwood, B. Mauk, R. L. McPherron, and J. N. Barfield.
 1735 Alfvén waves generated by an inverted plasma energy distribution. *Nature*,
 1736 275(5675):43–45, 1978.
- 1737 [44] J. A. Jacobs, Y. Kato, S. Matsushita, and V. A. Troitskaya. Classification of
 1738 geomagnetic micropulsations. *J. Geophys. Res.*, 69(1):180–181, 1964.
- 1739 [45] T. Karlsson and G. T. Marklund. A statistical study of intense low-altitude electric
 1740 fields observed by freja. *Geophys. Res. Lett.*, 23(9):1005–1008, 1996.
- 1741 [46] Y. Kato and T. Tsutomu. Hydromagnetic oscillations in a conducting medium
 1742 with hall couduct-ivity under the uniform magnetic field. *Science reports of the*
 1743 *Tohoku University. Ser. 5, Geophysics*, 7(3):147–164, 1956.
- 1744 [47] M. C. Kelley. *The Earth’s Ionosphere*. Academic Press, San Diego, second edition,
 1745 1989.
- 1746 [48] R. L. Kessel. Solar wind excitation of pc5 fluctuations in the magnetosphere and
 1747 on the ground. *J. Geophys. Res.*, 113(A4), 2008.
- 1748 [49] D. Y. Klimushkin, P. N. Mager, and K.-H. Glassmeier. Toroidal and poloidal
 1749 Alfvén waves with arbitrary azimuthal wavenumbers in a finite pressure plasma
 1750 in the earth’s magnetosphere. *Annales Geophysicae*, 22(1):267–287, 2004.
- 1751 [50] S. Knight. Parallel electric fields. *Planetary and Space Science*, 21:741–750, 1973.
- 1752 [51] S. Kokubun. Observations of Pc pulsations in the magnetosphere: Satellite-ground
 1753 correlation. *J. Geomagn. Geoelec*, 32(Supplement2):SII17–SII39, 1980.

- 1754 [52] S. Kokubun, K. N. Erickson, T. A. Fritz, and R. L. McPherron. Local time asymmetry of Pc 4-5 pulsations and associated particle modulations at synchronous orbit. *J. Geophys. Res.*, 94(A6):6607–6625, 1989.
- 1755
- 1756
- 1757 [53] D.-H. Lee and K. Kim. Compressional MHD waves in the magnetosphere: A new approach. *J. Geophys. Res.*, 104(A6):12379–12385, 1999.
- 1758
- 1759 [54] A. S. Leonovich and V. A. Mazur. Structure of magnetosonic eigenoscillations of an axisymmetric magnetosphere. *J. Geophys. Res.*, 105(A12):27707–27715, 2000.
- 1760
- 1761 [55] W. Liu, J. B. Cao, X. Li, T. E. Sarris, Q.-G. Zong, M. Hartinger, K. Takahashi, H. Zhang, Q. Q. Shi, and V. Angelopoulos. Poloidal ULF wave observed in the plasmasphere boundary layer. *J. Geophys. Res. Space Physics*, 118(7):4298–4307, 2013.
- 1762
- 1763
- 1764
- 1765 [56] W. Liu, T. E. Sarris, X. Li, S. R. Elkington, R. Ergun, V. Angelopoulos, J. Bonnell, and K. H. Glassmeier. Electric and magnetic field observations of Pc4 and Pc5 pulsations in the inner magnetosphere: A statistical study. *J. Geophys. Res.*, 114(A12), 2009.
- 1766
- 1767
- 1768
- 1769 [57] W. Liu, T. E. Sarris, X. Li, Q.-G. Zong, R. Ergun, V. Angelopoulos, and K. H. Glassmeier. Spatial structure and temporal evolution of a dayside poloidal ULF wave event. *Geophys. Res. Lett.*, 38(19), 2011.
- 1770
- 1771
- 1772 [58] R. L. Lysak. Magnetosphere-ionosphere coupling by Alfvén waves at midlatitudes. *J. Geophys. Res.*, 109, 2004.
- 1773
- 1774 [59] R. L. Lysak and D. hun Lee. Response of the dipole magnetosphere to pressure pulses. *Geophys. Res. Lett.*, 19(9):937–940, 1992.
- 1775
- 1776 [60] R. L. Lysak and Y. Song. A three-dimensional model of the propagation of Alfvén waves through the auroral ionosphere: first results. *Adv. Space Res.*, 28:813–822, 2001.
- 1777
- 1778
- 1779 [61] R. L. Lysak and Y. Song. Development of parallel electric fields at the plasma sheet boundary layer. *J. Geophys. Res. Space Physics*, 116, 2011.
- 1780

- 1781 [62] R. L. Lysak, C. L. Waters, and M. D. Sciffer. Modeling of the ionospheric Alfvén
1782 resonator in dipolar geometry. *J. Geophys. Res. Space Physics*, 118, 2013.
- 1783 [63] P. N. Mager and D. Y. Klimushkin. Giant pulsations as modes of a transverse
1784 Alfvénic resonator on the plasmapause. *Earth, Planets and Space*, 65(5):397–409,
1785 2013.
- 1786 [64] I. R. Mann, E. A. Lee, S. G. Claudepierre, J. F. Fennell, A. Degeling, I. J. Rae,
1787 D. N. Baker, G. D. Reeves, H. E. Spence, L. G. Ozeke, R. Rankin, D. K. Milling,
1788 A. Kale, R. H. W. Friedel, and F. Honary. Discovery of the action of a geophysical
1789 synchrotron in the Earth’s Van Allen radiation belts. *Nature Communications*, 4,
1790 2013.
- 1791 [65] I. R. Mann and A. N. Wright. Finite lifetimes of ideal poloidal Alfvén waves. *J.
1792 Geophys. Res.*, 100:23677–23686, 1995.
- 1793 [66] I. R. Mann, A. N. Wright, and A. W. Hood. Multiple-timescales analysis of ideal
1794 poloidal Alfvén waves. *J. Geophys. Res.*, 102(A2):2381–2390, 1997.
- 1795 [67] T. Maynard, N. Smith, S. Gonzalez, et al. Solar storm risk to the North American
1796 electric grid. 2013.
- 1797 [68] R. L. McPherron. The role of substorms in the generation of magnetic storms.
1798 *Washington DC American Geophysical Union Geophysical Monograph Series*,
1799 98:131–147, 1997.
- 1800 [69] T. Motoba, K. Takahashi, J. V. Rodriguez, and C. T. Russell. Giant pulsations on
1801 the afternoonside: Geostationary satellite and ground observations. *J. Geophys.
1802 Res. Space Physics*, 120:8350–8367, 2015.
- 1803 [70] NASA. Coordinated data analysis (workshop) web.
- 1804 [71] NASA. Near miss: The solar superstorm of july 2012.
- 1805 [72] M. Nicolet. The collision frequency of electrons in the ionosphere. *Journal of
1806 Atmospheric and Terrestrial Physics*, 3(4):200–211, 1953.
- 1807 [73] L. G. Ozeke and I. R. Mann. Energization of radiation belt electrons by ring
1808 current ion driven ULF waves. *J. Geophys. Res.*, 113(A2), 2008.

- 1809 [74] E. M. Poulter, W. Allan, E. Nielsen, and K.-H. Glassmeier. Stare radar observa-
1810 tions of a PG pulsation. *J. Geophys. Res.*, 88(A7):5668, 1983.
- 1811 [75] H. R. Radoski. A note on oscillating field lines. *J. Geophys. Res.*, 72(1), 1967.
- 1812 [76] H. R. Radoski. A theory of latitude dependent geomagnetic micropulsations: The
1813 asymptotic fields. *J. Geophys. Res.*, 79, 1974.
- 1814 [77] R. Rankin, J. C. Samson, and V. T. Tikhonchuk. Parallel electric fields in dis-
1815 persive shear alfvén waves in the dipolar magnetosphere. *Geophys. Res. Lett.*,
1816 26(24):3601–3604, 1999.
- 1817 [78] B. Rolf. Giant micropulsations at abisko. *J. Geophys. Res.*, 36(1):9, 1931.
- 1818 [79] G. Rostoker, H.-L. Lam, and J. V. Olson. PC 4 giant pulsations in the morning
1819 sector. *J. Geophys. Res.*, 84(A9):5153, 1979.
- 1820 [80] J. C. Samson, L. L. Cogger, and Q. Pao. Observations of field line resonances,
1821 auroral arcs, and auroral vortex structures. *J. Geophys. Res.*, 101(A8):17373–
1822 17383, 1996.
- 1823 [81] H. J. Singer, W. J. Hughes, and C. T. Russell. Standing hydromagnetic waves
1824 observed by ISEE 1 and 2: Radial extent and harmonic. *J. Geophys. Res.*,
1825 87(A5):3519, 1982.
- 1826 [82] D. J. Southwood. Some features of field line resonances in the magnetosphere.
1827 *Planetary and Space Science*, 22(3):483–491, 1974.
- 1828 [83] D. J. Southwood. A general approach to low-frequency instability in the ring
1829 current plasma. *J. Geophys. Res.*, 81(19):3340–3348, 1976.
- 1830 [84] J. Stratton and N. J. Fox. Radiation belt storm probes (RBSP) mission overview.
1831 In *2012 IEEE Aerospace Conference*. Institute of Electrical & Electronics Engi-
1832 neers (IEEE), 2012.
- 1833 [85] E. Sucksdorff. Giant pulsations recorded at sodankyl during 19141938. *Terrestrial
1834 Magnetism and Atmospheric Electricity*, 44(2):157–170, 1939.

- 1835 [86] K. Takahashi, J. Bonnell, K.-H. Glassmeier, V. Angelopoulos, H. J. Singer, P. J.
1836 Chi, R. E. Denton, Y. Nishimura, D.-H. Lee, M. Nosé, and W. Liu. Multipoint
1837 observation of fast mode waves trapped in the dayside plasmasphere. *J. Geophys.*
1838 *Res.*, 115(A12), 2010.
- 1839 [87] K. Takahashi, K.-H. Glassmeier, V. Angelopoulos, J. Bonnell, Y. Nishimura, H. J.
1840 Singer, and C. T. Russell. Multisatellite observations of a giant pulsation event.
1841 *J. Geophys. Res.*, 116:A11223, 2011.
- 1842 [88] K. Takahashi, M. D. Hartinger, V. Angelopoulos, K.-H. Glassmeier, and H. J.
1843 Singer. Multispacecraft observations of fundamental poloidal waves without
1844 ground magnetic signatures. *J. Geophys. Res. Space Physics*, 118:4319–4334, 2013.
- 1845 [89] K. Takahashi, R. W. McEntire, A. T. Y. Lui, and T. A. Potemra. Ion flux oscillations
1846 associated with a radially polarized transverse Pc 5 magnetic pulsation. *J.*
1847 *Geophys. Res.*, 95(A4):3717, 1990.
- 1848 [90] K. Takahashi and R. L. McPherron. Standing hydromagnetic oscillations in the
1849 magnetosphere. *Planetary and Space Science*, 32:1343–1359, 1984.
- 1850 [91] K. Takahashi, N. Sato, J. Warnecke, H. Lühr, H. E. Spence, and Y. Tonegawa.
1851 On the standing wave mode of giant pulsations. *J. Geophys. Res. Space Physics*,
1852 97(A7):10717–10732, 1992.
- 1853 [92] B. J. Thompson and R. L. Lysak. Electron acceleration by inertial alfvén waves.
1854 *J. Geophys. Res.*, 101(A3):5359–5369, 1996.
- 1855 [93] V. T. Tikhonchuk and R. Rankin. Electron kinetic effects in standing shear alfvén
1856 waves in the dipolar magnetosphere. *Physics of Plasmas*, 7(6):2630, 2000.
- 1857 [94] B. T. Tsurutani, W. D. Gonzalez, G. S. Lakhina, and S. Alex. The extreme
1858 magnetic storm of 12 september 1859. *Journal of Geophysical Research: Space*
1859 *Physics*, 108(A7), 2003. 1268.
- 1860 [95] A. Y. Ukhorskiy. Impact of toroidal ULF waves on the outer radiation belt elec-
1861 trons. *J. Geophys. Res.*, 110(A10), 2005.

- 1862 [96] J. A. Wanliss and K. M. Showalter. High-resolution global storm index: Dst versus
1863 sym-h. *Journal of Geophysical Research: Space Physics*, 111(A2):n/a–n/a, 2006.
1864 A02202.
- 1865 [97] C. L. Waters, R. L. Lysak, and M. D. Sciffer. On the coupling of fast and shear
1866 Alfvén wave modes by the ionospheric Hall conductance. *Earth Planets Space*,
1867 65:385–396, 2013.
- 1868 [98] C. L. Waters and M. D. Sciffer. Field line resonant frequencies and ionospheric
1869 conductance: Results from a 2-d MHD model. *J. Geophys. Res.*, 113(A5), 2008.
- 1870 [99] D. M. Wright and T. K. Yeoman. High-latitude HF doppler observations of ULF
1871 waves: 2. waves with small spatial scale sizes. *Ann. Geophys.*, 17(7):868–876,
1872 1999.
- 1873 [100] J. R. Wygant, J. W. Bonnell, K. Goetz, R. E. Ergun, F. S. Mozer, S. D. Bale,
1874 M. Ludlam, P. Turin, P. R. Harvey, R. Hochmann, K. Harps, G. Dalton, J. Mc-
1875 Cauley, W. Rachelson, D. Gordon, B. Donakowski, C. Shultz, C. Smith, M. Diaz-
1876 Aguado, J. Fischer, S. Heavner, P. Berg, D. M. Malsapina, M. K. Bolton, M. Hud-
1877 son, R. J. Strangeway, D. N. Baker, X. Li, J. Albert, J. C. Foster, C. C. Chaston,
1878 I. Mann, E. Donovan, C. M. Cully, C. A. Cattell, V. Krasnoselskikh, K. Kersten,
1879 A. Brenneman, and J. B. Tao. The electric field and waves instruments on the
1880 radiation belt storm probes mission. *Space Science Reviews*, 179(1):183–220, 2013.
- 1881 [101] J. R. Wygant, A. Keiling, C. A. Cattell, R. L. Lysak, M. Temerin, F. S. Mozer,
1882 C. A. Kletzing, J. D. Scudder, V. Streltsov, W. Lotko, and C. T. Russell. Evidence
1883 for kinetic alfvn waves and parallel electron energization at 46 re altitudes in the
1884 plasma sheet boundary layer. *Journal of Geophysical Research: Space Physics*,
1885 107(A8):SMP 24–1–SMP 24–15, 2002.
- 1886 [102] K. Yee. Numerical solution of initial boundary value problems involving maxwell's
1887 equations in isotropic media. *IEEE Trans. Antennas Propagat.*, 14(3), 1966.
- 1888 [103] T. K. Yeoman and D. M. Wright. ULF waves with drift resonance and drift-bounce
1889 resonance energy sources as observed in artificially-induced HF radar backscatter.
1890 *Ann. Geophys.*, 19(2):159–170, 2001.

- 1891 [104] Q.-G. Zong, X.-Z. Zhou, X. Li, P. Song, S. Y. Fu, D. N. Baker, Z. Y. Pu, T. A.
1892 Fritz, P. Daly, A. Balogh, and H. Réme. Ultralow frequency modulation of ener-
1893 getic particles in the dayside magnetosphere. *Geophys. Res. Lett.*, 34(12), 2007.
- 1894 [105] Q.-G. Zong, X.-Z. Zhou, Y. F. Wang, X. Li, P. Song, D. N. Baker, T. A. Fritz,
1895 P. W. Daly, M. Dunlop, and A. Pedersen. Energetic electron response to ULF
1896 waves induced by interplanetary shocks in the outer radiation belt. *J. Geophys.
1897 Res.*, 114(A10), 2009.